Doctoral Thesis

Soft Sensor-based Servo Press Monitoring

Author:
Jon Olaizola

Supervisors:
Dr. Eneko Sáenz de Argandoña
Dr. Aitzol Iturrospe

A thesis submitted in fulfillment of
the requirements for the degree of
Doctor of Philosophy in the

Mondragon Unibertsitatea
Department of Electronics and Computer Science

January 21, 2020

Abstract

The force that a servo press exerts forming a workpiece is one the most important magnitudes in any metal forming operation. The process force, along with the characteristics of the die, is what shapes the workpiece. When the process force is greater than the maximum force for which the servo press was designed, the servo press integrity can be damaged. Therefore, the knowledge of the process force is of great interest for both, press manufacturers and users. As such, the metal forming sector is seeking systems that can monitor the process force and the operation of the servo press to analyse process's performance and predict future deviations in the forming operation. Servo press users want to guarantee the quality of the formed parts and reduce facility downtimes due to malfunctions of the press.

This dissertation addressed the monitoring of the process force and the dynamic performance of a servo press based on a model based statistical signal processing algorithm known as the dual particle filter (dPF). Initially both, the developed model of a servo press and the proposed dPF, have been experimentally evaluated and validated in a reduced scale test bench. The test bench has been designed and manufactured based on a design methodology that allows to replicate the kinematic and dynamic behaviour of different servo press facilities in the same test bench. The experimental validation has been also carried out in an industrial servo press under three different metal forming processes. The estimation results have proved the ability of the dPF to track the process force throughout the evaluated processes, obtaining a deviation lower than 5% with respect to the measured force signals at the maximum force position. The dPF algorithm has been accelerated by means of a field programmable gate array (FPGA) to achieve a real time estimation.

Laburpena

Serbo prentsa batek pieza gordin bat eraldatzeko egindako prozesuko indarra edozein konformatu eragiketako magnitude garrantzitsuenetarikoa da. Prozesuko indarra da, trokelaren ezaugarriekin batera, pieza gordina eraldatzen duena. Prozesuko indarra prentsak diseinuaren arabera jasan dezakeena baino handiagoa bada, prentsak kalteak izan ditzake bere osotasunean. Beraz, prozesuko indarraren ezagutza interes handikoa da, prentsa egileentzat zein erabiltzaileentzat. Hori dela eta, metal eraldatzearen sektoreak prozesuko indarra eta prentsa beraren funtzionamendua monitoriza ditzaketen sistemen bila diardute, prentsaren jarduera aztertu eta eraldatzeko operazioetan etorkizunean izan daitezkeen desbideraketak aurreikusteko. Prentsa erabiltzaileek fabrikatutako piezen kalitatea bermatzea eta funtzionamendu akatsengatiko prentsaren geldialdiak murriztea bilatzen dute.

Tesi honek servo prentsa baten prozesuko indarra eta portarea dinamikoaren monitorizazioa jorratzen ditu, *dual particle filter* (dPF) izeneko modeloetan oinarritutako seinalaren prozesamendu estadistikoko algoritmo baten bitartez. Lehenik eta behin, garatutako servo prentsaren modeloa eta proposatutako dPFa eskalatutako entsegutarako banku batean ebaluatu eta balioztatu dira. Eskalatutako entsegutarako bankua serbo prentsa desberdinen portaera zinematiko eta dinamikoa erreplikatzea ahalbidetzen duen metodologia baten bitartez diseinatu eta gauzatu da. Esperimentu bidezko balioztatzea serbo prentsa industrial batean ere gauzatu da hiru konformatuko prozesu desberdinetan. Estimazio emaitzek dPFak prozesuko indarrari jarraitzeko duen ahalmena forgatu dute, neurtutako indarrarekiko %5ekoa baino txikiagoko desbideraketa lortuz indar maximoa egiten den puntuan. dPF algoritmoa *field programmable gate array* (FPGA) baten bitartez azeleratu da, denbora errealeko estimazioa lortzeko.

Resumen

La fuerza que una servo prensa ejerce conformando una pieza es la magnitud más importante en cualquier operación de conformado. La fuerza aplicada, junto a las características del troquel, es la magnitud que da forma a la pieza. Cuando la fuerza de proceso es más grande que la fuerza máxima para la que fue diseñada la servo prensa, la integridad de ésta puede verse afectada. Por lo tanto, el conocimiento de la fuerza de proceso es de grán interés tanto para los fabricantes de prensas como para los usuarios de las mismas. Así pues, el sector del conformado está buscando sistemas capaces de monitorizar la fuerza de proceso y el funcionamiento de la servo prensa para analizar el proceso y predecir futuras desviaciones de las operaciónes de conformado. Los usuarios de las servo prensas quieren garantizar la calidad de las piezas fabricadas y reducir las paradas de las servo prensas debidas al mal funcionamiento de las mismas.

Esta tesis aborda la monitorización de la fuerza de proceso y el comportamiento dinámico de una servo prensa mediante un algoritmo de tratamiento estadístico de la señal conocido como el *dual Particle Filter* (dPF). Inicialmente, tanto el modelo desarrollado como el dPF propuesto han sido evaluados y validados experimentalmente en un banco de ensayos de escala reducida. El banco de ensayos ha sido diseñado y fabricado mediante una metodología de diseño que permite replicar el comportamiento cinemático y dinámico de distintas servo prensas en el mismo banco. La validación experimental también se ha llevado a cabo en una servo prensa industrial mediante tres procesos de conformado distintos. Los resultados de estimación han provado la habilidad del dPF para seguir la fuerza de proceso en los procesos evaluados, obteniendo una desviación menor que un 5% con respecto a las señales medidas en el punto donde se da la fuerza máxima. El algoritmo dPF ha sido acelerado mediante un *filed programmable gate array* (FPGA) para lograr estimaciones en tiempo real.

Acknowledgements

Tesi honetako ikerketa lana burutzea ezinezkoa izango litzateke hainbat eta hainbat pertsonen laguntzarik gabe. Eskerrak ematerako orduan nire bi tesi zuzendarietatik hasi nahiko nuke, Eneko Sáenz de Argandoña eta Aitzol Iturrospe, momentu oro eskeini eta eman didaten laguntzarengatik. Nire zuzendariez gain, era guztietako lanekin eta arazoekin lagundu didaten beste pertsona askorekin ere gogoratzen naiz, Jose Manuel Abete, Jokin Lozares, Lander Galdos, Gorka Plata, Javier Trinidad, Aitor Osa, Arkaitz Garate... eta beste hainbat eta hainbatekin.

I also have to thank Christos-Savvas Bouganis for hosting me at Imperial College London and for all the support and help he provided me during the stay. His guidance contributed to the research and development of the hardware implementation part of the algorithm.

I would like to thank the members of the evaluation committee, as well as the reviewers that showed their willingness to assess this dissertation.

Tesiaren alde zientifiko-teknikoa albo batera lagata, tesian zehar izandako buruhauste eta momentu onetan aldamenean izan ditudanekin ere gogoratzen naiz, etxekoekin, familia, lagun eta batez ere Josunerekin.

Contents

List of Figures

List of Tables

List of Acronyms

AC alternate current

BDC bottom dead centre

BRAM block random access memory

CG centre of gravity

CPU central processing unit

DDSS data driven soft sensor

DoF degrees of freedom

dPF dual Particle filter

dq0 direct-quadrature-zero

DSP digital signal processing

EKF extended Kalman filter

EUIO extended unknown input observer

FF flip flop

FOC field oriented control

FPGA field programmable gate array

GPU graphics processing unit

HLS high-level synthesis

ICT information and communication technology

II initiation interval

KF Kalman filter

LO Luenberger observer

LUT lookup table

MBSS model based soft sensor

MC Monte Carlo

MCMC Markov chain Monte Carlo

PE piezoelectric

PEM prediction error method

PF particle filter

PF-S states particle filter

PF-UI unknown input particle filter

PL programmable logic

PMSM permanent magnets synchronous machine/motor

PS processing system

RMSE root mean square error

RNG random number generator

SNR signal to noise ratio

TDC top dead centre

UART universal asynchronous receiver-transmitter

UIO unknown input observer

UKF unscented Kalman filter

List of Symbols

A area of the load balancer

B viscous friction coefficient

F_{lb} force of the load balancer

F_{ms} force of the process

I_1 inertia of the crankshaft

I_2 inertia of the two connecting rods

I_4 inertia of the 1$^{\text{st}}$ gear of the gearbox

I_5 inertia of the 2$^{\text{nd}}$ gear of the gearbox

I_6 inertia of the 3$^{\text{rd}}$ gear of the gearbox

I_7 inertia of the servomotor's rotor

J inertia of the servomotor's rotor

K_t PMSM's constant or motor constant

L inductance of a stator winding

L Lagrange function

N_d number of unknown input particles

N_x number of state particles

Q number of fundamental dimensions

Q_k generalised coordinates

R equivalent resistance of each stator winding

T kinetic energy

U number of estimands

V potential energy

W weight of a particle

Ω sensitivity of a parameter

Φ_k^i dynamic equilibrium deviation for each unknown input particle

$\acute{l}$ distance between the end of the crank and CG2

$\acute{r}$ distance between the rotation centre of the crank and CG1

$\bar{}$ prediction

β angle of the connecting rod with respect to the upper side of the ram

$\boldsymbol{\sigma^2}$ variance vector associated to the measurement noise

$\boldsymbol{d}$ unknown inputs vector

$\boldsymbol{p}$ parameters vector

$\boldsymbol{q}$ variance vector associated to the process noise

$\boldsymbol{u}$ known inputs vector

$\boldsymbol{x}$ state vector

$\boldsymbol{y}$ output vector

$\ddot{\theta}$ angular acceleration of the crankshaft

$\dot{\theta}$ angular speed of the crankshaft

η reduction ratio of the gearbox

η_4 reduction ratio of the 1$^{\text{st}}$ gear of the gearbox

η_5 reduction ratio of the 2$^{\text{nd}}$ gear of the gearbox

η_6 reduction ratio of the 3$^{\text{rd}}$ gear of the gearbox

$\hat{}$ estimation

ϕ_a ϕ_b ϕ_c total magnetic fluxes of each phase of stator windings

ϕ_{am} ϕ_{bm} ϕ_{cm} magnetic fluxes of permanent magnets

τ_e electric torque of a PMSM

τ_{fric} friction torque

θ angle of the crankshaft

θ_e electrical angle of a PMSM

θ_r angle of PMSM's rotor

$\tilde{}$ proposal

ξ elastic coefficient of the servo press structure

a linear acceleration

f_c Coulomb's friction coefficient

f_s sampling frequency

f_s static friction coefficient

f_v viscous friction coefficient

g gravitational acceleration constant

i_a i_b i_c **or** I_{abc} three current phases of stator windings

j repeating estimand

l length of the connecting rod

l_i initial latency

l_t total latency

m_1 mass of the crankshaft (only the excentricity i.e. cranks)

m_2 mass of the two connecting rods

m_3 mass of the ram

p number of pole pairs of PMSM'S rotor

p_i initial pressure of the load balancer

p_m slope of pressure variation in the load balancer

q_k state variables in generalised coordinates

r radius of the crank

s linear displacement of the ram

s estimand

t_e execution time of an instruction

t_s sampling time

t_t total execution time

v_a v_b v_c three voltage phases of stator windings

v_s Stribeck's sliding friction coefficient

x linear deformation of the servo press structure

y position of the ram

Chapter 1

Introduction

1.1 Metal forming machinery sector outline

The global competition that exists in the industrial sector forces companies to improve their products and processes to survive and prosper. Metal forming industry, located in the manufacturing sector, is not excluded from the above assertion. In 2016, metal forming related industries represented 5.33% of the European manufacturing sector's gross income, totaling an amount of €102.05 billion[1]. Companies in the metal forming industry employed 6.07% of the workers attached to the manufacturing sector, i.e. almost 1.85 million persons. The industrial activities that participate in the metal forming sector are listed in Table 1.1, along with some data which emphasizes their impact in the European economy.

	Persons employed (number)	**Value added at factor cost[2] (billion €)**	**Enterprises (number)**	**Production value[3] (billion €)**
Manufacturing	30,472,486	1,912	2,120,592	6,763
Forging, pressing, stamping and roll-forming of metal; powder metallurgy	303,000	18.08	14.623	56.71

[1] A billion is used to denote one thousand million.

[2] Value added at factor costs is the gross income from operating activities after adjusting for operating subsidies and indirect taxes. Value adjustments (such as depreciation) are not subtracted (Eurostat, 2016).

[3] Production value is defined as turnover, plus or minus the changes in stocks of finished products, work in progress and goods and services purchased for resale, minus the purchases of goods and services for resale, plus capitalised production, plus other operating income (excluding subsidies) (Eurostat, 2016).

Manufacture of metal forming machinery	148,476	10.38	4.200	28.57
Manufacture of bodies (coachwork) for motor vehicles; manufacture of trailers and semi-trailers	161,540	8.47	7.041	32.27
Manufacture of parts and accessories for motor vehicles	1,236,688	65.10	10.400	256.31
Total	1,849,704	102.05	36,264	373.87
Percentage from Manufacturing	6.07	5.34	1.71	5.53

Table 1.1: Economic and employment data of metal forming related industrial manufacturing activities (Eurostat, 2016).

To be more competitive in the global market, the European metal forming sector wishes to decrease costs associated to machinery maintenance tasks, while keeping quality of products. Widodo and Yang, 2007 and Keith, 2002 stated that the costs related to the maintenance of produced iron and steel goods can reach up to 60% of the total production costs in the manufacturing sector.

To reduce the costs related to the maintenance activities, companies have been looking for solutions to anticipate machine failures by adopting monitoring systems that provide information to carry out machine diagnostics, starting from a reactive maintenance towards a predictive one (Keith, 2002). In this regard, the so-called German initiative "Industry 4.0", coined in 2011, seeks the automation of current manufacturing processes and plants among other actions, adopting intelligent monitoring strategies to carry out a predictive maintenance. Industry 4.0 involves the implementation of information and communication technologies (ICTs) to monitor and control manufacturing processes. According to Davies, 2015, the adoption of such technologies may increase productivity 20%, preventing machine failures and cutting downtime up to 50%.

A successful predictive maintenance lies in a precise diagnostic and prognostic of a process carried out by a machine as stated by J. Zhou et al., 2005. This means that deviations from the machine's nominal condition must be detected before they derive in failures that can imply machine downtimes. To detect this kind of undesired deviations, such as wear of machine's components or operation over specified machine limits, intelligent monitoring strategies are developed as mentioned by Lee et al., 2015.

Knowing the benefits associated to predictive maintenance, the manufacturing sector is adopting

new solutions based on sensor integration in machines, model based soft sensors and data driven soft sensors as pointed out by Esteban et al., 2016; R. Patton et al., 2000; Chen and R. J. Patton, 2012. These solutions are based on the condition monitoring of production machines and processes, allowing to foresee undesirable deviations of machine's condition and schedule preventive maintenance actions before machine failures become more severe and derive in unexpected machine downtimes.

1.2 Metal forming processes and facilities

Metal forming is a manufacturing process of shaping metal workpieces through plastic deformation, without adding or subtracting material. Many processes are inside this category, such as rolling, extrusion, cold and hot forging, bending and deep drawing. Additionally, other processes like joining and parting can be performed through this technology as described in Schuler, 1998. Metal forming is a complex manufacturing process where multiple factors may affect the performance of the press, such as the workpiece's properties and the wear of machine components, (Doege et al., 2002).

Most metal forming processes are carried out by presses. Among presses, mechanical presses are the most common presses used in batch/mass production of sheet metal parts, as claimed by Altan and Tekkaya, 2012a. Mechanical presses have some common components as defined by Altan and Tekkaya, 2012b, which are described below:

- A frame that supports the bolster, where the bed of the press is attached.
- A driving mechanism that controls the slider or ram movement (slider and ram are used indistinctly throughout the document).
- A guiding system that guides the ram in its linear displacement. The guiding system also keeps ram's parallelism with respect to the bed.
- A drive shaft that transmits the torque of the driving mechanism to the ram, composed by a gearbox, a crankshaft and the connecting rods.
- A load balancer that counteracts ram's weight.

These components are shown in Figure 1.1.

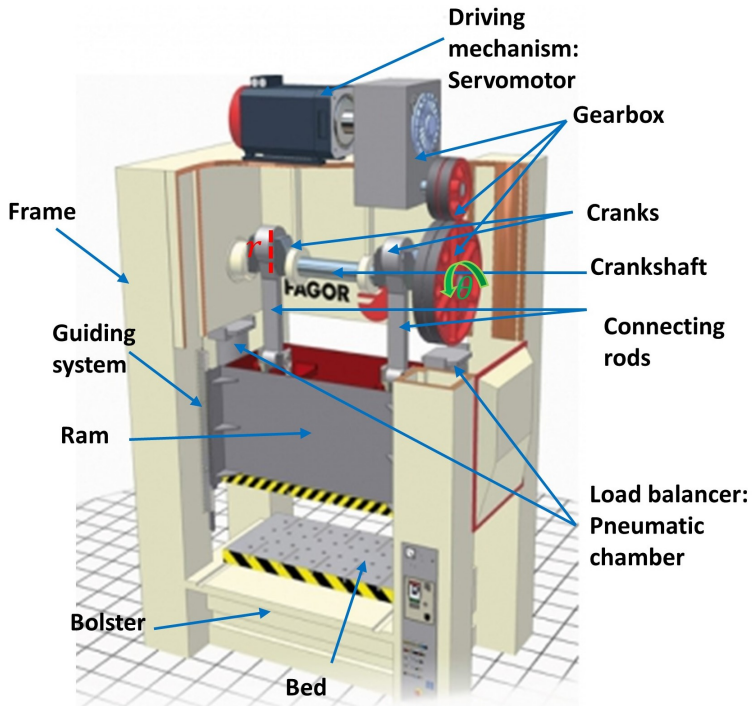

Figure 1.1: Common components of metal forming press (Courtesy of Fagor Arrasate).

According to Altan and Tekkaya, 2012b, crank driven presses are the simplest and most widely used mechanical presses in the metal forming industry. The slider crank system converts the rotary motion of a driving mechanism into linear motion of the ram. The ram of these presses perform a fixed displacement of $2r$ per stroke, being r the radius of the crank. The relation between the angular position of the crankshaft and the linear displacement of the ram is described by a sinusoidal curve as shown in figure 1.2. The highest position of the displacement of the ram is called the top dead centre (TDC), whereas the lowest position is called the bottom dead centre (BDC).

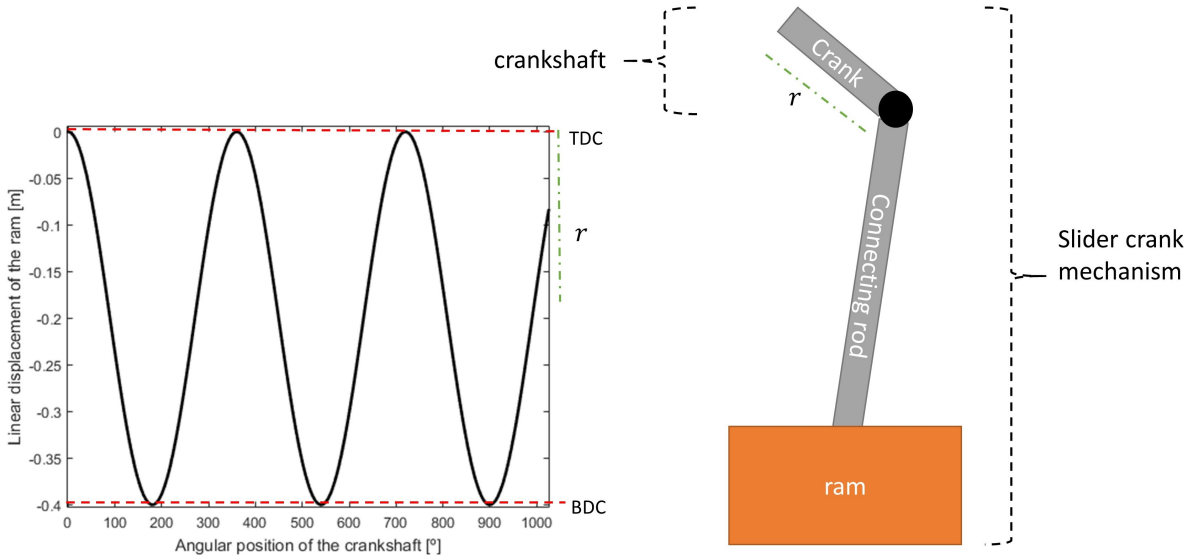

Figure 1.2: Ram displacement and a ram crank mechanism.

Slider crank mechanical presses can be classified in two types depending on the driving mechanism: conventional mechanical presses and servo presses. Table 1.2 describes the differences regarding the components of both presses.

System	Conventional Press	Servo Press
Working	Crankshaft, connecting rod shaft	Crankshaft, connecting rod shaft
Transmission	Belt drive	Transmission Gear
Driving	Clutch brake unit	Operating regulator, servomotor
Energy	Motor and flywheel	AC servomotor
Support	Press frame	Press frame

Table 1.2: Components of the two types of mechanical slider crank presses described by Yu et al., 2013.

Servo presses have many advantages with respect to conventional presses. The main advantage of servo presses is that their driving mechanism can be controlled at a variable speed in the same working cycle, while conventional presses can only move the driving mechanism at a constant speed, as stated by Osakada et al., 2011. Another advantage is that a servomotor can produce multiple position and speed profiles to drive the crankshaft of the press. Moreover, the position and speed control of the servomotor can synchronise the servo press operation with other machines of the production line. Besides, the signals and commands (such as position, speed or current, among others) used by the control of servo presses may shed light on the applied force, which can be used to monitor the metal forming process and the machine's condition.

1.3 Monitoring of metal forming processes and facilities

In any metal forming operation the process force is one of the key indicators that provides most relevant information not only about the quality of the process, but also about the condition of the press as claimed by Sharma, 1999. The finishing of a workpiece is highly related with the magnitude of the force during the process. The condition of the press components can also be assessed by means of the process force, as claimed by Spitler et al., 2003 and Altan and Tekkaya, 2012a. The process force can be used to detect and measure undesirable events that may arise during the forming operation, such as overload forces or reverse loads, which can damage the integrity of the press components. As described by Ghiotti, Regazzo, et al., 2010 and Ghiotti, Bruschi, et al., 2014 a reverse load is produced when cutting high strength metal sheets, and is released as a negative or reverse force when the metal sheet is fractured. Overload forces arise when the process force exceeds the maximum press load capacity (Council, 2004). The real time monitoring of the servo press's signals may lead to preventive actions, such as emergency stops of the driving system, to protect the components and the structure of the press. In the case of servo presses, these force signal could be used by the control system.

Either in servo presses or conventional presses, force measurements are commonly carried out

by load cells or piezoelectric (PE) sensors as described in Shieh et al., 2001; Doege et al., 2002; Altan and Tekkaya, 2012a. Both type of sensors require a calibration step to relate the applied force with the deformation of the component where force sensors are installed. Furthermore, these sensor suffer drift or a calibration loss throughout the life cycle of the press, as stated by Doege et al., 2002; Kumme et al., 2002; Wilson, 2005. The location of sensors must also be considered since it affects the quality of the measurement and their re-usability:

- The press frame is a common location for force sensors due to its easy accessibility and the low wear the sensors suffer during their life cycle, as mentioned by Altan and Tekkaya, 2012a. Load cells and PE sensors measure forces based on the strain the press frame suffers when process force is exerted. According to Altan and Tekkaya, 2012a other users install PE sensors in the connecting rods, mounting them either on the surface of the connecting rod or in drilled holes. PE sensors installed on connecting rods yield more precise readings than the ones carried out by frame located sensors, as they are closer to the process.
- In-die mounting of force sensors provides more sensitivity compared with the frame or connecting rod mounting solution, since sensors are placed closer to the forming process. Nonetheless, when the die is replaced to manufacture another part, these sensors have to be fitted to the new die or even changed for new sensors as mentioned in Altan and Tekkaya, 2012a.

Although physical sensors can initially provide precise readings and they are relatively straightforward to install, their integration involves purchasing and installing costs. Besides, physical sensor integration may be invasive and can affect the integrity of press components, since sensors are placed within components, as the drilled holes of the connecting rods, or in working areas of the press, as in the in-die installation solution. Furthermore, hardware sensors are prone to lose their initial calibration throughout the life cycle of the press, providing incorrect measurements.

Owing to the information that can be extracted from the process force and the limitations of the physical sensors discussed above, section 1.4 presents several techniques that can be used to monitor the process force taking advantage of the already available signals provided by the control systems of servo presses.

1.4 State of the art

This section describes the technologies and methods reviewed throughout the dissertation to estimate the press force. The literature review is focused in monitoring technologies that do not require the installation of physical force sensors, able to obtain the process force in any forming operation in real-time.

The following subsections are organized in three blocks. Subsections 1.4.1 and 1.4.2 present various monitoring technologies that have been employed in industrial applications to estimate

the forces of different machines and processes. Subsection 1.4.3 analyses the hardware architectures and devices that have been utilised to accelerate the reviewed technologies to achieve a real time monitoring. Subsection 1.4.4 reviews different methodologies to design a test bench able to emulate the dynamic and kinematic behaviour of servo presses. This way, experiments can be done in a controlled lab environment.

1.4.1 Indirect measurements: soft sensing approach

During the last decades, researchers on monitoring systems have advanced towards indirect measurement algorithms (also known as soft sensors) to replace the conventional physical sensor based measurements. According to Doraiswami and Cheded, 2014, generally speaking, "a soft sensor is a software based sensor used in industrial applications to replace hardware sensors, which are costly, difficult to maintain and even impossible to physically access". Soft sensors are software algorithms that process different physical sensors' signals at the same time to produce estimations. Soft sensors take advantage of the interactions of the measured signals to estimate new magnitudes that are not measured.

In this line, Senda et al., 2014 patented a force control methodology for a servo press. To the best of my knowledge this monitoring technology is the only publication that I found, that is close to what is intended to achieve in this thesis, but it has some important limitations. In this patent, authors protected a procedure to indirectly measure the process force of a servo press of a powder compacting operation, taking advantage of the electric motor's torque signal. They calculated the process force using the kinematic relationship between the torque and the force of the servo press. The kinematic relationship is given by the geometric features of the slider crank mechanism. The calculation of the process force is carried out while the servo press is stopped at different positions of the displacement of the ram while it is compacting powder. They do not include the kinetics (dynamic behaviour) of the servo press in their patent and therefore, this method is not able to obtain the process force at a continuous press operation.

Over the years, two classes of soft sensors have been proposed. As mentioned by Esteban et al., 2016, the so-called model based soft sensors (MBSSs) are based on the previous knowledge about the process/system to be monitored. Besides, data driven soft sensors (DDSSs) rely on a empirical model elaborated from the measured data. These soft sensors are trained on the data collected during the operation of the process, as described by Webster and Eren, 2014.

Model based soft sensors

MBSSs lean on the so-called white-box or grey-box models, which are respectively models that include full or partial information about the dynamics of the process or system. The description of white-box models is fully specified by physical knowledge and is deterministic. Grey-box models are described by prior knowledge and can also accommodate stochastic phenomena

within the model as claimed by Kristensen et al., 2004. Radke and Gao, 2006 pointed out that the quality of the estimated information increases as the model of the system or process improves.

A model is a mathematical representation of the system or process, described usually by ordinary differential equations, as mentioned by Kadlec et al., 2009. Models are described by state variables (also known as states), parameters, inputs and their interrelations. The states represent the behaviour of the system (e.g. the speed of a mass) for any time and the parameters describe system's condition or characteristics (e.g. the value of the mass). Systems can be driven by some external inputs (e.g. the force applied to move the mass). Those inputs can either be known or unknown. Finally, when a state is observable (measurable by a sensor), it is known as a system output.

MBSSs have been extensively used to estimate the states, parameters and unknown inputs of the model taking advantage of available system inputs and outputs. Estimations are carried out correcting the difference between the measured output(s) and the outputs generated by the MBSS fitting the estimation. Figure 1.3 depicts the basic scheme of a MBSS. (From now on, those internal behaviours or dynamics will be called as states of the system while components conditions will be named as parameters of the system, as proposed by Ogata, 2010).

As depicted in figure 1.3, the MBSS estimates the state variables (commonly represented by an $\boldsymbol{x}$), parameters (represented by a $\boldsymbol{p}$) and/or unknown inputs (commonly represented by a $\boldsymbol{d}$) based on the measured input signals $\boldsymbol{u}$ and output signals $\boldsymbol{y}$, fitting the estimations to minimise the error between the actual $\boldsymbol{y}$ and predicted $\bar{\boldsymbol{y}}$ outputs. From this section onward, these three estimable model components that represent physical magnitudes will be called as estimands (parameters, states and inputs), as suggested by Gelman et al., 2013.

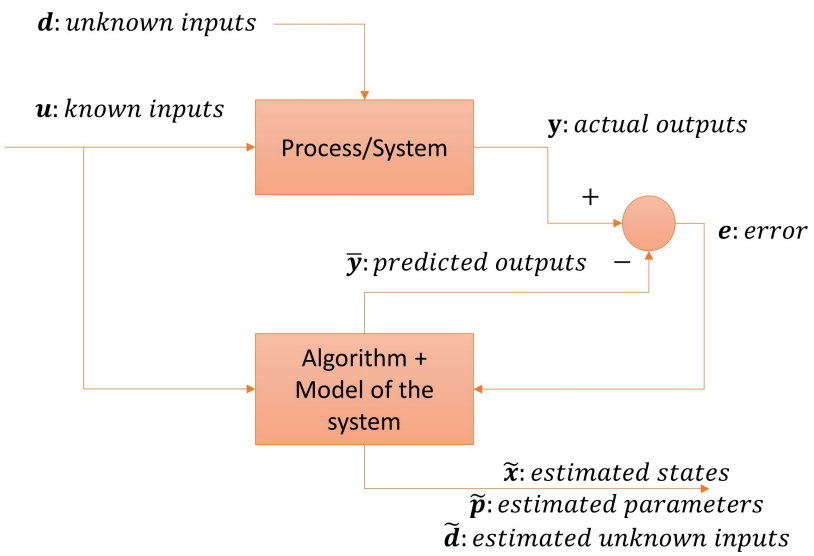

Figure 1.3: Basic scheme of a MBSS.

Data driven soft sensors

As pointed out by Kadlec et al., 2009, DDSSs rely on black-box models. Black-box models are empirical models that describe functional relationships between system inputs and outputs. The parameters of these models do not represent any physical magnitude such as mass, heat or any other kind of physical coefficients (Zhang, 2010). According to Yan et al., 2016, DDSSs require an initial training step to setup the black-box model. This training step is carried out by means of statistical or soft computing supervised learning approaches that take advantage of the training data measured throughout several experiments. Essentially, the training step adjusts the parameters of the black-box model until the output coincides with the measured output of the real system. Once the model is configured, the DDSSs can be used to estimate system states and parameters.

As stated by Webster and Eren, 2014; Yan et al., 2016, one of the main handicaps of the DDSSs is the lack of significant enough data to train the algorithm. The lack of significant data can affect the precision of the model built by the training step and in turn the precision of estimations. Besides, the models built by the training step are rarely physically interpretable, which makes difficult to understand the underlying physical phenomena of the system or process. Figure 1.4 shows a block diagram of a DDSS, which, first, builds a model by means of the training step and, then, takes advantage of the model to estimate system or process states and parameters.

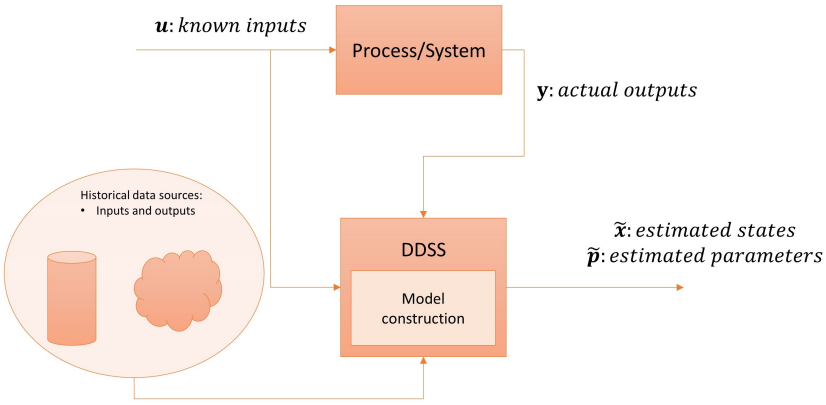

Figure 1.4: Basic scheme of a DDSS.

Comparison between MBSS and DDSS

In the scientific literature, there are many reviews and surveys such as (Radke and Gao, 2006; Fortuna et al., 2007; Kadlec et al., 2009), that compare MBSS and DDSS approaches. Within those reviews, authors discuss the benefits and drawbacks of both approaches and mention the suitable applications for each approach.

If the process or system under review is well understood and a mathematical model that represents the condition and dynamics of the system can be formulated, MBSSs can be adopted. In this way, MBSSs allow a better insight of the underlying physical phenomena, which can be

evaluated to check the plausibility of the estimation results. On the contrary, the requirement of an extensive knowledge about the process or system can be also a handicap, as discussed in Kadlec et al., 2009, since the precision of estimations can worsen in the absence of a model that represents the dynamic of the system or process accurately.

Many processes and systems, due to their nature, are difficult to model because of the complexity of their dynamic behaviour and interactions between system components. In those cases the DDSS approach can be adopted as reviewed in Kadlec et al., 2009; Webster and Eren, 2014. However, the application of such soft sensors has also its difficulties. According to Lahiri, 2017, the amount of historical data has to be large and significant enough to obtain a model that is able to represent the dynamic behaviour of the process or system. Besides, the estimated models are sometimes difficult to interpret, due to the lack of a mathematical model that explains the system or process with a physical sense as pointed out by Rizzo, 2010.

Regarding the servo press system that was analysed in this dissertation, the MBSS approach is the most suitable strategy to monitor the dynamic behaviour of the system and the processes it performs. Regarding the mathematical modelling of the servo press, there are many publications in the literature that have already studied the dynamic system's that form the servo press. Besides, the estimations carried out by means of MBSSs are more intuitive thanks to the developed model.

1.4.2 Model based soft sensing

A MBSS approach needs three elements to perform its estimations: system measurements, a model of the system and a soft sensor algorithm. If sufficient, measurements are obtained taking advantage of the already available signals acquired from sensors or control devices already operating in the machine to be monitored.

The other two elements, the model and the soft sensor, will be addressed in two subsections. Subsection "MBSS: Servo press modelling" reviews some methods and publications that addressed the modelling of the two subsystems of the servo press and subsection "MBSS: soft sensors" presents a set of MBSSs, analysing their characteristics and their applicability depending on the estimands to be monitored, the way these soft sensors process the data and the assumptions the different types of MBSSs make regarding the estimands.

MBSS: Servo press modelling

A mechanical servo press merges an electrical subsystem and a mechanical subsystem. The electrical subsystem is composed of a servomotor and its control system. The mechanical subsystem is composed of the mechanical components of the press, as illustrated in figure 1.5.

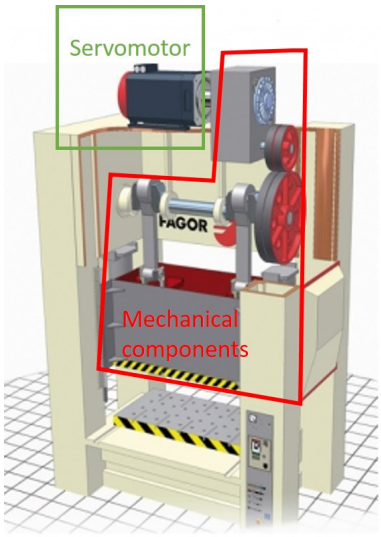

Figure 1.5: Electric and mechanical subsystems of a servo press.

- **Electrical subsystem**

  Manufacturers usually install alternate current (AC) permanent magnets synchronous motors (PMSMs) to drive the mechanical subsystem of the press, since they provide high torque capacities along with high position and speed control accuracy and flexibility (Halicioglu et al., 2016a). As stated by Gieras, 2002 a PMSM is an electromechanical device whose rotor rotates synchronised with the magnetic field generated by a (usually) three-phase electrical winding system. In the literature there are lots of publications that address the derivation of the mathematical model of a PMSM type servomotor as presented, for instance, by Arroyo, 2006; Benjak and Gerling, 2010; Kung et al., 2015. The models proposed by these authors derive an expression for the electrical torque exerted by the PMSM, taking into account the three phase currents, the magnetic flux of the rotor's permanent magnets and the resistances and inductances of the stator's windings. In addition, Esteban et al., 2016 proposed a joint model of an electromechanical system that gathers an electrical and a mechanical subsystem as in the case of the servo press. The presented joint model is formed by an electrical subsystem that includes a PMSM and a control device and by a mechanical subsystem that represents an elevator.

  Merzoug, Naceri, et al., 2008 pointed out the field oriented control (FOC) as one of the most common control schemes utilised to drive PMSM servomotors. The FOC usually includes several control loops that produce control commands based on a signature to drive the system, based on the measured feedback signals, as shown in figure 1.6. Those feedback signals utilised by the control scheme are usually the angular position, the angular speed and the three-phase current signals. Indeed, these signals are considered robust according to Huh et al., 2007, as the FOC is designed to be insensitive to the variations of the system's components that it controls (Peresada et al., 1999).

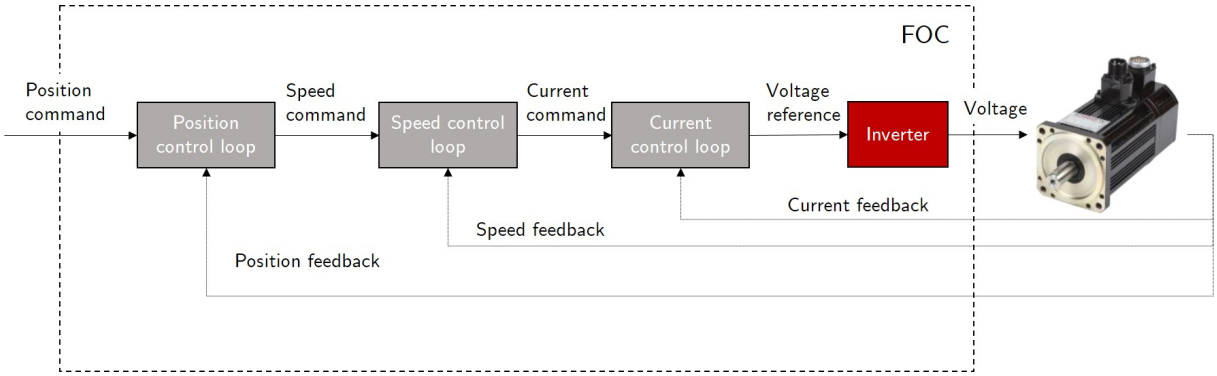

Figure 1.6: Control loops of FOC driving a PMSM.

- **Mechanical subsystem**

  The mechanical subsystem of the servo press is formed of a gearbox, an eccentric crankshaft, one or various connecting rods, a ram and a pneumatic load balancer. In the mechanical literature there are many publications that address the modelling of systems formed by kinematic chains and actuators, such as presses, using different approaches (Ha et al., 2006; Khemili and Romdhane, 2008; Zheng and X. Zhou, 2014). Generally speaking, there are three main approaches to obtain the dynamic model of mechanisms, the so-called Newton-Euler method, the Lagrange method and the kineto-static method as claimed by He et al., 2006.

  The kineto-static method operates with Newton's second law so that it transforms the dynamic problem into a static problem by finding the dynamic equilibrium of forces acting within the system. The dynamic equilibrium is achieved subtracting the force and the product of inertial terms and acceleration: $F - ma = 0$ and it is commonly known as D'Alembert's principle. The forces that actuate over the system are modelled as external inputs. As the kineto-static approach is a method that simplifies the dynamic problem by neglecting speed variations, the modelled dynamic behaviour of the system may be imprecise (He et al., 2006). For instance, He et al., 2006 used the kineto-static method to obtain the dynamic model of a mechanical press driven by a constant speed motor.

  The Newton-Euler approach is more intuitive than the kineto-static approach since elaborates a expression that includes all the forces and torques acting in each rigid body, including constraint forces between the connections of those rigid bodies that limit their motion in some coordinates. In Newton-Euler method the external forces exerted by actuators are also modelled as inputs. This approach is based on the force/torque balance among rigid bodies, where each rigid body requires its own equation. However, Newton-Euler requires a more extensive physical knowledge about the system than in kineto-static and Lagrange approaches, since constraint forces must be known and included in the dynamic equation, apart from other torques and forces that govern the motion of rigid bodies. Khalil, 2011 used the Newton-Euler method to obtain the dynamic model of different types of robots, which include a parametrised friction model.

  The Lagrange method is a systematic approach that obtains an analytical equation of the

system's dynamic behaviour from the energetic model of system's components, based on a single or multiple generalised coordinates. These generalised coordinates represent the degrees of freedom (DoF) of a system. As it formulates the mentioned energy expression, all the workless forces and constraints are not considered, easing the derivation of the dynamic equation. Besides, all the system components are expressed in a single dynamic equation and external forces are modelled as system inputs. Ha et al., 2006 and Halicioglu et al., 2016a; Halicioglu et al., 2016b propose Lagrange function based dynamic modelling of a ram crank mechanism. The obtained model's generalised coordinate was the angle of the crank, and the kinematic and the dynamic behaviour of the rest of the components were given in that coordinate. Ha et al., 2006 included also a parametrised friction force.

Components' geometrical features, such as connecting rod and crankshaft lengths, are represented in the model as they describe the coordinates and kinematics of the connected components in a ram crank system as shown in figure 1.7. This geometric characteristics along with inertia and masses of the rigid bodies that form the kinematic chain of the servo press are system parameters. CG1, CG2 and CG3 represent the centres of gravity of the crank, the connecting rod and the ram respectively. l, r, θ, β, and y are the length of the connecting rod, the radius of the crank, the crank's input angle, the connecting rod's angle and the position of the ram respectively. $\acute{r}$ represents the distance between the rotation centre of the crank and CG1, while $\acute{l}$ represents the distance between the end of the crank and CG2.

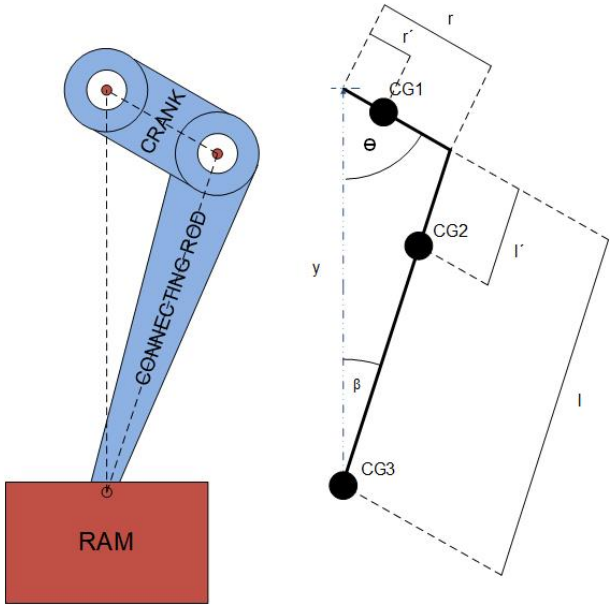

Figure 1.7: Crank-connecting rod-ram mechanism's geometric features.

The kinematic chain models proposed by the analysed modelling approaches include actuators forces as external inputs. Besides, friction forces interacting with the system are also modelled. Therefore, the process force of the servo press should be modelled as an input and friction model's parameters must be also identified.

The next subsection addresses the different types of MBSS algorithms that can be used to

estimate magnitudes such as the process force.

MBSS: soft sensors

MBSSs are algorithms that rely on statistical signal processing techniques to estimate unknown or noisy quantities of a system or process taking advantage of a model and the available measurements. MBSS can process data recursively or in batch (Candy, 2016). Recursive MBSSs process data step by step, as each measurement becomes available. The recursive MBSSs are usually used for real time applications to continuously estimate variable estimands. Conversely, batch MBSSs process multiple time steps' data at one time. Batch MBSSs cannot be used for real time estimations, but are considered more robust since they make their estimations based in the whole measured data set as mentioned by Särkkä, 2013. Batch MBSSs are usually designed for the estimation of invariable estimands like model parameters.

MBSS can be deterministic or probabilistic, depending on if the analysed model is deterministic or stochastic respectively. Deterministic models define system estimands by means of fixed values and the output of the model is entirely determined by a set of parameters, inputs and previous states as claimed by (Renard et al., 2013). Among deterministic observers, The Luenberger observer (LO) (Luenberger, 1966) and the unknown input observer (UIO) (Garcia and Frank, 1997) have been widely used in many industrial applications. The LO was developed to recursively estimate the states of linear systems. The LO is not suitable neither for complex linear systems nor nonlinear systems as claimed by Ali et al., 2015. Regarding the unknown input estimation, Darouach, 1994 proposed the UIO to estimate system unknown inputs recursively. It was first designed to deal with linear systems. The nonlinear version of the UIO requires a linearisation step around an operating point at each time step, which may introduce large estimation errors when monitoring highly nonlinear systems, as claimed by Zarei and Poshtan, 2010. Besides, the design of such MBSSs is complicated for nonlinear models, as stated by Garcia and Frank, 1997. Other extensions of UIO, such as the extended UIO (EUIO) (Hsu et al., 2001; Pan et al., 2016), despite their ability to estimate simultaneously states and unknown inputs, also require the mentioned linearisation step prone to fail in highly nonlinear systems.

In contrast, stochastic models used by probabilistic MBSSs assume systems are exposed to uncertainties, such as noisy measurements due to limited accuracy of sensors or unmodelled processes driving the modelled system. According to Bellman, 1964 and Candy, 2016 stochastic models represent the real systems more faithfully, due to the inherent randomness of real systems. The prediction error method (PEM) is a batch probabilistic MBSS that estimate parameters of the system using system's model, inputs and outputs (Ljung, 2002). It estimates the parameters by an optimization approach, minimizing the error between the predicted output and the actual output (measured from the real system). Although the processing time of PEM is variable and is computationally costly, PEM estimations are more robust than recursive MBSSs' ones, as PEM evaluates the estimands for the whole measured data set.

Within the probabilistic algorithms, the so-known Bayesian MBSS have attracted the interest of many engineers due to their ability to incorporate a priori information about the system or process model and improve estimations (Candy, 2016). Bayesian MBSSs represent the estimands by means of probability distributions, even though the estimand is a parameter with a unique value (e.g. the mass of a solid-rigid body). The adoption of Bayesian MBSS has led from theoretical applications to practical ones for highly nonlinear and non-Gaussian problems. Early Bayesian MBSSs tackled by Kalman et al., 1960; Faragher et al., 2012 were formulated to carry out estimations in dynamic linear and nonlinear models, assuming that estimands' uncertainties follow a Gaussian distribution (e.g. Kalman filter based algorithms). Other authors, such as Arulampalam et al., 2002; Candy, 2016; Kitagawa and Gersch, 2012 proposed the so-called Monte Carlo (MC) methods able to model the uncertainties of estimands by means of either Gaussian or non-Gaussian probability distributions in dynamic linear or nonlinear models.

Within the Bayesian signal processing the Kalman filter proposed by Kalman et al., 1960 (KF) was one of the first popular Bayesian MBSSs used to recursively estimate system states. The KF was only applicable in linear systems and assumes the states uncertainty is Gaussian. Two variants of the KF, the extended KF (EKF) (Ljung, 1979; Huang and Dissanayake, 2007) and the unscented KF (UKF) (Julier and Uhlmann, 1997; Wan and Van Der Merwe, 2000; Chowdhary and Jategaonkar, 2010) overcome some of the limitations of the KF, as they can deal with nonlinear systems and are able to estimate simultaneously states and parameters recursively. Similarly to KF, EKF and UKF model the estimands uncertainties as a Gaussian distribution. EKF linearises the nonlinear model around an operating point at each time step, which may introduce large errors in highly nonlinear systems as claimed by Haseltine and Rawlings, 2005. UKF instead, is computationally expensive since proposes a set of samples of the estimand and evaluates those samples through the model to obtain a mean and a covariance of the estimand (Konatowski et al., 2016).

Another MBSSs family within the Bayesian signal processing is MC methods presented by Hammersley and Handscomb, 1964. MC methods is a collection of MBSSs able to estimate estimands based on random sampling and simulation. Although this collection was presented first in the 60s, it has not been extensively adopted until first high performance computers appeared. These algorithms generate a set of independent random samples of the estimands, propagate them through the model (simulate) and evaluate their likelihood using the measurements. Within this family the most used algorithms are the Markov chain Monte Carlo (MCMC) and the particle filters (PF). MCMC (Hastings, 1970) was formulated to estimate parameters, while PF was developed (Del Moral, 1996) to estimate system states. To the best of the authors knowledge it has never been used to estimate time-varying unknown inputs, although it might have potential to do so.

With respect to the simultaneous estimation of states and unknown inputs a dual version of the PF (dPF) has been recently used by Mejri et al., 2013. Although the work tackles the simultaneous estimation of states and unknown inputs, it is not able to deal with time-varying unknown inputs, since the input is parametrised. The main benefit of the dual PF scheme is

that the particles of each PF are decoupled and evaluated separately, improving the accuracy of the estimations as stated by Mustière et al., 2009.

MC methods can deal either with linear or nonlinear models and they do not require any linearisation procedure. In addition, MC methods can assume Gaussian or non-Gaussian probability distributions for estimands' uncertainties. These two characteristics make them preferable to KF based algorithms when monitoring nonlinear systems. As a drawback, MC family soft sensors provide sometimes slow execution time due to the amount of computations they carry out to evaluate the likelihood as mentioned by Gilks et al., 1995. The computational effort increases as the number of initialised particles raises. To tackle this issue some recent publications, like the ones posed by S. Liu et al., 2014; Mingas, 2015; Sileshi et al., 2016; Mingas, Bottolo, et al., 2017, raise acceleration architectures relying on hardware devices, which allow a faster execution of MC methods.

Table 1.3 gathers the soft sensors discussed in the above lines, classifying them according to the analysed characteristics.

Attribute		**LO**	**UIO**	**EUIO**	**PEM**	**KF**	**EKF**	**UKF**	**MCMC**	**PF**	**dPF**
System type	Linear	✓	✓	✓	✓	✓	✓	✓	✓	✓	✓
	Nonlinear	✗	✓	✓	✓	✗	✓	✓	✓	✓	✓
Processing	Recursive	✓	✓	✓	✗	✓	✓	✓	✗	✓	✓
	Batch	✗	✗	✗	✓	✗	✗	✗	✓	✗	✗
Uncertainty's distribution	Gaussian	-	-	-	✗	✓	✓	✓	✗	✗	✗
	Any	-	-	-	✓	✗	✗	✗	✓	✓	✓
Measurements	$\boldsymbol{y}$	✓	✓	✓	✓	✓	✓	✓	✓	✓	✓
	$\boldsymbol{u}$	✓	✗	✗	✓	✓	✓	✓	✓	?	?
Estimations	$\hat{\boldsymbol{x}}$	✓	✗	✓	✗	✓	✓	✓	✗	✓	✓
	$\hat{\boldsymbol{\theta}}$	✗	✗	✗	✓	✗	✓	✓	✓	✗	✓
	$\hat{\boldsymbol{d}}$	✗	✓	✓	✗	✗	✗	✗	✗	?	?

Table 1.3: Characteristics of the MBSS used in engineering applications.

? means potentially applicable.

- $\boldsymbol{y}$: measured states
- $\boldsymbol{u}$: measured inputs
- $\hat{\boldsymbol{x}}$: estimated states
- $\hat{\boldsymbol{\theta}}$: estimated parameters
- $\hat{\boldsymbol{d}}$: estimated unknown (unmeasured) inputs

1.4.3 Hardware implementation based acceleration

To give response to the slow execution time subjected to MC methods, researches have adopted recently new hardware implementation solutions, employing several architectures and techniques to accelerate the workflow and the execution of these soft sensors. Mingas, 2015 mention a large number of real scenarios where the CPU cannot face the computational effort that MC methods demand.

MC methods such as MCMC, PF and dPF have many independent (non-sequential) instructions that can be parallelised. Thanks to this independence, parallel processing and pipelining can be carried out by using modern hardware devices that employ parallelisation. Pipelining is a technique that allows to increase the throughput by dividing the code into sequential steps that can run overlapped in time (Aiken and Nicolau, 1988).

Multicore central processing units (CPUs), graphics processing units (GPUs) and field programmable gate arrays (FPGAs) are able to carry out operations in parallel. According to Mingas and Bouganis, 2016, multicore CPUs provide limited parallelism per chip and were originally manufactured for sequential code, so they cannot tackle applications that demand a high degree of parallelism. GPUs and CPUs have fixed hardware architectures, while FPGAs are reconfigurable, which facilitates custom modifications.

Regarding data storage specifications of the analysed hardware devices, there are two variants in terms of memory allocation: on-chip or off-chip. As the name indicates, the on-chip memory is placed on the processing chip, while off-chip memory is located outside the processing chip. Mingas, Bottolo, et al., 2017 stated that a GPU has a predefined amount of on-chip memory per processing core, while an FPGA provides more flexibility, as it can allocate a custom amount of on-chip memory to each processing block. When data is stored on-chip, communication between the various hardware blocks of the device is faster than when it is stored off-chip, due to the latency associated with off-chip memory communication. In recent years, hardware manufacturers have moved towards hybrid solutions that combine some of the mentioned hardware to exploit their benefits in a single device. These devices allow sequential code to run on traditional CPUs and the parallelizable code to run in FPGAs to accelerate execution.

To take advantage of the parallelizable characteristics of MC methods, some researches began to implement these algorithms on multicore architectures using FPGAs and application-specific integrated circuits. Some authors, such as Lebedev, Cheng, et al., 2010; Lebedev, Fletcher, et al., 2012; Alves et al., 2015, proposed an architecture containing many cores for the implementation of MC methods. This method enables a parallel programming model implemented on FPGA. Lin et al., 2010 posed a framework for high computation throughput by exploiting FPGA's distributed memories and abundant hardware structures.

1.4.4 Test bench design

To validate the proposed MBSS, firstly, experimental tests will be carried out in a test bench to evaluate the model and the algorithm in a controlled environment. For this purpose, a scaled model of the real servo press will be designed and manufactured keeping the dynamic similarities with the original system.

Scaled systems that keep a dynamic and kinematic similitude with the original system allow to test different machine configurations and experiments, as if they were tested in the original machine (Kittirungsi, 2008). This scaled systems can shed light about the kinematic and the dynamic response of the original machine under different conditions and experiments in a controlled environment. Moreover, scaled systems allow to save time and money since the original machine does not need to be stopped to carry out a set of experiments. For instance, Brennan and Alleyne, 2001 designed and evaluated a scaled test bench of a vehicle and a roadway for a safe and economic testing of a vehicle control application. The scaled vehicle and the roadway kept the dynamic and kinematic similitude with the original vehicle. More recently, Esteban et al., 2016 presented a scaled elevator system that was used to test different electrical and mechanical configurations in controlled lab conditions.

According to Coutinho et al., 2016, there are mainly two methods that authors have used during the last decades to design and manufacture mechanical systems based on similitude theory: the dimensional analysis and the differential equations method. The similitude theory states the necessary and minimum conditions of similarity that a new system or machine must keep with the original system, so that its dynamics and kinematics are representative of the original system.

The dimensional analysis elaborates scaling laws based on the Buckingham's π method proposed by Vaschy, 1892. The Buckingham's π theorem groups system's estimands, which derive in scaling laws. Magnitudes are grouped so their product yields a dimensionless result. These groups are named as π-groups and both, the scaled system and the original one, must yield the same result to guarantee the dynamic and the kinematic similitude. Several authors have applied the dimension analysis to scale systems and machines as Simitses and Rezaeepazhand, 1992; Szirtes, 2007; Esteban et al., 2017.

Kline, 2012 and Baker et al., 1973 proposed the application of the similitude theory using differential equations. In this method the similitude theory is applied to the governing analytical differential equations. Interrelations of scaling laws are formulated arbitrarily based on the knowledge of the designer about the physical properties of system to be scaled. For instance, the designer may define that the mass and the length of the scaled system have to be scaled based on the same ratio (e.g. 1:3). Then, the proposed scaled values are tested using the dynamic differential equations of the system. If the desired similitude is not achieved, the designer can formulate other interrelations of scaling laws and repeat the process. Some examples of the application of this method to scale mechanical systems are given by Simitses, 2001; Singhatanadgid and Ungbhakorn, 2002; Ungbhakorn and Wattanasakulpong, 2007.

1.5 Critical assessment of the state of the art

The monitoring of the process force provides crucial information about the quality of the process and the condition of the machine. Furthermore, the continuous monitoring of the process force may contribute to the detection of failures and undesired events that can compromise the integrity of the machine.

Among the reviewed force monitoring techniques, soft sensors have more advantages with respect to hardware sensors, since they overcome two of the main handicaps associated to hardware sensors: their economic cost and the frequent drift they suffer. Besides, in the case of mechanical presses, the MBSS approach is preferable to DDSS approach, since several authors have already proposed models of servo press components. The estimations carried out by means of MBSSs are more intuitive, since the model describes the physical phenomena of the system. Among modelling techniques, the Lagrange approach avoids the main handicaps of the Newton-Euler and kineto-static approaches. On the one hand, Lagrange method does not require to define all the kinematic constraints of rigid bodies of Newton-Euler approach. On the other hand, unlike the kineto-static approach, Lagrange method does not neglect the speed variation of system components. The removal of speed variations of components can introduce inaccuracies in the dynamic of the system.

Among analysed MBSSs almost all the algorithms have their limitations. In the case of the LO and KF, they cannot cope with nonlinear systems. EKF, UIO and EUIO may introduce large errors in estimations due to their linearisation step. In respect of UKF, although it overcomes the linearisation limitation of EKF, it can only assume Gaussian probability distributions of estimands uncertainties. PEM and MCMC instead, can provide robust estimations of parameters as they process the received measurements in batch. Regarding the simultaneous estimation of states and an unknown input a modified version of the dPF might be suitable, as it can decouple the particles evaluated in its both PFs.

Due to the slow execution time and high computational effort associated to MC methods, hardware based accelerators have been reviewed. Among them, hardware devices equipped with an FPGA have shown better performance than other devices such as multi-core CPUs and GPUs, due to their larger on-chip memory and its reconfigurable nature.

Test benches allow to test different set-ups of the machine in a controlled environment, without compromising the integrity of the original system when testing extreme operations. Among the analysed scaling methods, Buckingham's π theorem based dimension analysis is simpler than the differential equations method. Buckingham's π only takes into account the magnitudes of the system to be scaled and there is no need of formulating and analytical differential equation model. In the differential equations method the interrelations of scaling laws are created arbitrarily and scaling laws are tested several times through the differential equations, repeating the process until the dynamic similitude with the original system is achieved. Nonetheless, the scaling laws formulated by Buckingham's π method allows to define system's estimands in infinite ways,

while keeping the dynamic similitude with the original system.

1.6 Hypothesis of the dissertation

The hypothesis of this thesis is that a MBSS is able to estimate simultaneously the process force and the dynamic behaviour of a servo press using exclusively already available angular position and current signals of the servomotor and a model of the system.

1.7 Objectives of the dissertation

The main objective of this thesis entitled "Soft sensor based servo press monitoring" is to estimate process forces and the dynamic behaviour of a servo press by means of a novel version of the dPF.

To achieve the stated objective, five operative objectives were defined:

- O_1 To develop and validate a model that defines the dynamic behaviour of a servo press perturbed by an external process force.
- O_2 To propose a MBSS able estimate simultaneously the process force and the dynamic behaviour of a servo press.
- O_3 To design and manufacture a scaled test bench of a servo press to validate the developed model and the proposed algorithm in a controlled environment.
  - O_{31} To design a scaled test bench of a servo press keeping a dynamic similitude with the original system.
  - O_{32} To validate the manufactured scaled servo press by means of experimental signals, comparing the dynamic similitude with the original servo press.
  - O_{33} To validate the novel version of the algorithm in the manufactured scaled test bench of the servo press.
- O_4 To implement the validated model and the proposed MBSS in hardware for accelerating the computational time.
  - O_{41} To design a hardware architecture to implement the proposed MBSS.
  - O_{42} To validate the hardware implementation experimentally.
- O_5 To validate the proposed MBSS and its hardware implementation under different metal forming processes in a real servo press.

1.8 Methodology

The dissertation begins reviewing the already available solutions to monitor the servo press force in real time, analysing their advantages and limitations. Owing to the handicaps of hardware or physical sensors in terms of the drift they suffer, their cost and installation constraints, the path of the software based sensors is raised. Regarding the two branches of soft sensors, MBSSs are found more suitable than DDSSs for the servo press use case, since the mechanisms of servo presses and the processes they perform are already analysed in the literature by means of analytical models. Among the wide variety of MBSS, the so-known Monte Carlo methods are selected as they are the most generalist algorithms, due to the fact that they make fewer assumptions than other MBSSs about the nature of the model they are interacting with. To reduce the computational effort and accelerate the slow execution time associated to MC methods, the implementation of a hardware architecture is proposed, which allows to accelerate the algorithms within MC methods to achieve a real time execution.

A servo press analytical dynamic model is developed using Lagrange method, including all the components that participate in the dynamic behaviour of the system. The model is experimentally validated by means of unloaded servo press operations, taking advantage of the signals acquired from the control system of the servo press.

Once the model is validated a novel MBSS is proposed and developed, able to carry out the simultaneous estimation of an unknown input (input force) and the states of the system. The MBSS is validated in a 2DoF simulated system. Then, a hardware implementation of developed MBSS is raised to accelerate the execution time.

To validate both, the developed dynamic model of the servo press and the MBSS, in a controlled lab environment, a test bench is designed and manufactured. The design of the test bench is accomplished by means of a methodology that allows to emulate the dynamic behaviour of the real servo press of the use case. Besides, the test bench overcomes two of the main handicaps subjected to the real servo press, its low availability and the possibility of damaging the press with extreme condition experiments.

Having validated the model and the MBSS in the test bench, the proposed monitoring technique is deployed in an industrial servo press. Three different metal forming processes are monitored with the proposed MBSS.

1.9 Outline of the dissertation

The rest of the dissertation is organized as follow:

Chapter 2 presents the model of the servo press, which includes the modelling of both the electrical subsystem and the mechanical subsystem. The dynamic behaviour of the developed model is validated with experimental signals. Chapter 3 describes the proposed MBSS to estimate the

process force and the dynamic behaviour of a servo press. The proposed dPF MBSS and its hardware implementation are addressed in this chapter. Chapter 4 tackles the validation of the proposed dPF in a lab environment. A test bench has been designed using a scaling methodology known as the Buckingham's π method. The designed and manufactured test bench has been used for the validation of both the servo press model and the dPF MBSS. Chapter 5 discusses the validation of the proposed dPF in an industrial servo press facility under three metal forming processes and shows the hardware implementation of the dPF in a hybrid device that combines a multi-core CPU and an FPGA. Chapter 6 includes some conclusions drawn from this research work and poses future research lines to follow.

1.10 Publications

Some of the work developed during this dissertation is already published in various book chapters, conferences and journals:

- Olaizola, J., Abete, J. M., Iturrospe, A., & de Argandoña, E. S. "Modelling, Simulation and Validation of a Ram-Crank Servo Driven Press", Conferencia Internacional sobre Tecnologías aplicadas a las Redes Eléctricas Inteligentes CITREI 2018, 26-30 noviembre 2018, La Habana, Cuba. ISBN 978-959-261-585-4.
- Cucek, V., Albano, M., Abete, J. M., Inza, I. B., De Brabandere, K., Etxabe, A., ... & Olaizola, J. (2019). Monitoring of Critical Assets. The MANTIS Book: Cyber Physical System Based Proactive Collaborative Maintenance, 93.
- Larrinaga, F., Fernandez-Anakabe, J., Zugasti, E., Garitano, I., Zurutuza, U., Olaizola, J., ... & Mondragon, M. (2019). A Big Data implementation of the MANTIS reference architecture for predictive maintenance. Proceedings of the Institution of Mechanical Engineers, Part I: Journal of Systems and Control Engineering, 0959651819835362.
- Olaizola, J., Bouganis, C. S., de Argandoña, E. S., Iturrospe, A., & Abete, J. M. (2019). Real-time servo press force estimation based on dual Particle Filters. IEEE Transactions on Industrial Electronics.

Chapter 2

Modelling of the servo press

This chapter presents the works carried out to develop a model of a servo press able to describe the machine's dynamic behaviour. It comprises the modelling methodology of both, the electrical subsystem composed of a PMSM servomotor and the mechanical subsystem composed of the kinematic chain. Besides, a friction model that represents the friction among the components of the kinematic chain of the servo press system is also posed. Finally the developed model is experimentally validated.

The servo press analysed during the dissertation is the Fagor Arrasate's model SDM2-400-2400-1200, which is powered by a PMSM servomotor. It is able to exert a maximum force of 4000 kN (throughout the document the force is expressed in tonnes instead of Newtons, as tonnes are the common unit used in the metal forming industry). As presented in section "MBSS: Servo press modelling", a servo press is composed of a mechanical and an electrical subsystems. Next sections address the derivation of both subsystems to achieve the complete model of the servo press.

2.1 Electrical subsystem

Regarding the modelling of the electrical subsystem, there are many publications in the literature that provide a mathematical model of the PMSM (Gieras et al. Gieras, 2002, Jianbo et al. Jianbo et al., 2009 and Benjak et al. Benjak and Gerling, 2010).

A PMSM is formed by a stator that contains windings supplied with current to produce a rotating magnetic field, and by a rotor shaft which is manufactured with permanent magnets providing a constant magnetic field as shown in figure 2.1.

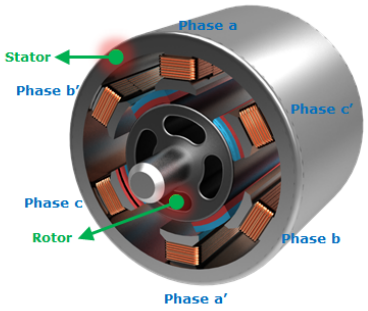

Figure 2.1: A PMSM's internal structure (functionbay, 2016).

When controlled, these two magnetic fields exert an electric torque τ_e that makes the rotor rotate. The voltage that flows across the stator windings is defined in a state space representation as in (2.1).

$$\begin{bmatrix} v_a \\ v_b \\ v_c \end{bmatrix} = \begin{bmatrix} R & 0 & 0 \\ 0 & R & 0 \\ 0 & 0 & R \end{bmatrix} \begin{bmatrix} i_a \\ i_b \\ i_c \end{bmatrix} + \frac{d}{dt} \begin{bmatrix} \phi_a \\ \phi_b \\ \phi_c \end{bmatrix} \tag{2.1}$$

where:

- v_a, v_b, v_c are the phase voltages of each stator winding,
- R is the equivalent resistance of each stator winding,
- i_a, i_b and i_c are currents flowing in each stator winding,
- ϕ_a, ϕ_b and ϕ_c are the total magnetic fluxes in each stator winding.

The permanent magnets and the stator windings contribute to the total flux that links each winding as shown in (2.2).

$$\begin{bmatrix} \phi_a \\ \phi_b \\ \phi_c \end{bmatrix} = \begin{bmatrix} L_{aa} & L_{ab} & L_{ac} \\ L_{ba} & L_{bb} & L_{bc} \\ L_{ca} & L_{cb} & L_{cc} \end{bmatrix} \begin{bmatrix} i_a \\ i_b \\ i_c \end{bmatrix} + \frac{d}{dt} \begin{bmatrix} \phi(t)_{am} \\ \phi(t)_{bm} \\ \phi(t)_{cm} \end{bmatrix} \tag{2.2}$$

where:

- L_{aa}, L_{bb}, L_{cc} are the self-inductances of the stator windings,
- $L_{ab} = L_{ba}, L_{bc} = L_{cb}, L_{ac} = L_{ca}$ are the mutual inductances of the stator windings,
- $\phi(t)_{am}, \phi(t)_{bm}$ and $\phi(t)_{cm}$ are the permanent magnets fluxes linking the stator windings.

Stator inductances can be represented as a function of the rotor's electrical angle, as stated by Ohm, 2000. The electrical angle is obtained from the product of the rotor's angle and the number of pairs of poles of permanent magnets. For the sake of simplicity, a mathematical transformation is derived from the three phase equations using the Park's transform (Park, 1929). This method provides a way for translating the three phase reference frame equations to a rotary direct-quadrature-zero (dq0) frame where the rotor's electrical angle is considered in the equations.

Figure 2.2 shows the Park's transformation diagram that reduces the number of equations governing the PMSM's stator: from three (abc frame) phases to two (dq0 frame) phases.

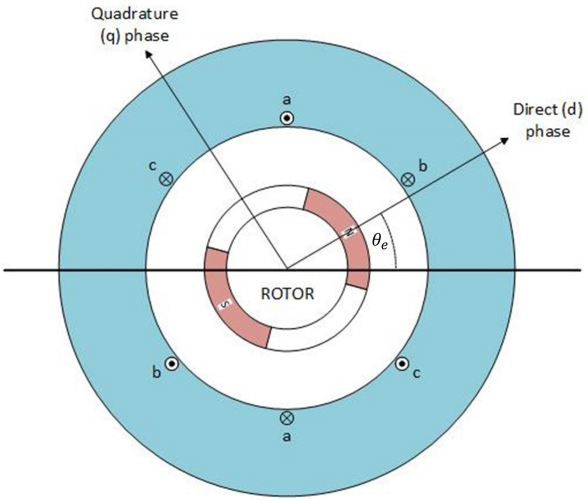

Figure 2.2: Axial view of a conceptual PMSM motor.

Knowing that the three phases of the PMSM are shifted 120° ($2\pi/3$), the dq0 equations are derived using the Park's transform matrix shown in (2.3):

$$T = \frac{\sqrt{2}}{3}\begin{bmatrix} \cos(\theta_e) & \cos(\theta_e - 2\pi/3) & \cos(\theta_e + 2\pi/3) \\ -\sin(\theta_e) & -\sin(\theta_e - 2\pi/3) & -\sin(\theta_e + 2\pi/3) \\ 1/2 & 1/2 & 1/2 \end{bmatrix} \tag{2.3}$$

where θ_e is the electrical angle defined as $\theta_e = p\theta_r$, p being the number of pole pairs of the rotor and θ_r the angle of rotor. Thus, the dq0 frame voltage and current equations are represented in (2.4).

$$\begin{bmatrix} v_d \\ v_q \\ v_0 \end{bmatrix} = T \begin{bmatrix} v_a \\ v_b \\ v_c \end{bmatrix} \qquad \begin{bmatrix} i_d \\ i_q \\ i_0 \end{bmatrix} = T \begin{bmatrix} i_a \\ i_b \\ i_c \end{bmatrix} \tag{2.4}$$

If the stator windings are balanced, the 0 axis of the dq0 reference frame is 0. Applying the Park's transformation, the currents that flow across the stator windings are expressed as in (2.5).

$$\frac{d}{dt}\begin{bmatrix} i_d \\ i_q \end{bmatrix} = \begin{bmatrix} \frac{p\dot{\theta}_r i_q L_q}{L_d} - \frac{Ri_d}{L_d} + \frac{v_d}{L_d} \\ -\frac{Ri_q}{L_q} - \frac{p\dot{\theta}_r(i_d L_d + \phi_m)}{L_q} + \frac{v_q}{L_q} \end{bmatrix} \tag{2.5}$$

where :

- L_d and L_q are the d-axis and q-axis stator inductances respectively,
- $\dot{\theta}_r$ is the angular speed of the rotor.

Finally, the electric torque τ_e exerted by the PMSM can be defined (Zhu, 2008; Esteban et al., 2016), as in (2.6).

$$\tau_e = \frac{3}{2}p(i_q(i_d L_d + \phi_m) - i_d i_q L_q) \tag{2.6}$$

In many industrial applications, the control schemes such as the FOC (Plunkett, 1989; Suja et al., 2016) minimise the direct current i_d to reduce the reactive power associated to a power loss in the form of heat. Thus, the control tries to maximise the active power to produce the maximum torque as claimed by Jianbo et al., 2009. Therefore, the direct current i_d is considered as 0, yielding a simplified expression for τ_e as in (2.7).

$$\tau_e = K_t i_q \tag{2.7}$$

being $K_t = (3/2)p\phi_m$ the constant provided by the manufacturer of the PMSM. The electric part of the PMSM and its mechanical part are coupled as shown in (2.8).

$$\tau_e = J\ddot{\theta}_r + B\dot{\theta}_r \tag{2.8}$$

where J, B and $\ddot{\theta}_r$ are the rotor's inertia, the viscous friction and rotor's acceleration respectively. Viscous friction is caused by the lubrication of the PMSM's bearings and the aerodynamic drag generated moving the rotor (Chin et al., 2018).

2.2 Mechanical subsystem

The model of the mechanical subsystem of the servo press takes into account the gearbox, the crankshaft, the two connecting rods, the ram and the pneumatic load balancer. The torques and forces that actuate over the mechanical subsystem are also considered in the model: the friction torque (that includes the friction forces transmitted to the crankshaft), the process force and the electric torque of the servomotor. Figure 2.3 illustrates the above mentioned magnitudes.

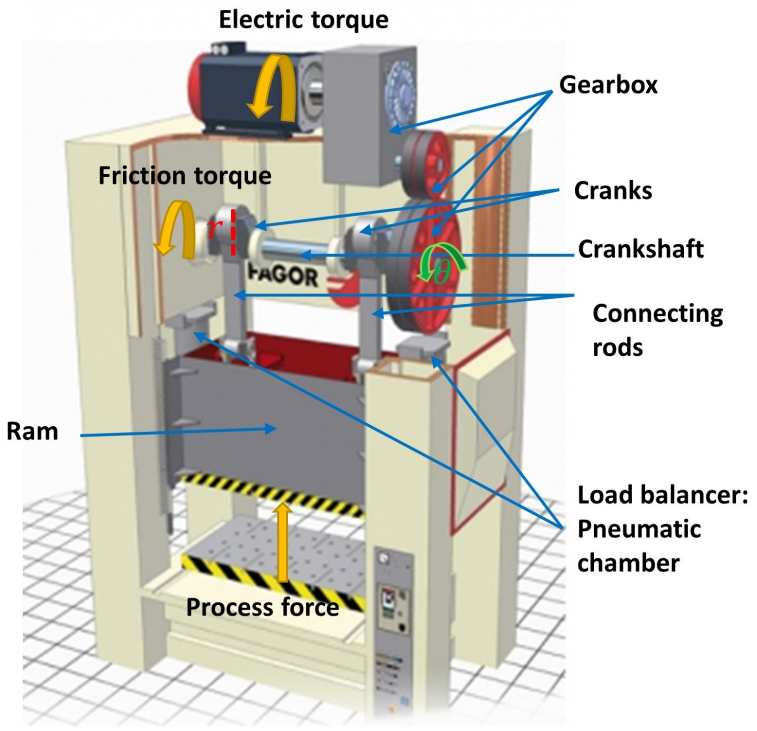

Figure 2.3: Magnitudes included in the mechanical subsystem.

The equation of the dynamic model for the mechanical subsystem is derived using the Lagrange method. All the states, parameters and inputs of the servo press listed in table 2.1 are included on the model equation. The values of parameters defined in the table were obtained from a computer aided design (CAD), measuring the lengths, the masses and the inertia values of components.

	Definition	**Value**
States		
θ	Angular position of the crankshaft	$(-)rad$
$\dot{\theta}$	Angular speed of the crankshaft	$(-)rad/s$
$\ddot{\theta}$	Angular acceleration of the crankshaft	$(-)rad/s^2$
Parameters		
r	Radius of the crank	$0.2m$
$\acute{r}$	Distance between the axis of the crank and its centre mass	$0.0762m$

l	Length of the connecting rod	$1.05m$
$\acute{l}$	Distance between the axis of the connecting rod and its centre mass	$0.327m$
I_1	Inertia of the crankshaft	$80.92kg/m^2$
m_1	Mass of the crankshaft (only the eccentricity i.e. cranks)	$424kg$
I_2	Inertia of the two connecting rods	$66.4 \times 2kg/m^2$
m_2	Mass of the two connecting rods	$412.93 \times 2kg$
m_3	Mass of the ram	$11600kg$
I_4	Inertia of the 1st gear of the gearbox	$105.77kg/m^2$
I_5	Inertia of the 2nd gear of the gearbox	$19.007kg/m^2$
I_6	Inertia of the 3rd gear of the gearbox	$3.58kg/m^2$
I_7	Inertia of the servomotor's rotor	$7.38kg/m^2$
η_4	Reduction ratio of the 1st gear of the gearbox	$60/17$
η_5	Reduction ratio of the 2nd gear of the gearbox	$60/17$
η_6	Reduction ratio of the 3rd gear of the gearbox	$71/18$
η	Reduction ratio of the gearbox	$\eta_4\eta_5\eta_6$
g	Gravitational acceleration constant	$9.81m/s^2$
Inputs		
F_{ms}	Force of the process	$(-)N$
F_{lb}	Force of the load balancer	$(-)N$
τ_e	Electric torque of the PMSM	$(-)Nm$
τ_{fric}	Friction torque	$(-)Nm$

Table 2.1: List of symbols included in the servo press model.

The load balancer (figure 2.4) is modelled as a pneumatic chamber, whose pressure fluctuates proportional to the linear displacement of the ram. Therefore, the force F_{lb} produced by the load balancer also varies proportional to the linear displacement of the ram. The model of the load balancer is represented in (2.9).

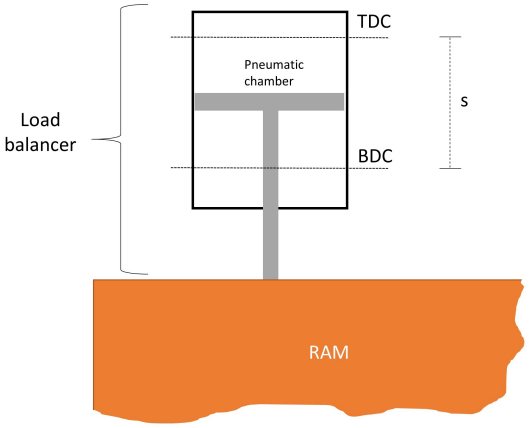

Figure 2.4: Schematic diagram of a pneumatic load balancer.

$$\begin{aligned} s &= r - l + r\cos(\theta) + \sqrt{l^2 - r^2 sin^2(\theta)} \\ F_{lb} &= (p_m s + p_i)\, A \end{aligned} \tag{2.9}$$

where s is the linear displacement of the ram, $p_m = 300\text{kPa}$ represents the slope of the pressure variation, $p_i = 400\text{kPa}$ is the initial pressure and $A = 0.029m^2$ is the area of the load balancer.

The Lagrange method derivations starts obtaining the energy expression of the mechanical subsystem denoted as the Lagrange function (2.10), which represents the difference between the kinetic and potential energies.

$$L = T - V \tag{2.10}$$

L, T and V are the Lagrange function, the kinetic energy and the potential energy of the system respectively. The general form of Lagrange's equations of motion is given by (2.11):

$$\frac{d}{dt}\left(\frac{dL}{d\dot{q}_k}\right) - \frac{dL}{dq_k} = Q_k \qquad k = 1, 2, ..n \tag{2.11}$$

where q_k is the state variable of the energy system, $\dot{q}_k$ the derivative of q_k, Q_k represents the generalized state variable and n is the number of generalised state variables (Ha et al., 2006).

The kinematic relations of the mechanical subsystem's components are used to define the kinetic and potential energies of the Lagrange's function. The components that perform a translational motion are the crankshaft, the connecting rods and the ram depicted in red in figure 2.5. The crankshaft and the connecting rod also perform a rotational motion, as well as the gearbox's gears and the rotor.

The kinematic equations of these components are defined by trigonometric functions representing the motion of their centres of gravity (c_{g1}, c_{g2}, c_{g3}) as shown from equation (2.12) to (2.15).

$$x_{c_{g1}} = \acute{r}\sin(\theta) \qquad y_{c_{g1}} = \acute{r}\cos(\theta) \tag{2.12}$$

$$x_{c_{g2}} = \left(l - \acute{l}\right)\sin(\beta) \qquad y_{c_{g2}} = -\left(r\cos(\theta) + \acute{l}\cos(\beta)\right) \tag{2.13}$$

$$x_{c_{g3}} = 0 \qquad y_{c_{g3}} = -\left(r\cos(\theta) + l\cos(\beta)\right) \tag{2.14}$$

$$\dot{\beta} = \frac{r\cos(\theta)\dot{\theta}}{c} \qquad c = \sqrt{l^2 - r^2\cos^2(\theta)} \tag{2.15}$$

The kinetic T and potential V energies of (2.10) are defined in (2.16) and (2.17) respectively,

based on the above presented kinematic equations (2.12)-(2.15) and the masses and inertias of the rest of components that perform a rotational motion.

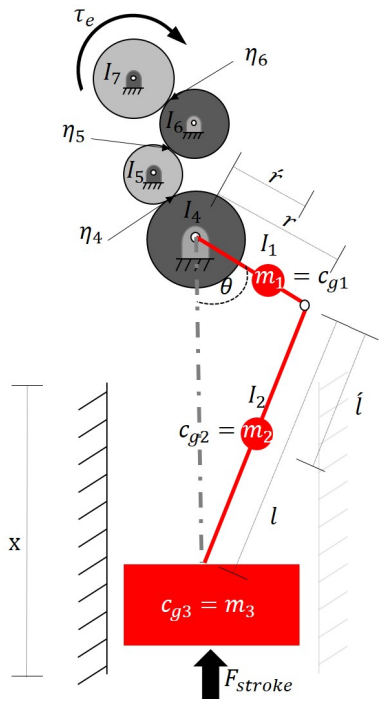

Figure 2.5: Diagram of the mechanical subsystem.

$$T = \frac{1}{2}\dot{\theta}^2 \left(I_1 + m_1\acute{r}^2 + \frac{I_2 r^2 \cos^2(\theta)}{c^2} + \frac{\left(l - \acute{l}\right)^2}{l^2} m_2 r^2 \cos^2(\theta) + \sin^2(\theta) \right.$$
$$\left. \left(m_2 r^2 \frac{\left(r\acute{l}\cos(\theta) + lc\right)^2}{l^2 c^2} + m_3 r^2 \frac{(r\cos(\theta) + c)^2}{c^2} \right) + I_4 + I_5\eta_4^2 + I_6\eta_4^2\eta_5^2 + I_7\eta_4^2\eta_5^2\eta_6^2 \right) \tag{2.16}$$

$$V = -g\left(\cos(\theta)\left(m_1\acute{r} + m_2 r + m_3 r\right) + m_2\frac{\acute{l}}{l}c + m_3 c \right) \tag{2.17}$$

Equations (2.16) and (2.17) are substituted in (2.10), yielding the Lagrange function as in (2.18).

$$L = \frac{1}{2}\dot{\theta}^2 \left(I_1 + m_1\acute{r}^2 + \frac{I_2 r^2 \cos^2(\theta)}{c^2} + \frac{\left(l - \acute{l}\right)^2}{l^2} m_2 r^2 \cos^2(\theta) + \sin^2(\theta) \right.$$
$$\left(m_2 r^2 \frac{\left(r\acute{l}\cos(\theta) + lc\right)^2}{l^2 c^2} + m_3 r^2 \frac{(r\cos(\theta) + c)^2}{c^2} \right) + I_4 + I_5\eta_4^2 + I_6\left(\eta_4\eta_5\right)^2 \tag{2.18}$$
$$\left. + I_7\left(\eta_4\eta_5\eta_6\right)^2 \right) + g\left(\cos(\theta)\left(m_1\acute{r} + m_2 r + m_3 r\right) + m_2\frac{\acute{l}}{l}c + m_3 c \right)$$

Using the Lagrange method, the dynamic equation of the mechanical subsystem is obtained, deriving the Lagrange's equations of motions with respect to $q_k = \theta$, as defined in (2.11). The derivation of the Lagrange's equations of motion is described in Appendix A, where equation (2.11)'s derivatives are solved. The dynamic equations of the external forces are also derived by means of the virtual work method. The complete dynamic equation is represented in (2.19).

$$\begin{aligned}
\ddot{\theta}\Bigg(I_1 + m_1\acute{r}^2 + \frac{I_2 r^2\cos^2(\theta)}{c^2} + \frac{\left(l-\acute{l}\right)^2}{l^2}m_2 r^2\cos^2(\theta) + \sin^2(\theta)\Bigg(m_2 r^2\frac{\left(r\acute{l}\cos(\theta)+lc\right)^2}{l^2c^2} \\
+m_3 r^2\frac{(r\cos(\theta)+c)^2}{c^2}\Bigg) + I_4 + I_5\eta_4^2 + I_6\left(\eta_4\eta_5\right)^2 + I_7\left(\eta_4\eta_5\eta_6\right)^2\Bigg) \\
+\frac{1}{2}\dot{\theta}^2\Bigg(\frac{2I_2 r^4\cos^3(\theta)\sin(\theta)}{c^4} - \frac{2I_2 r^2\cos(\theta)\sin(\theta)}{c} - \frac{2m_2 r^2\cos(\theta)\sin(\theta)\left(l-\acute{l}\right)^2}{l^2} \\
+2\sin(\theta)\cos(\theta)\Bigg(m_2 r^2\frac{\left(r\acute{l}\cos(\theta)+lc\right)^2}{l^2c^2} + m_3 r^2\frac{(r\cos(\theta)+c)^2}{c^2}\Bigg) + 2\sin^2(\theta) \\
\Bigg(\frac{m_2 r^3\acute{l}\sin(\theta)\left(r\acute{l}\cos(\theta)+lc\right)(r\cos(\theta)-c)(r\cos(\theta)+c)}{l^2c^4} \\
\frac{m_3 r^3\sin(\theta)(r\cos(\theta)+c)^2(r\cos(\theta)-c)}{c^4}\Bigg)\Bigg) \\
+g\Bigg(\sin(\theta)\left(m_1\acute{r}+m_2 r+m_3 r\right) + \sin(\theta)\cos(\theta)\left(\frac{m_2 r^2\acute{l}}{lc} + \frac{m_3 r^2}{c}\right)\Bigg) \\
= \tau_e\eta - \tau_{fric} - \left(F_{ms}+F_{lb}\right)r\sin(\theta)\left(1+\frac{r\cos(\theta)}{c}\right)
\end{aligned} \tag{2.19}$$

Note that the electrical subsystem and the mechanical subsystem are coupled in the above equation, since the electric torque τ_e, the rotor's inertia $J = I_7$ and the viscous friction's effect $\tau_{fric}\left(B\dot{\theta}\right)$ are included in the dynamic model's equation.

The next subsection addresses the characterisation of the friction torque that interacts with the servo press model.

2.2.1 Static friction model

The torque consumed by the different friction phenomena that take place in the servo press is described by means of a friction model, as presented by Chiew et al., 2013 and Virgala et al., 2013 for servomotors with kinematic chains or by C. Liu et al., 2017 for servo presses. This friction model is widely used in engineering applications, since it is able to describe many friction phenomena such as the static friction f_s, the Coulomb friction f_c and the viscous friction f_v.

The static friction torque is the torque that keeps the servo press system at rest. Coulomb's friction torque opposes rotational motion with a constant torque at any angular speed. Viscous friction coefficient represents a torque that is proportional and contrary to the angular speed of the kinematic chain. Besides, v_s describes the characteristic curve of the Stribeck friction, which represents the friction of a low speed sliding among components of the servo press. This friction model captures the sliding frictions among the surfaces of different components such as the gears and bearings. The combined model is defined in (2.20).

$$\tau_{fric} = sgn\left(\dot{\theta}\right)\left(f_c + (f_s - f_c)\, e^{-\left(\frac{\dot{\theta}}{v_s}\right)}\right) + f_v\dot{\theta} \tag{2.20}$$

$sgn\left(\dot{\theta}\right)$ is obtained as in 2.21.

$$sgn\left(\dot{\theta}\right) = q\begin{cases} 1 & \dot{\theta} > 0 \text{ crankshaft rotating clockwise} \\ 0 & \dot{\theta} = 0 \text{ crankshaft stopped} \\ -1 & \dot{\theta} < 0 \text{ crankshaft rotating counterclockwise} \end{cases} \tag{2.21}$$

The methodology to model the effect of friction is explained next:

- Several unloaded ($F_{ms} = 0$) servo press operations are carried out at different speeds.
- PMSM's three phase currents I_{abc} and rotor's angular position signal θ_r are measured using a sampling frequency of $f_s = 4$kS/s. These signals are acquired from the control device of the servo press, without installing additional sensors. Those signals are used to calculate the electric torque $\tau_e(I_{abc}, \theta_r)$ and the angular position of the crankshaft $\theta = \theta_r/\eta$. The calculated signals are filtered using a low pass filter with a cutting frequency of $fc = 100$Hz to remove higher frequencies, since they are not representative of the servo press's slower dynamic.
- Model (2.19) is solved for τ_{fric}, as it is the only unknown magnitude. Measured θ, $\dot{\theta}$ and $\ddot{\theta}$ and calculated τ_e signals are introduced in the model to obtain a signal that captures the τ_{fric}.
- Friction model's coefficients are estimated using the PEM algorithm. The input signal used by PEM is the friction torque τ_{fric}. The angular position θ, speed $\dot{\theta}$ and acceleration $\ddot{\theta}$ of the crankshaft have been used as output signals.

2.3 Validation of the servo press model

This section tackles the validation of the servo press model, including the proposed friction model. First the friction model is fitted using experimental signals. Then, the dynamic model of the servo press is evaluated and validated through unloaded experiments.

Based on the methodology presented in subsection 2.2.1, the coefficients' values proposed by PEM to fit the friction model are $f_s = 1572Nm$, $f_c = 2140Nm$, $f_v = -2906Ns/m$ and $v_s = 5546rad/s$. (Note: the estimated values are rounded to the nearest integer). The signal obtained by the fitted model (2.20) is illustrated in figure 2.6, along with the friction torque signal calculated by solving (2.19) for τ_{fric}. The absolute error between the calculated and the modelled torques is also shown. Looking at either the model fit graph or the absolute error graph, some unmodelled dynamics can be noticed. Some of the phenomena that could explain such dynamics are the effects of clearances of servo press's joints. The fluctuations in the absolute error between seconds $1-7$ show a sinusoidal dynamic behaviour that could correspond to the angular position of the different joints of the servo press. The maximum absolute error obtained is $906Nm$. Regarding the fast transitions around seconds 1 and 7, those downwards peaks are introduced by the low pass filter.

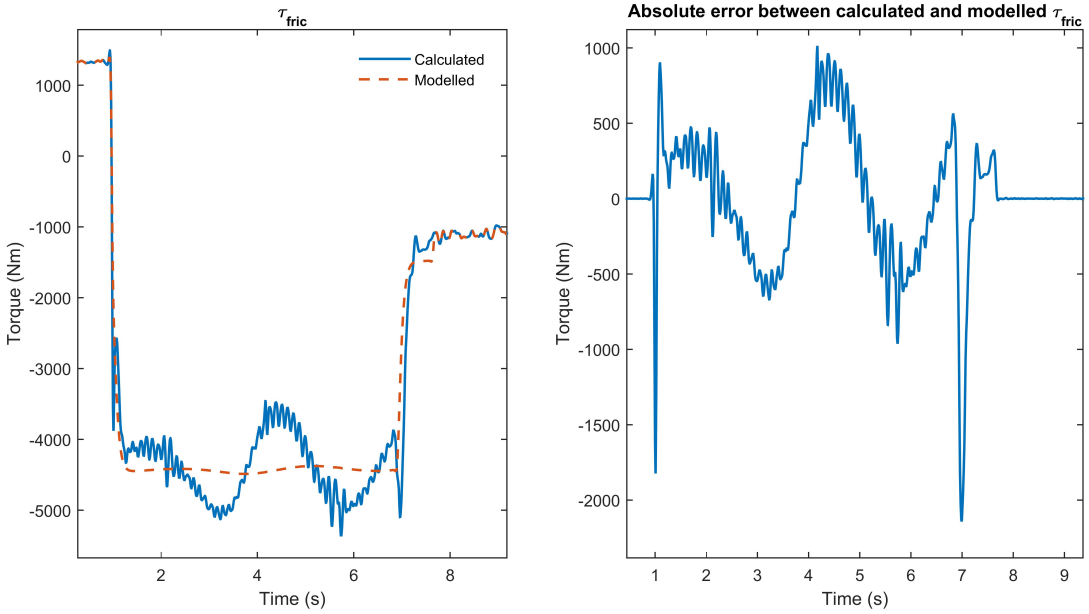

Figure 2.6: Torque signal consumed by the system's friction.

Regarding the validation of the complete model of the servo press, PMSM's three phase current I_{abc} and rotor's angular position signal θ_r have been acquired from the control device of the servo press using a sampling frequency of $f_s = 4$kS/s. Signals have been measured during a single working cycle of the servo press under unloaded conditions ($F_{ms} = 0$). $\tau_e(I_{abc}, \theta_r)$ and $\theta = \theta_r/\eta$ have been obtained from the measured signals and have been filtered using a low pass filter with a cutting frequency of $fc = 100$Hz. τ_e has been used as an input of the servo press model and the three states of the model $\left(\theta, \dot{\theta}, \ddot{\theta}\right)$ have been simulated and compared with the measured θ and its derivatives (angular speed and angular acceleration).

Figure 2.7 shows the evolution of the three states during a working cycle of the servo press, comparing simulation results with measured signals. The absolute error in the three states show a varying error during the working cycle of the servo press. As concluded in section 2.2.1, the

varying error might be due to unmodelled dynamics of the servo press, such as the frictions and clearances in servo press's joints. These phenomena should be investigated in future works.

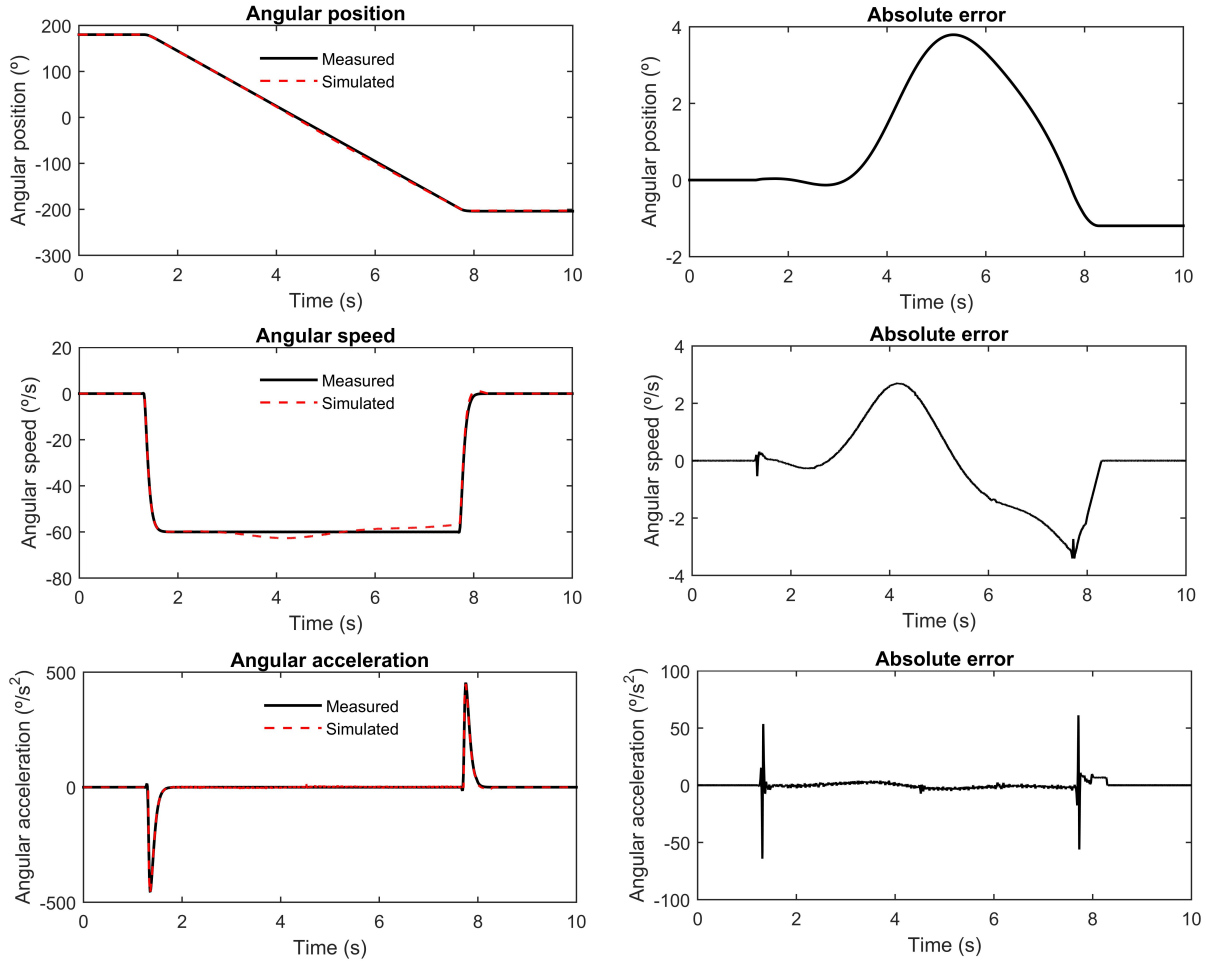

Figure 2.7: Validation of the servo press model's states.

Next chapter presents a novel monitoring solution to estimate the states and the process force of the servo press simultaneously.

Chapter 3

Proposed monitoring solution

In this chapter a dual particle filter (dPF) MBSS is proposed to estimate simultaneously the states and the process force of the analysed servo press. In the first sections of this chapter the formulation of the dPF is presented and then the algorithm is evaluated and validated in a simulated 2DoF system.

The second section tackles the hardware implementation of the dPF and proposes a metric to assess the quality of the estimations under the selected hardware parameters. The hardware implementation of the algorithm is carried out for the simulated 2DoF system.

3.1 The dual Particle Filter

This section presents the formulation of the proposed dPF and the tuning of its parameters. Then, the algorithm is applied to a 2DoF system.

3.1.1 Overview of PF

PF is a sequential Monte Carlo method that is frequently used for recursively estimating (in k iterations) system's states based on the posterior probability of generated particles x_k^i. Each particle represents the state vector at time step k. These particles are usually selected by the importance sampling techniques (Gordon et al., 2004), which associate a likelihood weight $W_{x_k}^i$ to the generated (sampled) particle x_k^i. Particles are sampled based on the state vector estimated in the previous iteration $\hat{\boldsymbol{x}}_{k-1}$ and a variance vector $\boldsymbol{q}_x$ that must capture all the range of values that a state can acquire during the experiment.

The likelihood weight of each particle $[x_k^i, W_x^i]$ represents the probability of that particle being

sampled from the probability density function defined by the measurements, as in (3.1).

$$p(x_k, |Y_k) \approx \sum_{i=1}^{N_x} W_{x_k}^i \delta(x_k - x_k^i) \tag{3.1}$$

where $Y_k = y_1, y_2, .., y_k$ is a set of accumulated measurements up to time k and is defined as $y_k = h_k(x_k) + v_k$, where $h_k(\cdot)$ and v_k are the measurement function and measurements noise respectively. δ is the Dirac delta function, and N_x is the number of particles. PF employs four steps to carry out the estimation of states: the Prediction & Update step, the Normalization step, the Resampling step and the Averaging step, as described in Algorithm I on table 3.1, where a general PF is detailed for a single available measurement y_k.

Algorithm I	
STATES PF STEPS	
	For i=1..N_x - Prediction & Update loop
(a)	Propagate previous estimated state particles $\boldsymbol{x}_{k-1}^i = \hat{\boldsymbol{x}}_{k-1}^i$ through the model $g_k(\cdot)$ to obtain predicted states particles $\bar{\boldsymbol{x}}_k^i = g_k(\hat{\boldsymbol{x}}_{k-1}^i, \boldsymbol{u}_k, \boldsymbol{\omega}_k)$
(b)	Sample proposal state particles from predicted state particles with a variance vector $\boldsymbol{q}_x$ associated with the process noise $\boldsymbol{\omega}_k$, e.g., using a normal distribution $\tilde{\boldsymbol{x}}_k^i \sim N(\bar{\boldsymbol{x}}_k^i, \boldsymbol{q}_x)$
(c)	Calculate weights of proposal state particles using a weighting function for updating the particles, e.g., using a Gaussian function $W_{x_k}^i = \frac{1}{\sqrt{2\pi\sigma_x^2}} e^{\frac{(y_k - h_k(\tilde{x}_k^i))^2}{2\sigma_x^2}}$, σ_x^2 being the variance of the measurement associated to v_k.
	End
(d)	Normalise weights $W_{x_k}^i = \frac{W_{x_k}^i}{\sum_{j=1}^{N_x} W_{x_k}^j}$
(e)	Calculate the cumulative sum of the weights $CW_x^i = \sum_{i=1}^{N_x} W_{x_k}^i$
	For i=1..N_x - Resampling loop
(f)	Generate uniformly distributed random sample $r_u \sim U(0,1)$
	While $\mathbf{r_u} \leq \mathbf{CW_x^j}$
(g)	Resample state particles $\hat{\boldsymbol{x}}_k^i = \tilde{\boldsymbol{x}}_k^{r_u \leq CW_x^j}$
	$j = j + 1$
	End
	End
(h)	Calculate estimated state vector $\hat{\boldsymbol{x}}_k$ using an average function of the resampled particles: mean, mode or median.
	Go to step (a) for the next iteration

Table 3.1: PF's procedure for state estimation.

As the conventional PF is only able to estimate the states of the system, the next subsection proposes an algorithm to simultaneously estimate system states and a single unknown input.

3.1.2 dPF for Simultaneous States and Unknown Input Estimation

In this dissertation, a modified version of a dPF algorithm (Thrun et al., 2001) is proposed, extending the PF described in Algorithm I, that estimates the states of the system (PF-S), with an additional PF for the estimation of a single unknown input (PF-UI), as shown in Algorithm II of table 3.2. The key point of this approach lies in sharing estimations between the two PFs. Figure 3.1 illustrates the block diagram of the dPF.

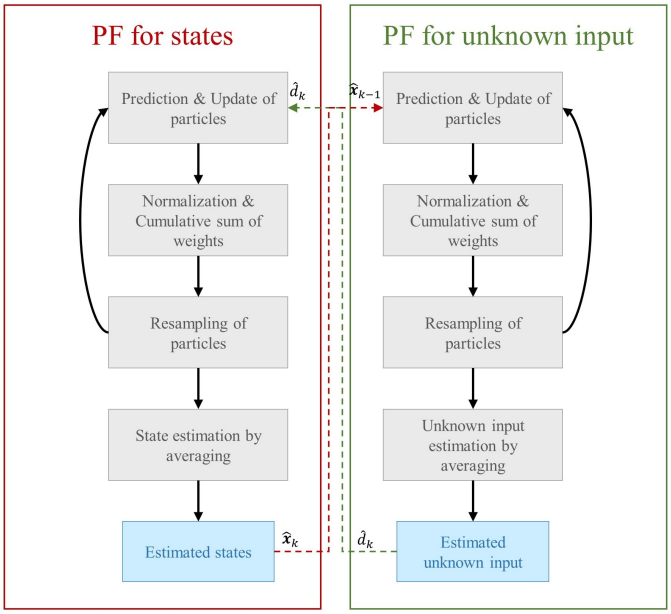

Figure 3.1: Block diagram of the proposed dPF.

In the dPF, each PF must include the estimation of the other PF in the Prediction & Update step, while keeping the rest of the steps the same. Each PF is executed independently including the estimation of the other one. The dPF begins with the PF-UI. Let us consider a dynamic system model that can be either linear or non-linear, which is in a dynamic equilibrium, with known inputs $\boldsymbol{u}_k$ and a single unknown input d_k, as in (3.2). A system is in dynamic equilibrium when the sum of all internal and external forces yield 0.

$$f_k(\boldsymbol{x}_{k-1}, \boldsymbol{u}_k, d_k, \boldsymbol{\omega}_k) = 0 \tag{3.2}$$

For each iteration k, the PF-UI samples N_d proposal particles for the unknown input $\tilde{d}_k^i$ based on previous estimations of both unknown input particles $\hat{d}_{k-1}^i$ and state vector $\hat{\boldsymbol{x}}_{k-1}$ estimated by the PF-S, as in (3.3).

$$\tilde{d}_k^i \sim p(\tilde{d}_k | \hat{d}_{k-1}, \hat{\boldsymbol{x}}_{k-1}) \quad i = 1, 2, ..N_d \tag{3.3}$$

To calculate the likelihood weight $W^i_{d_k}$ for each $\tilde{d}^i_k$ proposal particle, both $\tilde{d}^i_k$ and $\hat{\boldsymbol{x}}_{k-1}$ are propagated through the dynamic equilibrium model (3.2), obtaining a deviation Φ^i_k each $\tilde{d}^i_k$ produces, as in (3.4).

$$f_k(\hat{\boldsymbol{x}}_{k-1}, \boldsymbol{u}_k, \tilde{d}^i_k, \boldsymbol{\omega}_k) = \Phi^i_k \tag{3.4}$$

Then, $W^i_{d_k}$ is evaluated in (3.5) based on Φ^i_k and increases in value as Φ^i_k approximates to 0. In this way, the unknown input particles that are closer to the dynamic equilibrium $\Phi^i_k = 0$ acquire more importance by means of larger weights. The larger the weight of the $\tilde{d}^i_k$, the more precise the value it represents.

$$W^i_{d_k} \sim p(\Phi_k | \tilde{d}_k, \hat{\boldsymbol{x}}_{k-1}) \tag{3.5}$$

Once the rest of the PF-UI steps (Normalisation, Resampling and Averaging) are computed, the PF-S samples its proposal particles $\tilde{\boldsymbol{x}}^i_k$ using the current iteration's predicted state particles $\bar{\boldsymbol{x}}^i_k$. The predicted state particles are obtained by propagating the previous iteration's $\hat{\boldsymbol{x}}^i_{k-1}$ and the current iteration's estimated unknown input $\hat{d}_k$, as in (3.6).

$$\begin{aligned} \bar{\boldsymbol{x}}^i_k &= g_k(\hat{\boldsymbol{x}}^i_{k-1}, \boldsymbol{u}_k, \hat{d}_k, \boldsymbol{\omega}_k) \\ \tilde{\boldsymbol{x}}^i_k &\sim p(\tilde{\boldsymbol{x}} | \bar{\boldsymbol{x}}) \quad i = 1, 2, ..N_x \end{aligned} \tag{3.6}$$

The weights $W^i_{x_k}$ are then calculated, as in Algorithm I, taking advantage of the available measured states.

Algorithm II

UNKNOWN INPUT PF STEPS

For i=1..N_d - Prediction & Update loop

(a) Sample proposal unknown input particles from estimated unknown input particles and a variance q_d, e.g., $\tilde{d}^i_k \sim N(\hat{d}^i_{k-1}, q_d)$. q_d is associated to the maximum value d_k can get.

(b) Propagate proposal unknown input particles $\tilde{d}^i_k$ and the previous estimation of $\hat{\boldsymbol{x}}_{k-1}$ through the dynamic equilibrium model to get the deviation $\Phi^i_k = f_k(\hat{\boldsymbol{x}}_{k-1}, \boldsymbol{u}_k, \tilde{d}^i_k, \boldsymbol{\omega}_k)$

(c) Calculate weights of proposal particles $\tilde{d}^i_k$ using a weighting function for updating the particles, e.g., $W^i_{d_k} = \frac{1}{\sqrt{2\pi\sigma_d^2}} e^{\frac{(0-\Phi^i_k)^2}{2\sigma_d^2}}$. σ_d is associated to the maximum value Φ^i_k can take.

End

(d) Normalise weights $W_{d_k}^i = \frac{W_{d_k}^i}{\sum_{j=1}^{N_d} W_{d_k}^j}$

(e) Calculate the cumulative sum of the weights $CW_d^i = \sum_{i=1}^{N_d} W_{d_k}^i$

For i=1..N_d - Resampling loop

(f) Generate uniformly distributed random sample $r_u \sim U(0,1)$

While $\mathbf{r_u} \leq \mathbf{CW_d^j}$

(g) Resample state particles $\hat{d}_k^i = \tilde{d}_k^{r_u \leq CW_d^j}$

$j = j + 1$

End

End

(h) Calculate estimated unknown input $\hat{d}_k$ using an average function of the resampled particles: mean, mode or median.

Go to step (a) for the next iteration

Table 3.2: PF able to estimate an unknown input.

Tuning of the dPF

Some parameters of the dPF must be tuned according to the available measurements and the characteristics of the model. The variance vectors used in the weighting function $\boldsymbol{\sigma_x}$, $\boldsymbol{\sigma_d}$ and the variance vectors used in the proposal sampling $\boldsymbol{q_x}$, $\boldsymbol{q_d}$ must be set based on the variance of both, the unknown input and states, during the working cycle of the servo press. These parameters are adjusted experimentally so that they can represent the maximum variance of both, the unknown inputs and the states.

When selecting the number of particles for both PF-UI and PF-S, N_x and N_d, the designer has to deal with a trade-off between computational cost and the precision of the estimate. Different combinations of particle numbers must be tested to find the minimum values for N_x and N_d that provide an acceptable estimation of the unknown input. The quality of the estimated states is not assessed, since the states are corrected at each iteration using the available measurement(s). The metric utilised to evaluate the acceptance of the estimated unknown input is given by the root mean square error (RMSE) described in (3.7).

$$RMSE = \sqrt{\frac{\sum_{k=1}^{L} \left(\hat{d}_k - u_{d_k}\right)^2}{L}} \tag{3.7}$$

u_{d_k} and L being the measured unknown input by means of a validation sensor and the length of the experiment in number of samples respectively. The RMSE value is calculated for all the combinations of N_x and N_d, repeating the evaluation of each combination several times to obtain a mean value, since randomness is implicit in the dPF. As a result, the designer of the dPF chooses a combination of the lowest N_x and N_d values that yield acceptable estimations

according to his criterion. The criterion can be specified by the required computational time or the amount of hardware resources employed by the different amounts of particles.

3.1.3 Evaluation of the dPF in a simulated 2DoF system

This section presents the estimation results of the dPF in simulation, applied to a double mass-spring-damper (MSD) system with 2DoF depicted in figure 3.2, whose model is defined in (3.8).

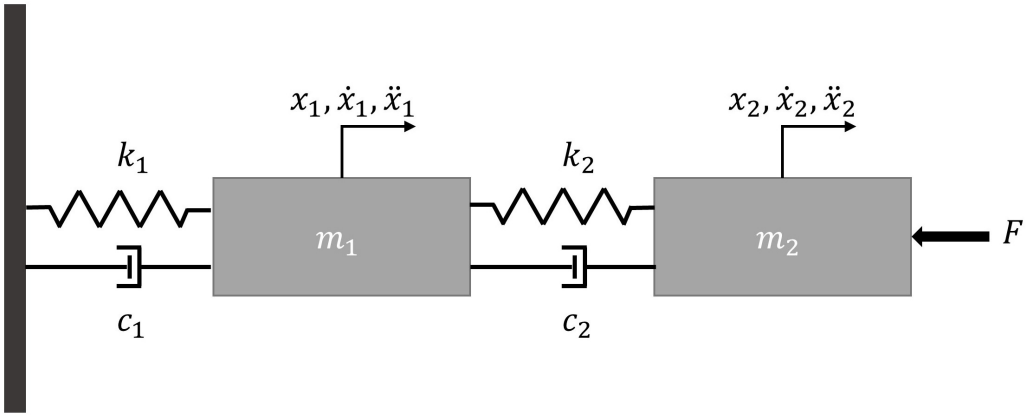

Figure 3.2: 2DoF mass-spring-damper system.

$$\begin{aligned} m_1\ddot{x}_1 + (c_1 + c_2)\,\dot{x}_1 + (k_1 + k_2)\,x_1 - c_2\dot{x}_2 - k_2x_2 = 0 \\ m_2\ddot{x}_2 + c_2\dot{x}_2 + k_2x_2 - c_2\dot{x}_1 - k_2x_1 = F \end{aligned} \tag{3.8}$$

The values of the parameters are defined in table 3.3.

	m_1	c_1	k_1	m_2	c_2	k_2
Values	$20kg$	$3kg/s$	$75N/m$	$10kg$	$1.5kg/s$	$37.5N/m$

Table 3.3: Values of parameters.

A sinusoidal force signal $F = 100\sin(2\pi t)$ N of $10s$ has been used as model input to simulate the dynamic response of the system, sampled in $f_s = 1kSps$. The sampling time is $t_s = 0.001s$. The acceleration $\ddot{x}_2$ of m_2 has been used as the only measured output of the system, taking the other two states of m_2, the three states of m_1 and the input F as unknown. The simulated states and the input have been distorted with a random Gaussian noise of 0 mean and 0.02 standard deviation $N(0, 0.02^2)$ to simulate measurement noise. Equation (3.9) represents the discrete state space model of (3.8).

$$\begin{bmatrix} x_{1_{k+1}} \\ v_{1_{k+1}} \\ a_{1_{k+1}} \\ x_{2_{k+1}} \\ v_{2_{k+1}} \\ a_{2_{k+1}} \end{bmatrix} = \begin{bmatrix} x_{1_k} + v_{1_k} t_s \\ v_{1_k} + a_{1_k} t_s \\ \frac{c_2}{m_1} v_{2_k} + \frac{k_2}{m_1} x_{2_k} - \frac{c_1+c_2}{m_1} v_{1_k} - \frac{k_1+k_2}{m_1} x_{1_k} \\ x_{2_k} + v_{2_k} t_s \\ v_{2_k} + a_{2_k} t_s \\ \frac{c_2}{m_2} v_{1_k} + \frac{k_2}{m_2} x_{1_k} - \frac{c_2}{m_2} v_{2_k} - \frac{k_2}{m_2} x_{2_k} + \frac{F_k}{m_2} \end{bmatrix} \tag{3.9}$$

Besides the dynamic equilibrium equation used by the PF-UI is defined as in (3.10). This equation must include F_k to evaluate the unknown input proposals.

$$m_2 a_{2_k} - c_2 v_{1_k} - k_2 x_{1_k} + c_2 v_{2_k} + k_2 x_{2_k} - F_k = 0 \tag{3.10}$$

The variance vectors for the proposal sampling $\boldsymbol{q}_x$ and $\boldsymbol{q}_d$ and weighting functions $\boldsymbol{\sigma}_x$ and $\boldsymbol{\sigma}_d$ have been defined iteratively, until the estimation result converges to the actual signals. Values are shown in (3.11).

$$\begin{aligned} \boldsymbol{q}_x &= \begin{bmatrix} 4t_s^4 & 4t_s^2 & 4 & 40t_s^4 & 40t_s^2 & 40 \end{bmatrix}^T & \boldsymbol{q}_d &= 50 \\ \boldsymbol{\sigma}_x &= 8 \times 10^{-3} & \boldsymbol{\sigma}_d &= 2 \times 10^{-4} \end{aligned} \tag{3.11}$$

$N_x = 1000$ and $N_d = 1000$ particles have been set based on the RMSE calculation methodology presented in the previous section, ensuring the estimations converge with the actual values of states and the unknown input with a tolerance of less than 5%. In this case, the selected criterion has been to guarantee lowest computational time possible for the established estimations tolerance.

The algorithm has been developed in Matlab® and sequentially executed in an PC equipped with an Intel® Core™ i7-4700MQ processor. Double precision floating point variables have been defined. The estimation process has taken 200.94 seconds, $0.0201s$ for each sample.

Results are shown in figure 3.3, where the estimated and the measured values of the three states of each mass are illustrated in the first two row of graphs. The estimated and the measured force of the system is also shown in the bottom graph.

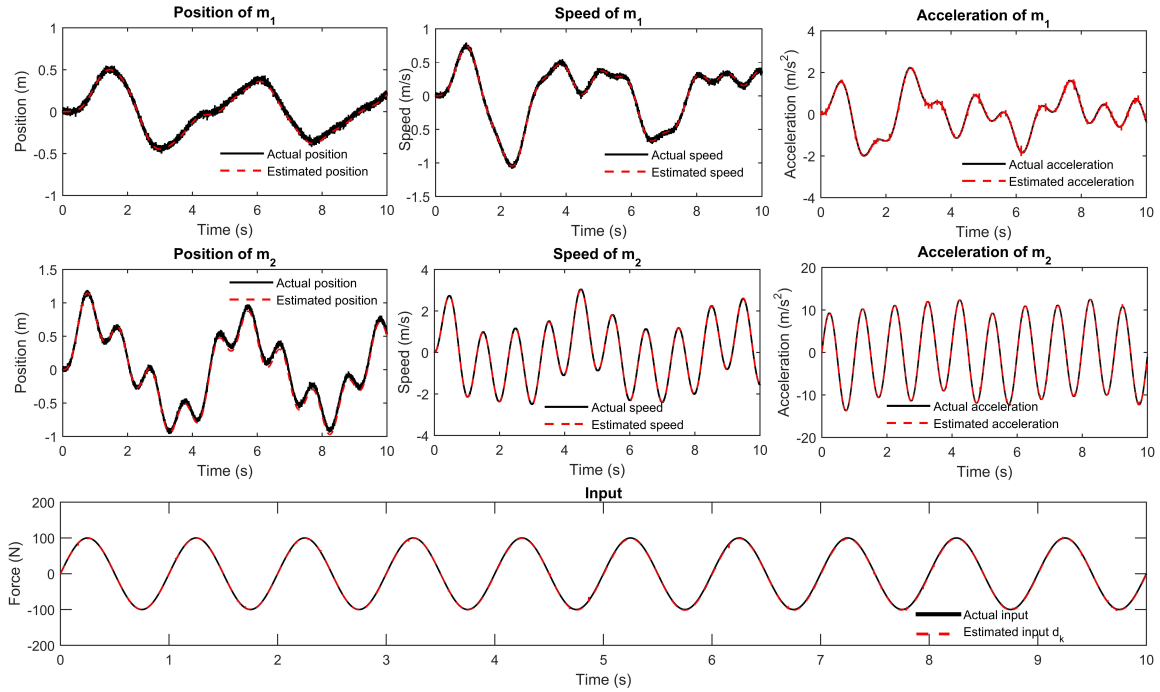

Figure 3.3: Estimation results of the 2DoF MSD model applying the dPF.

The RMSE values of the estimands are listed in table 3.4, which capture the deviation of the estimations from the measured (simulated with noise) signals. Obtained results show that estimated signals converge with actual signal values during the whole experiment. The RMSE evaluation shows also a good fitting since the obtained RMSE values are between two and three orders of magnitude smaller than the peak to peak value of their underlying estimands. The maximum RMSE value relative to the peak to peak value of its underlying estimand is obtained in the estimated unknown input d, being $\frac{6.475}{2*100}100 = 3.24\%$.

	x_1	$\dot{x}_1$	$\ddot{x}_1$	x_2	$\dot{x}_2$	$\ddot{x}_2$	F
RMSE	$0.027m$	$0.0214m/s$	$0.0322m/s^2$	$0.0562m$	$0.0265m/s$	$0.0479m/s^2$	$6.475N$

Table 3.4: RMSE of estimands.

3.2 Hardware implementation of the dPF

To achieve a real time execution of the dPF, a hybrid device comprising a multicore-CPU and an FPGA is proposed as discussed in the state of the art. A hardware architecture implementation is posed to accelerate the algorithm, exploiting dPFs parallelizable characteristics. The methodology followed to design and implement the required hardware architecture is inspired on the work presented by Mingas and Bouganis, 2012 and S. Liu et al., 2017. The hardware implementation is focused on the achievable computational time, while keeping a tolerable precision of the estimations. At the same time, these two specifications affect the utilisation of the

hardware resources.

Upon developing a hardware architecture, the precision of the estimations must be assessed by the designer of the algorithm, testing the parameters that affect the quality of the estimations, such as the number of initialised particles (N_x, N_d) and the arithmetic precision (number of bits representing the integer, sign and fractional portions of a number) of the variables used in the algorithm. Reduced arithmetic precision of variables results in larger arithmetic errors, loosing precision and affecting the estimation results, as claimed by Mingas and Bouganis, 2016. Indeed, both parameters affect directly the computational time of the algorithm. On the one hand, as N_x and N_d increase, the dPF has to evaluate more particles at the time step determined by the sampling time of the measurements. On the other hand, as arithmetic precision decreases, the area of hardware used by arithmetic operators also shrinks, leaving more hardware resources to implement parallelisation of the algorithm, as mentioned by Mingas and Bouganis, 2012 and Mingas and Bouganis, 2016.

Besides, to obtain a real time execution of the dPF, the throughput of the algorithm must match the throughput of the received data (measurements). Therefore, the dPF must generate an output from the received data in a shorter (or equal) period of time than the sampling time of the data acquisition system. The time period spent by the algorithm to produce an output is called latency.

Finally, the improvement of the estimation precision and the acceleration of the computational time have an impact on the amount of hardware resources required to build such hardware architectures. The available hardware resources is a constraint in many architecture designs.

3.2.1 Parameters that affect precision of estimations

The precision of the estimations is evaluated by means of the RMSE calculation (3.7) presented in section "Tuning of the dPF". These evaluation compares the actual value of the input with the unknown input estimated by the dPF. The estimated states are not evaluated, since states are corrected by means of the measurement, obtaining a better precision than in the case of the unknown input.

The RMSE calculation is used to evaluate the two parameters involved in the precision of estimations: the arithmetic precision of the variables used throughout the dPF and the number of initialised N_x and N_d.

Arithmetic precision

Regarding the arithmetic precision of the variables used throughput the algorithm, double, single or custom floating point arithmetic precisions can be defined. Double and single precision floating points have their fixed amount of bits assigned to represent the sign, the exponent and

fraction portions of a number. The custom precision floating point instead, is more flexible since it can take an arbitrary amount of bits for the exponent and fraction portions. Figure 3.4 shows the amount of bits assigned to the mentioned portions to define a variable depending on the arithmetic precision.

Looking at figure 3.4, it can be noted that a double precision floating point variable uses twice as many bits as a single precision variable. This implies that double precision variables require the twice as much memory resources and arithmetic operators as the single precision variables. Furthermore, these memory and arithmetic operator requirements can be reduced even more using custom precision variables that take fewer than the 32 bits of the single precision variables.

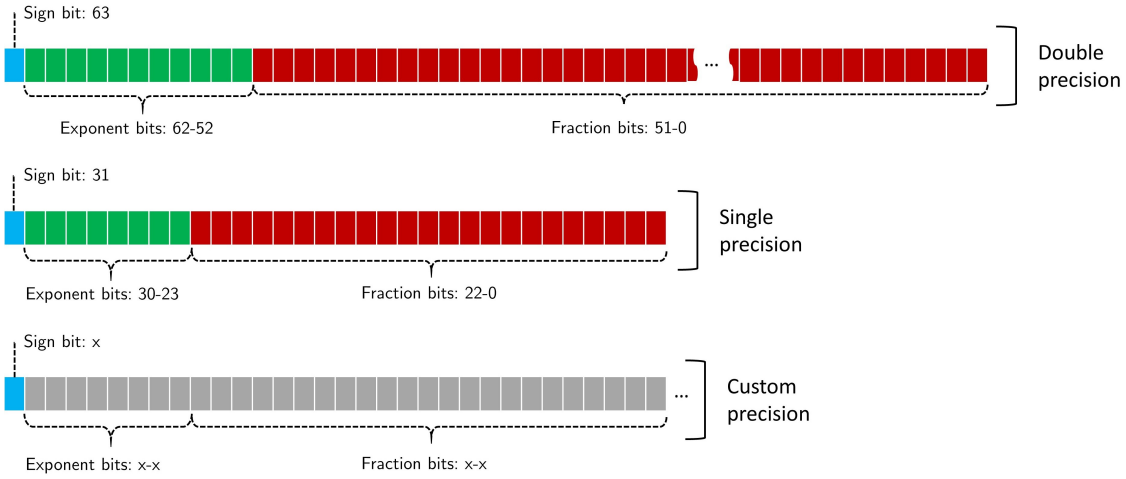

Figure 3.4: Assignation of bits for each arithmetic precision.

Nevertheless, if the variables' arithmetic precision is reduced in excess, it may turn out that variables do not define the quantities they represent accurately enough, which leads to a precision loss in the estimations. The RMSE calculation must be used to evaluate the precision of the estimations obtained under different arithmetic precisions.

Number of particles

The number of the initialised N_x and N_d must be large enough to guarantee the diversity in the sampled proposal particles. The lack of diversity is due to the small numbers of N_x and N_d, which produce an impoverishment of particles in the resampling step of the PFs, as discussed by Wang et al., 2017.

As it is well-known, during the resampling step, the particles with the smaller likelihood weights are replaced by copies of the particles with the largest likelihood weights. The diversity loss produced by these replacements becomes more evident when the number of N_x and N_d is small. Consequently, in next iterations, the proposals sampled from less diversified particles will be more similar from each other, worsening the likelihood of resembling to new values that are more distant in magnitude. As a result, the precision of the estimands will decrease, since the

PFs of the dPF are not able to track values that vary more than the sampled proposals.

This impoverishment discussed above can be easily tackled by increasing the number of N_x and N_d, since there will be more particles that are not replaced by the same copies, and the diversity will last more iterations, improving the precision of the estimations. Nonetheless, the larger the number of initialised particles the longer the algorithm takes to process the Prediction & Update and Resampling loops, and the more hardware resources are required to handle the amount of particles. The designer of the hardware architecture must assess the trade-off among precision of estimands, the achievable computational time and the utilisation of the hardware resources associated to the number of particles.

Similarly to the selection of the arithmetic precision, the RMSE of the estimated unknown input can be used to evaluate different combinations of N_x and N_d, seeking the minimum number of N_x and N_d that provide an arbitrarily acceptable result. The designer selects the values of N_x and N_d based on the plane formed by the number of particles and the RMSE shown in the example figure 3.5. To reduce the effect of the random sampling of dPF in estimations, each combination of particles should be evaluated several times, taking the mean RMSE value as a representative result.

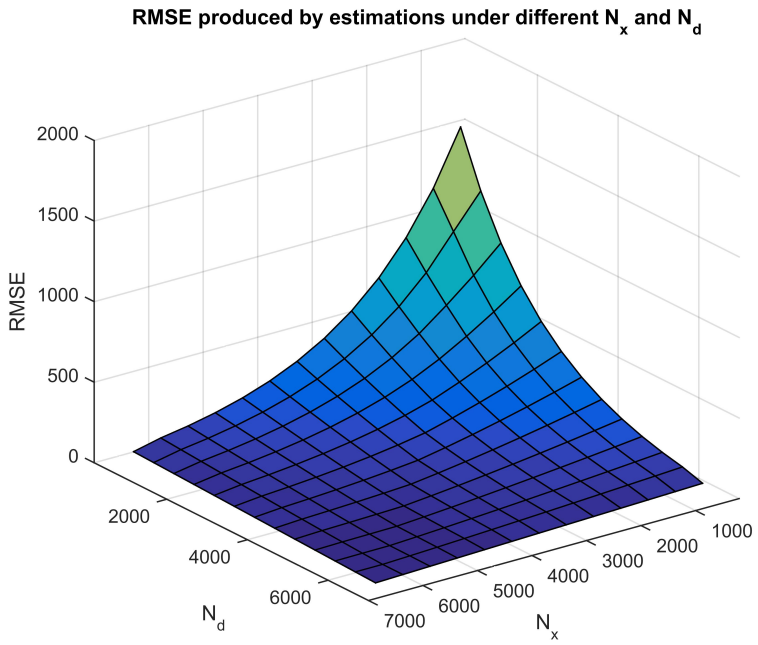

Figure 3.5: Example of the RMSE values produced by N_x and N_d.

3.2.2 Computational time

Under the selected N_x and N_d values and the arithmetic precision of variables, the dPF consumes a certain time processing the data sequentially. The algorithm processes the Prediction & Update and the Resampling loops of the PF-S and PF-UI, N_x and N_d times respectively, which makes the computational time increase as the number of initialised particles grows.

The computations related to each particle of N_x and N_d in the mentioned loops are independent, and therefore they can be processed in parallel in case that the algorithm is deployed in a parallelizable hardware. Within the developed hardware implementation methodology, the technique known as pipelining has been employed. Pipelining is a technique of executing subsequent instructions or commands overlapped in time. In a pipelined scheme, the received data is processed in a different hardware block at each clock cycle of the hardware. Thus, n instruction are executed at the same clock cycle for n data samples (i.e. particles). Illustration (a) and illustration (b) of figure 3.6 show a non-pipelined and a pipelined series of instructions respectively and emphasizes the number of clock cycles used in both processing schemes.

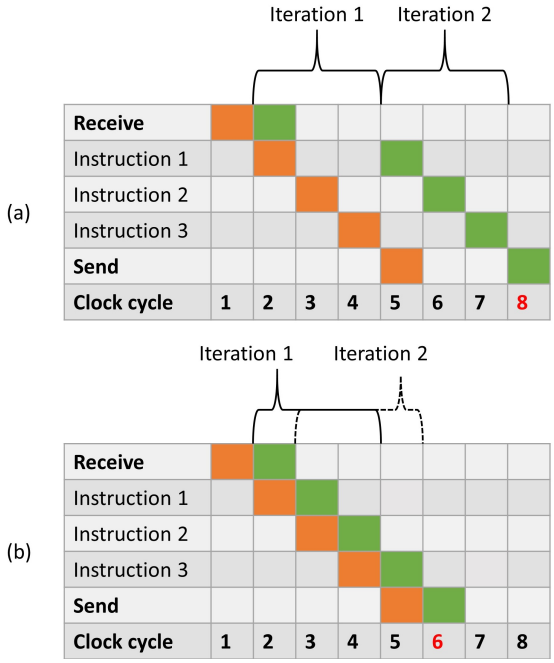

Figure 3.6: A non-pipelined and a pipelined series of instructions.

The time consumed by a pipelined loop is given by (3.12).

$$t_t = l_i + t_e \tag{3.12}$$

where t_t is the total execution time consumed processing the pipelined instructions, which is given by the initial latency l_i and the execution time of the instructions t_e.

An important parameter of loop pipelining that determines the initial latency l_i is the initiation interval (II). The II defines the number of clock cycles before a loop can accept new input data. Ideally the II is set as 1, which allows to output the data samples at every clock cycle. Nevertheless, sometimes due to limited hardware resources of the device, the II must inevitably be larger, causing higher latency. Taking into account each pipelined loop's t_t and the execution times of the rest of the sequential code, the dPF's total latency l_t is obtained. The total latency l_t represents how long the dPF takes producing an output from last received measurement.

To carry out a real time processing, the total latency l_t of the algorithm must be shorter than the sampling time of the data acquisition system. The resource consumption of the hardware implementation is tightly related to the time requirements established by the required latency. The faster (i.e. fewer clock cycles) the processing, the more resources are used. The designer of the architecture must try to optimise the design to satisfy the latency by using the minimum of the hardware resources on the FPGA.

3.2.3 Hardware resources

As noted in the previous sections 3.2.1 and 3.2.2, the actions taken to improve the precision of estimations and the computational time have an impact on the hardware resource utilisation.

The analysed resources are lookup tables (LUTs), flip flops (FFs), digital signal processing (DSP) modules and block-random access memories (BRAMs). The first three are computational resources, i.e. they are used to implement the computations of the algorithm. The BRAM instead, is a memory resource located on-chip. The amount of initialised particles, the arithmetic precision of variables and the II defined to implement the pipelined loops affect the mentioned hardware resources utilisation. The amount of resources used is evaluated after the designed hardware architecture is placed on the FPGA and the connections among the different hardware block are routed.

The designed hardware architecture to deploy the dPF in an hybrid device is shown in figure 3.7. The dPF algorithm is implemented exclusively in the programmable logic (PL or FPGA), but the estimated unknown input and states are shared through the processing system (PS or multicore-CPU), and those results are simultaneously extracted from the universal asynchronous receiver-transmitter (UART) for verification. The Gaussian and uniform random number generators (RNG) were also implemented in the FPGA.

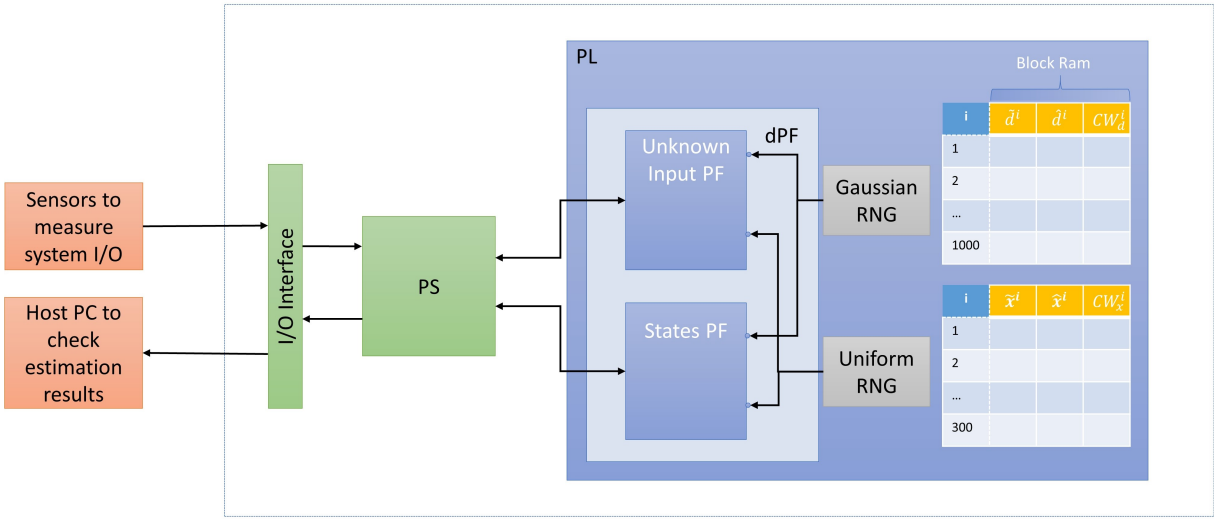

Figure 3.7: Global architecture of the dPF.

To predict the total latency of the implemented architecture and to guarantee the required latency, the code must be deterministic. For that reason, step (g) of the resampling loops presented in Algorithm I and Algorithm II must be modified, since its operation is a non-deterministic while loop. A bounded binary search resampling is raised to make step (g) deterministic, as shown in table 3.5.

Bounded binary search resampling	
	Initialise $L = 1$, $R = N_x$
	For $n = 1..13$
	Set: $p = floor\,(L + R/2)$
(g)	**if** $r_u > CW_x^p$ **then** $L = p$
	else if $r_u < CW_x^p$ **then** $R = p$
	else if $r_u == CW_x^p$ **then** $p = p - 1$
	End
	Copy the sampled p particle in the ith position of particles vector: $\hat{\boldsymbol{x}}_k^i = \tilde{\boldsymbol{x}}_k^p$

Table 3.5: Deterministic Resampling loop based on binary search.

The number of iterations of the **For** loop was set iteratively, checking that the binary search converged to a single particle number represented by p. The binary search shown in table 3.5 is also applied to the resampling of the unknown input particles.

3.2.4 Hardware implementation of the dPF on the 2DoF MSD system

The hardware implementation of the dPF is applied on the previously presented 2DoF MSD system to achieve a real time execution. First, a precision analysis is carried out, evaluating the estimation results obtained depending on the arithmetic precision and the initialised N_x and N_d particles. Then, as the total latency l_t of the algorithm is higher than the sampling time t_s of the measurement (the acceleration of m_2), the dPF is accelerated by means of the architecture presented in figure 3.7.

The hardware implementation is deployed in the hybrid Zynq UltraScale+ MPSoC ZCU106 Evaluation Kit of Xilinx, which integrates a quad-core ARM® Cortex™ applications processor and a PL (equivalent to an FPGA).

The precision analysis evaluates the arithmetic precision and the combinations of different N_x and N_d quantities based on the RMSE calculation presented in (3.7). The combinations of the different particle quantities are evaluated under single and double arithmetic precisions of dPF's variables. Each combination is run 50 times to reduce the effect of the random sampling of the dPF, taking the mean RMSE value from the 50 runs. Figure 3.8 shows two plots of the RMSE evaluation, obtained under single and double arithmetic precision for the analysed combinations of the particle numbers.

The three dimension graphs of figure 3.8 illustrate the influence of the arithmetic precision and the number of N_x and N_d on the RMSE. Based on the RMSE values, the double floating point arithmetic precision and $N_x = 1000$ and $N_d = 1000$ quantities are chosen assuming they produce estimations of acceptable precision. Using more particles does not improve the results significantly, while it takes more computational time to process the algorithm. Besides, the RMSE values obtained by means of the double arithmetic precision are one order of magnitude smaller than the ones obtained under single arithmetic precision.

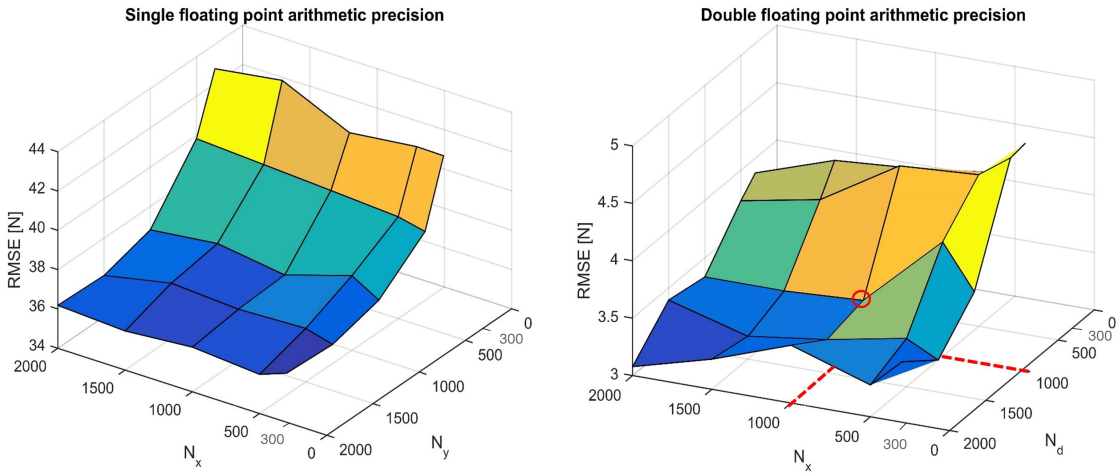

Figure 3.8: RMSE calculation for combinations of different N_x and N_d under single and double floating point arithmetic precisions.

The execution of the algorithm in a PC equipped with an Intel® Core™ i7-4700MQ processor takes $268s$ for a $10s$ experiment under the established precision parameters. Each received measurement is processed with a total latency of $l_t = 0.0268s$, while the sampling time is $t_s = 0.001s$. To achieve a real time execution of the dPF, the total latency must be lower than the sampling time $l_t < t_s$. For that purpose, a hardware implementation based acceleration is developed for the dPF.

The proposed architecture of the dPF shown in figure 3.7 is implemented by means of Vivado™ high-level synthesis (HLS) using the mentioned double floating point arithmetic precision and the number of particles $N_x = 1000$ and $N_d = 1000$. Initially, the targeted initiation interval is set as II= 1, to minimise the initial latency l_i. The hardware resource utilisation and the total latency obtained after the place and route step of the hardware implementation are shown in table 3.6. The achieved total latency is $l_t = 0.231ms$, which is 4.33 times lower than the sampling time $t_s = 0.001s$. Therefore the real time execution is guaranteed.

Piece of code	LUTs	FF	DSPs	BRAMs	II[1]	II[2]	Execution Time
PF-UI	19529	14213	61	4	4	7	$115.37\mu s$
PF-S	37468	26161	106	4	4	7	$115.30\mu s$
Total	56997	40374	167	8	-	-	$230.67\mu s = 0.231ms$

Available on board	230400	460800	1728	624	-	-	-
Percentage	24.74%	8.76%	9.66%	1.28%	-	-	-
Execution time in software							$0.0268s$
Required latency							$< 0.001s = 1ms$

Table 3.6: Post place & route resource utilisation and execution time.

[1] The II of the Prediction & Update loop.

[2] The II of the Resampling loop.

Chapter 4

Validation of the dPF in a test bench

This chapter tackles the design of a servo press test bench to validate both, the developed servo press model and the proposed dPF. First a test bench design and manufacturing methodology is presented, based on the similitude theory proposed by the Buckingham's π dimensional analysis. The second section of the chapter demonstrates the estimation results obtained applying the dPF MBSS to the servo press test bench.

4.1 Buckingham's π based test bench design

This section presents a design methodology to develop a test bench that is able to emulate the kinematic and dynamic behaviour of the servo press under review with a priori established geometric and dynamic constraints. The aim of the scaled test bench is to provide a servo press to test and validate the proposed dPF algorithm in a controlled environment. The designed test bench keeps a kinematic and dynamic similitude with the use case servo press, being able to emulate other servo press set-ups too.

On the first step of the methodology, the Buckingham's π theorem is applied to obtain scaling laws that allow to define a scaled test bench similar to an original system. On the second step, a constrained optimisation of the scaled estimands is carried out. This optimisation provides values of estimands that fit in the pre-established design requirements and constraints. On the third stage, the activities and manufacturing tolerances of the scaled estimands are obtained, which determine the final dynamic similitude of the test bench with the original servo press.

4.1.1 Methodology

The similitude based scaling arises from the basic theorem of dimensional analysis, also known as Buckingham's π theorem (Buckingham, 1914; Curtis et al., 1982). Buckingham's π theorem provides a methodology to formulate dimensionless scaling laws from system's estimands. The

obtained dimensionless scaling laws must yield the same results using the estimands of the original system and the scaled estimands of the test bench, to keep a kinematic and dynamic similitude between them.

Formulated scaling laws give the possibility of scaling the test bench in multiple ways. To delimit the dimension and the characteristics of the scaled test bench those scaling laws are assessed in an optimisation framework to obtain optimal values of estimands according to the predefined requirements and constraints.

During the manufacturing, the test bench's parameters may suffer some deviations from the optimal values obtained in the optimisation step, due to inaccuracies in the manufacturing process or the constraints of the manufacturing equipment. In this context, some manufacturing tolerances are proposed, based on the importance of the parameters in the performance of the test bench's dynamic behaviour.

Buckingham's π formulation

Let us assume a dimensional expression (4.1) that includes U estimands s of the analysed dynamic system.

$$z = f(s_u) \qquad u = 1, 2, .., U \tag{4.1}$$

Estimands are physical magnitudes that are formed by fundamental dimensions denoted as $M =$ mass, $L =$ length, $T =$ time. Some estimands have one fundamental dimension such as the mass $m(kg) = M$; others have more than one, such as the linear acceleration $a(m/s^2) = LT^{-2}$. Let us define Q as the number of fundamental dimensions among all the estimands s_u. Buckingham's π theorem determines that the U estimands can be arranged in $(U - Q)$ dimensionless equations known as π-groups.

The π-groups are constructed using as many repeating estimands j as Q, each one including at least one of the fundamental dimensions. The most frequently chosen repeating estimands are those that are a-priori known or easily measurable. Thus, a π-group is represented as in (4.2).

$$\pi_n = s_n(j_1)^{\alpha_1}(j_2)^{\alpha_2}...(j_q)^{\alpha_q} \quad n = 1, 2, ..(U - Q) \quad q = 1, 2, ..Q \tag{4.2}$$

where $\alpha_1, \alpha_2, \alpha_q$ are chosen to ensure each π_n-group is non-dimensional. These π-groups can be used to define scaling laws λ for each scaled estimand as expressed in (4.3).

$$\lambda_n = \frac{\pi_{n_t}}{\pi_{n_o}} \qquad \lambda_{s_u} = \frac{s_{u_t}}{s_{u_o}} \tag{4.3}$$

where subindexes t and o stand for the test bench and the original system respectively.

Optimisation of the scaled system's estimands

Unlike for an ideal scaling framework, where the system's estimands can be scaled faithfully according to the established requirements, sometimes the design of the scaled system is subjected to constraints, such as geometric or operational constraints. In this context, achieving the required scaling of the system may be tedious. To overcome this difficulty an optimisation approach is proposed, which provides optimal values for the test bench's estimands keeping the dynamic similitude with the original system. The optimisation must also satisfy some functional and geometric requirements and constraints.

The optimisation approach is posed as a minimisation of a cost function $f()$ defined from the design requirements under constraints. A design requirement can be any functional specification that must keep a dynamic and kinematic similitude with the original system, e.g. a proportional torque to rotate a scaled servomotor at the same constant speed as the original servomotor. The constraints are usually given by geometric specifications and functional limits $h()$ of the scaled system, such as length, width, mass, maximum and minimum speed, voltage, force, pressure and etcetera.

Some of the scaling laws obtained from the Buckingham's π formulation are used as design requirements, whilst others are used as constraints of the scaled system. Maximum and minimum values of the test bench's estimands are also used as constraints. The optimisation equation is expressed as in (4.4).

$$\begin{aligned} & \min_{\lambda_{s_u}} f(\lambda_{s_u}) \\ \text{s.t.} \quad & h(\lambda_{s_u}) = 0 \\ & min_{s_u} < s_u < max_{s_u} \end{aligned} \tag{4.4}$$

The optimised values of the system's estimands describe a scaled system that keeps the dynamic and kinematic similitude with the original system.

Definition of the manufacturing tolerances

The optimised scaled test bench keeps the same dynamic behaviour as the original system under the established design requirements and constraints. Nevertheless, the manufacturing

process may make parameters deviate from the optimised values. The deviation of the optimised parameters is mainly due to inaccuracies of the manufacturing machine and the characteristics of the workpiece's material. Thereby, it is important to discover the impact of each parameter on the dynamic behaviour of the system.

Some parameters have a greater impact on the dynamic behaviour than others and therefore their tolerance with respect to the optimised values is lower. On the contrary, the deviations of parameters that have less impact on the dynamic behaviour produce a minor change in the dynamic behaviour of the system. To evaluate the influence of system's parameters, Kittirungsi et al. and Borutzky eta al. proposed an activity based metric Kittirungsi, 2008; Borutzky, 2011. The activity measures the amount of energy a parameter of the system consumes and generates over a specified time window T and is defined as in (4.5).

$$A_x = \int_{t=0}^{T} |P_x(t)| dt \qquad x = 1, 2, ..., X \tag{4.5}$$

$|P_x(t)|$ is the absolute value of the parameter's power over the time window T and X is the number of parameters p of the system.

According to the activity analysis, the parameters with the smallest activities tolerate a larger deviation from the optimised values without significantly altering the dynamic behaviour of the test bench to be manufactured. The tolerance of the parameters' values is specified by the grade of similitude required by the designer and it is calculated based on the sensitivity Ω of the analysed parameter as in (4.6). A parameter's sensitivity measures the response of the system's dynamic behaviour to the deviation of the parameter.

$$\Omega_x = \frac{A_x(\Delta s_x)}{A_{tot}} \tag{4.6}$$

This methodology leads to a more flexible design and manufacturing procedure of a scaled test bench, keeping the dynamic and kinematic similitude with the original system.

4.1.2 Application of the methodology for the design and manufacturing of a reduced scale servo press test bench

This section tackles the design of a reduced scale servo press test bench based on the methodology presented in subsection 4.1.1. The reduced scale test bench includes most of the components of the original servo press that have already been listed and described in section 2.2. The gearbox of the original system is excluded from the analysis, since its reduction ratio will be defined by the required torque and speed of the scaled servo press. Likewise, the friction model's coefficients

are excluded from the scaling procedure, since they will depend on factors that cannot be scaled, such as lubrication, the finishing of the manufactured components or the assembly of the system.

The estimands to be scaled are included in the dimensional expression as shown in (4.7).

$$z = f(\tau_e, \theta, \dot{\theta}, \ddot{\theta}, r, \acute{r}, l, \acute{l}, I_1, m_1, I_2, m_2, m_3, F_{ms}, \xi, x) \tag{4.7}$$

where the symbols that have not been already defined in section 2.2 are ξ and x, representing the elastic coefficient and the linear deformation of the servo press's structure respectively. These two estimands are implicitly included in the process force, since they define the force that the servo press's structure is exerting against the formed workpiece ($F_{ms} = \xi x$). F_{ms} denotes the maximum process force value of the servo press, which will be the main design requirement. Equation (4.7) shows $U = 16$ scalable estimands, whose fundamental dimensions are listed in (4.8).

$$\begin{array}{llll} \tau_e = ML^2T^{-2} & \theta = none & \dot{\theta} = T^{-1} & \ddot{\theta} = T^{-2} \\ (r, \acute{r}, l, \acute{l}) = L & (I_1, I_2) = ML^2 & (m_1, m_2, m_3) = M & F_{ms} = MLT^{-2} \\ & \xi = MT{-}2 & x = L & \end{array} \tag{4.8}$$

The dimension analysis of the estimands in (4.8) show $Q = 3$ fundamental dimensions (M,L and T). Thus, $(U - Q) = 13$ non-dimensional π-groups can be formulated by means of Q repeating estimands selected by convenience. The selected repeating estimands are $j_1 = F_{ms}$, $j_2 = m_3$ and $j_3 = r$, since they can be easily measured in the original servo press. π-groups are shown in the set of equations (4.9). π_1-group calculation procedure is demonstrated in Appendix B.1.

$$\begin{array}{llll} \pi_1 = \dfrac{\tau_e}{F_{ms} r} & \pi_2 = \theta & \pi_3 = \dot{\theta}\sqrt{\dfrac{m_3 r}{F_{ms}}} & \pi_4 = \ddot{\theta}\dfrac{m_3 r}{F_{ms}} \\ (\pi_5, \pi_6, \pi_7) = \dfrac{(\acute{r}, l, \acute{l})}{r} & (\pi_8, \pi_9) = \dfrac{(I_1, I_2)}{m_3 r^2} & (\pi_{10}, \pi_{11}) = \dfrac{(m_1, m_2)}{m_3} & \pi_{12} = \xi\dfrac{r}{F} \\ \pi_{13} = \dfrac{x}{r} & & & \end{array} \tag{4.9}$$

The π-groups lead to the formulation of the scaling laws λ_n, which describe the ratio between the estimands of the original system and the scaled test bench. Scaling laws are grouped as in the set of equations (4.10).

$$\begin{aligned}
\pi_1 \rightarrow \frac{\tau_{e_o}}{F_{ms_o} r_o} = \frac{\tau_{e_t}}{F_{ms_t} r_t} \rightarrow \quad & \frac{F_{ms_t} r_t}{F_{ms_o} r_o} = \frac{\tau_{e_t}}{\tau_{e_o}} \rightarrow \lambda_{F_{ms}} \lambda_r = \lambda_{\tau_e} \\
\lambda_\theta = 1 \qquad \lambda_{\dot{\theta}} = \frac{\lambda_{F_{ms}}^{1/2}}{\lambda_{m_3}^{1/2} \lambda_r^{1/2}} \qquad & \lambda_{\ddot{\theta}} = \frac{\lambda_{F_{ms}}}{\lambda_{m_3} \lambda_r} \qquad \lambda_{\acute{r}} = \lambda_r \\
\lambda_l = \lambda_r \qquad \lambda_{\acute{l}} = \lambda_r \qquad & \lambda_{I_1} = \lambda_{m_3} \lambda_r^2 \qquad \lambda_{I_2} = \lambda_{m_3} \lambda_r^2 \\
\lambda_{m_1} = \lambda_{m_3} \qquad \lambda_{m_2} = \lambda_{m_3} \qquad & \lambda_\xi = \frac{\lambda_{F_{ms}}}{\lambda_r} \qquad \lambda_x = \lambda_r
\end{aligned} \tag{4.10}$$

The obtained scaling laws are used in the optimisation approach, which includes constraints and a cost function based on the design requirements. The cost function of the optimisation approach is defined by the maximum force ratio denoted as $\lambda_{F_{ms}}$, which is the ratio between the targeted maximum force of the scaled test bench and the maximum force of the original system. The cost function is expressed in (4.11).

$$\min_{\lambda_{F_{ms}}} = f \left(\lambda_{F_{ms}} - \lambda_{F_{ms_i}} \right)^2 \tag{4.11}$$

$$\lambda_{F_{ms_i}} = \lambda_\xi \lambda_r \tag{4.12}$$

At each i iteration, the optimiser proposes a value for the maximum force ratio $\lambda_{F_{ms_i}}$ to minimise the cost function. The proposition of $\lambda_{F_{ms_i}}$ is defined by the scaling law of (4.12). The rest of the scaling laws are introduced in the optimiser as non-linear equality constraints c_{eq_n}, as in (4.13).

$$\begin{aligned}
c_{eq_1} = \left(\frac{\lambda_{\tau_e}}{\lambda_{F_{ms}} \lambda_r} - 1 \right) \qquad & c_{eq_2} = \left(\frac{\lambda_{\dot{\theta}} \lambda_{m_3}^{1/2} \lambda_r^{1/2}}{\lambda_{F_{ms}}^{1/2}} - 1 \right) \qquad c_{eq_3} = \left(\frac{\lambda_{\ddot{\theta}} \lambda_{m_3} \lambda_r}{\lambda_{F_{ms}}} - 1 \right) \\
c_{eq_4} = \left(\frac{\lambda_{\acute{r}}}{\lambda_r} - 1 \right) \qquad & c_{eq_5} = \left(\frac{\lambda_l}{\lambda_r} - 1 \right) \qquad c_{eq_6} = \left(\frac{\lambda_{\acute{l}}}{\lambda_r} - 1 \right) \\
c_{eq_7} = \left(\frac{I_1}{\lambda_{m_3} \lambda_r^2} - 1 \right) \qquad & c_{eq_8} = \left(\frac{I_2}{\lambda_{m_3} \lambda_r^2} - 1 \right) \qquad c_{eq_9} = \left(\frac{\lambda_{m_1}}{\lambda_{m_3}} - 1 \right) \\
c_{eq_{10}} = \left(\frac{\lambda_{m_2}}{\lambda_{m_3}} - 1 \right) \qquad & c_{eq_{11}} = \left(\frac{\lambda_\xi \lambda_r}{\lambda_{F_{ms}}} - 1 \right) \qquad c_{eq_{12}} = \left(\frac{\lambda_x}{\lambda_r} - 1 \right)
\end{aligned} \tag{4.13}$$

As a result, scaled estimands of the test bench must yield the same π-group values as the original system, which guarantees that the kinematic and dynamic similitude are kept.

The design requirement and constraints are provided to the optimiser as inputs. In this case, the established design requirement is that the test bench must carry out at least a process force up to $F_{ms_t} = 1000kg$. Constraints are defined to limit the size of the test bench. The displacement of the ram cannot exceed $0.04m$ and cannot be smaller than $0.03m$, which is given by $[0.03m] < 2r <= [0.04m]$. The optimised values are shown in Table 4.1.

Magnitudes	**Original servo press's values**	**Optimised test bench's values**
τ_e	$9.081 \times 10^4 Nm$	$22.70Nm$
θ	$(-)rad$	$(-)rad$
$\dot{\theta}$	$(X)rad/s$	$2.19(X)rad/s$
$\ddot{\theta}$	$(X)rad/s^2$	$4.82(X)rad/s^2$
r	$0.2m$	$0.02m$
$\acute{r}$	$0.076m$	$0.00762m$
l	$1.05m$	$0.105m$
$\acute{l}$	$0.3270m$	$0.0327m$
I_1	$80.92kg/m^2$	$0.0045kg/m^2$
m_1	$424kg$	$2.35kg$
I_2	$132.72kg/m^2$	$0.0073kg/m^2$
m_2	$825.86kg$	$4.57kg$
m_3	$11600kg$	$64.21kg$
F_{ms}	$400000kg$	$1000kg$ (requirement)
ξ	$1.35 \times 10^9 N/m$	3.375×10^7
x	$0.0025m$	$0.00025m$

Table 4.1: Original and optimised estimands' values.

The values obtained solving the π-groups for both the original system and the test bench, reveal an identical kinematic and dynamic similitude of the test bench according to the Buckingham's π theorem. Results are shown in table 4.2.

π-groups	**Original servo press's values**	**Optimised test bench's values**
π_1	1.1351	1.1351
π_2	1	1
π_3	0.0762	0.0762
π_4	0.0058	0.0058
π_5	0.3811	0.3811
π_6	5.25	5.25
π_7	1.6351	1.6351
π_8	0.174	0.174
π_9	0.286	0.286
π_{10}	0.0366	0.0366
π_{11}	0.0712	0.0712
π_{12}	675	675
π_{13}	0.0125	0.0125

Table 4.2: π-group values for both, the original system and the test bench.

Owing to the value deviations that the optimised estimands may suffer during the manufacturing of the test bench, parameters' activities and sensitivities are calculated. In an unconstrained optimisation, the original system's parameters and the optimised ones must produce the same activity results. The test bench designer will define some tolerances for the parameters based on the sensitivity analysis to keep the desired similitude with the original system.

The parameters of the test bench are m_1, m_2, m_3, I_1, I_2 and ξ, which define the condition of the test bench's components. Analytical expressions of the parameters' power are shown in Appendix B.2. Parameters' activities are expressed in the set of equations (4.14).

$$\begin{aligned} A_{m_1} &= \int_{t=0}^{T} |P_{m_1}(t)|dt \qquad A_{m_2} = \int_{t=0}^{T} |P_{m_2}(t)|dt \qquad A_{m_3} = \int_{t=0}^{T} |P_{m_3}(t)|dt \\ A_{I_1} &= \int_{t=0}^{T} |P_{I_1}(t)|dt \qquad A_{I_2} = \int_{t=0}^{T} |P_{I_2}(t)|dt \qquad A_{\xi} = \int_{t=0}^{T} |P_{\xi}(t)|dt \end{aligned} \tag{4.14}$$

Optimised parameters' activities are calculated numerically using the analytical expression of parameters' power and the crankshaft's angular position θ as input for the calculation of power. Crankshaft's angular position is depicted in figure 4.1.

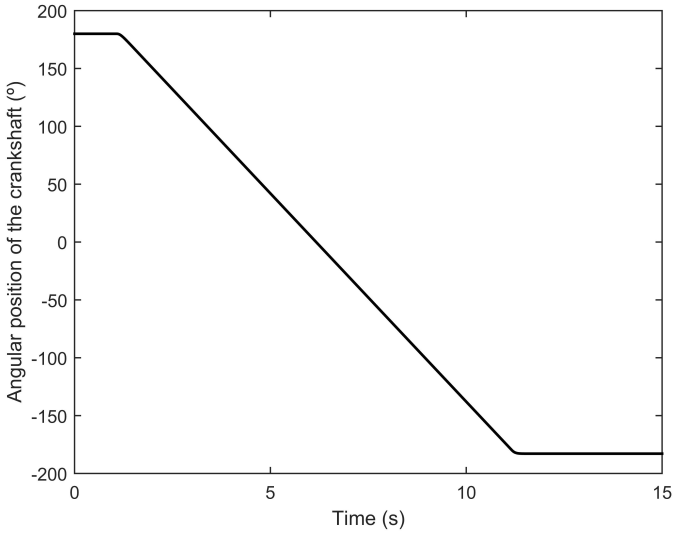

Figure 4.1: Crankshaft's angular position.

Activity values and their percentage of the total activity are shown in Table 4.3. Figure 4.2 shows the evolution of activities during the working cycle. The activity analysis reveals that a deviation in the ram's mass will have a greater impact on the kinematic and dynamic behaviour of the system than a deviation in the rest of the parameters, since its activity is the 88.6% of the total activity.

Parameters	**Activity**	**Activity percentage**
m_1	$0.7014J$	1.23%

m_2	$3.59J$	6.31%
m_3	$50.35J$	88.6%
I_1	$0.088J$	0.15%
I_2	$6.81 \times 10^{-4}J$	0.002%
ξ	$2.11J$	3.71%
Total	56.84×10^5	100%

Table 4.3: Parameters' activities.

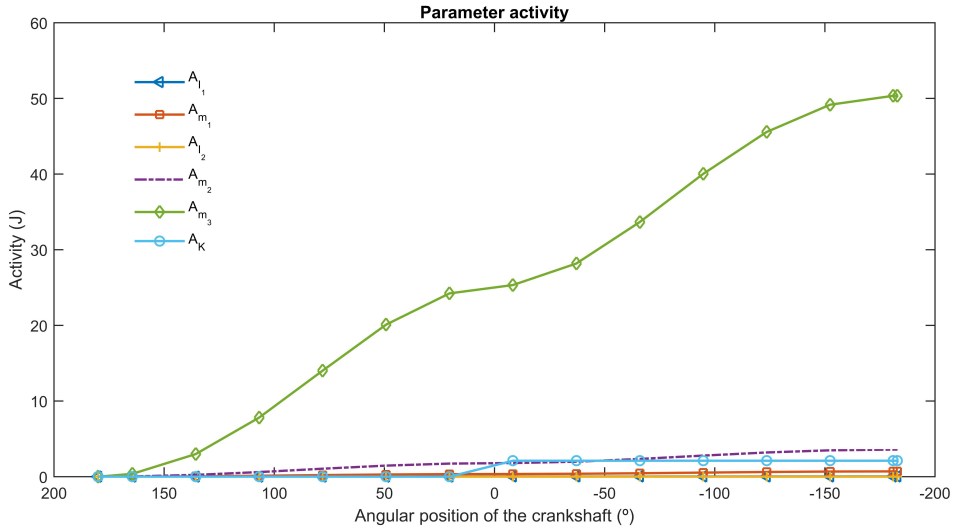

Figure 4.2: Activities of parameters during a single cycle of the servo press.

Regarding the manufacturing of the scaled test bench, a tolerance of a 2% in the parameters' activities is set arbitrarily, yielding the ranges of the parameters collected in table 4.4. It also shows the actual values obtained after the manufacturing. For parameters with small activity percentages (less than 3%), values equal or higher than the optimized values have been proposed. Otherwise, the manufacturing of the components associated to those parameters might be difficult or even impossible due to the specifications of the component. The percentages of the activities of m_2 and m_3 differ slightly from the targeted 2% of deviation.

Parameters	**Minimum value**	**Maximum value**	**Obtained after manufacturing**	
			Actual value	**Activity %**
m_1	$2.35kg$	$7.16kg$	$6.058kg$	3.09%
m_2	$3.24kg$	$8.58kg$	$7.24kg$	8.76%
m_3	$42.23kg$	$73.2kg$	$60.12kg$	85.33%
I_1	$0.0045kg/m^2$	$0.1523kg/m^2$	$0.0101kg/m^2$	0.154%
I_2	$0.0073kg/m^2$	$2.4kg/m^2$	$0.0410kg/m^2$	0.006%
ξ	$2.66 \times 10^7 N/m$	$4.76 \times 10^7 N/m$	$3.06 \times 10^7 N/m$	2.66%

Table 4.4: Parameters' manufacturing ranges.

According to table 4.4, the obtained parameters' values after the manufacturing process are between the established minimum and maximum values. The percentages of the activities of m_2 and m_3 differ slightly from the targeted 2% of deviation.

The manufactured test bench is shown in figure 4.3.

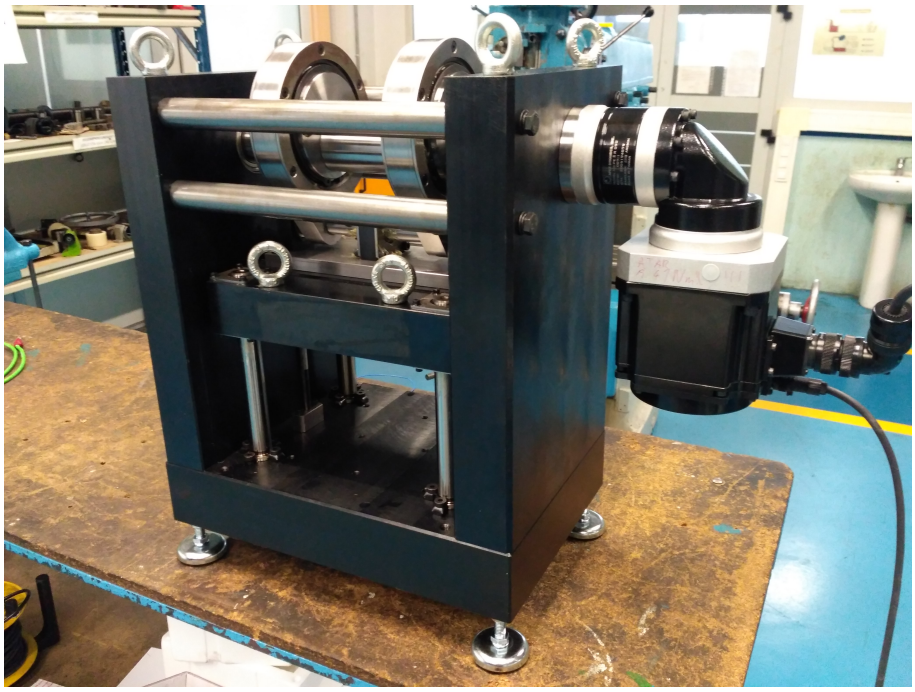

Figure 4.3: Manufactured test bench.

Test bench's dynamic and kinematic behaviour has been compared with the original system's one. To monitor the dynamic behaviour of the original servo press, two different force level strokes have been performed against two cylinders of rigid steel placed under each connecting rod, as shown in image A of figure 4.4. The two force levels have been achieved placing two rigid steel foils of different thickness on the rigid cylinders. The thicker the foil, the greater force is achieved. The process force has been measured by means of two PE sensors, each one installed in their respective connecting rod, measuring the force signal at 1kSps. Those two experiments have been replicated in the scaled test bench, exerting a stroke against a rigid cylinder equipped with a load cell, as illustrated in image B of figure 4.4. The maximum forces of the two experiments carried out in the original servo press have been $\lambda_{F_{ms}}$ proportionally replicated in the test bench, placing different thickness foils as well. Measurements have also been carried out at 1kPps in the test bench.

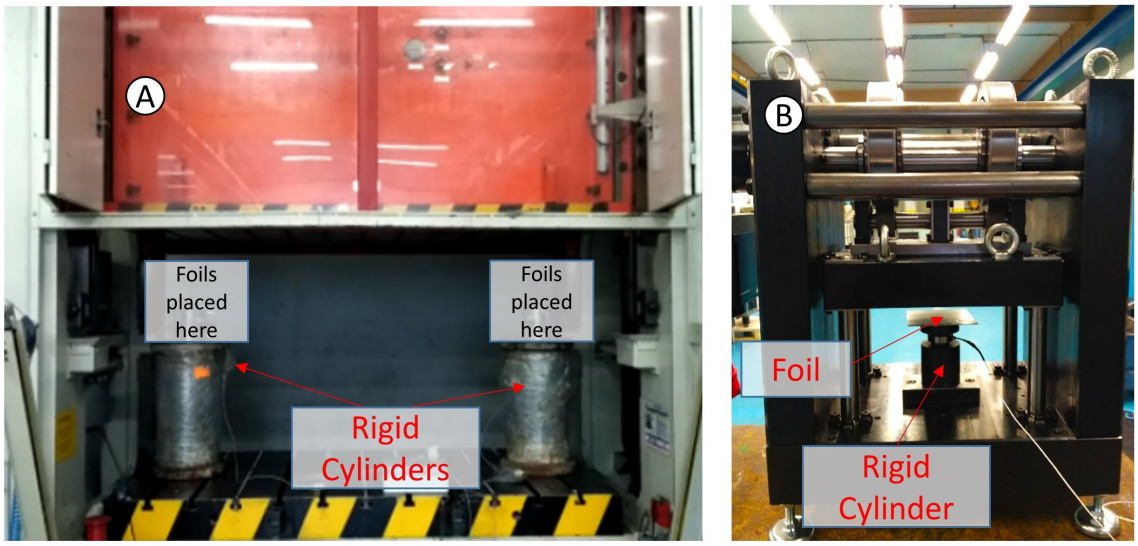

Figure 4.4: Experimental set-up of the original servo press and the test bench.

Figure 4.5 shows the two force profiles measured in both servo presses. The proportional force of the scaled test bench and the force of the original servo press in image A and image B, draw a similar force curve for the same angular position of the crankshaft, with an RMSE value of 8.57t and 19.13t respectively. Comparing these RMSE values with the maximum force applied in both experiments, 182t in the experiments of image A and 351t in the experiments of image B, the obtained relative errors are 4.71% and 5.45% in image A and B respectively, which yield a mean value of 5.08% for the relative error. Therefore, the obtained relative error demonstrates the dynamic and kinematic similitude of the test bench with the use case servo press.

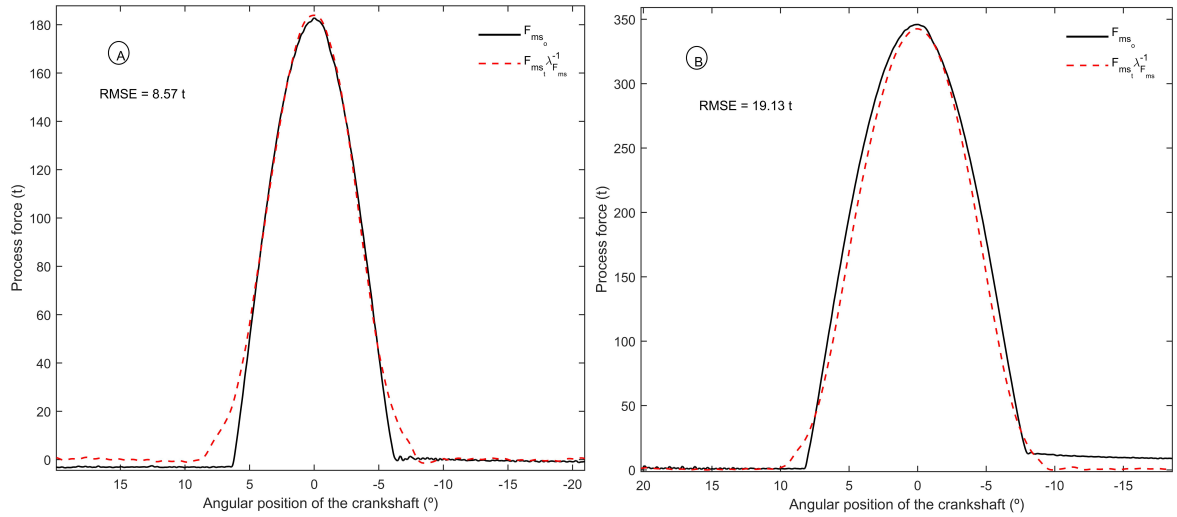

Figure 4.5: Force profile of both machines drawn throughout the angular position of the crankshaft.

The next section tackles the validation of the proposed dPF algorithm in the scaled test bench of the servo press.

4.2 Validation of the dPF

To validate the dPF in the scaled test bench, two different experiments have been carried out. In each experiment, the force has been exerted by means of a stroke against a cylinder equipped with a load cell. The height of the cylinder has been modified in each experiment placing rigid steel foils and the process force has been measured by a load cell for validation.

The servo press model (2.19) has been modified according to he parameters obtained through the Buckingham's π based scaling. The three phase currents and angular position signals of the servomotor have been measured using a sampling frequency of $F_s = 1kSps$. These signals have been filtered using a low pass filter with a cutting frequency of $fc = 100$Hz to remove higher frequencies, since they are not representative of the servo press's slower dynamics of interest. The RMSE of the three states and the process force has been calculated to evaluate the fitting of the estimations. Regarding the states, the RMSE has been calculated for the whole cycle of the press, whereas the RMSE of the process force has been calculated only for the angular position region where the servo press is exerting the force. This way, the fitting error of the process force is highlighted. The friction model is characterised by means of the method presented in section 2.2.1, obtaining the parameters shown in 4.15.

$$\begin{aligned} f_c &= 1.83Nm & f_s &= 0.511Nm \\ f_v &= 1.51Ns/m & v_s &= 12.5rad/s \end{aligned} \tag{4.15}$$

Figure 4.6 and figure 4.7 illustrate the estimation results of the system's states (angular position, angular speed and angular acceleration of the crankshaft) and the process force for experiment 1 and experiment 2 respectively. The setup of graphs in both figures, 4.6 and 4.7 is the next: the upper left corner shows a graph of the angular position of the crankshaft versus time; the upper right corner shows a graph of the angular speed of the crankshaft versus the angular position of the crankshaft; the lower left corner shows a graph of the angular acceleration of the crankshaft versus the angular position of the crankshaft; the lower right corner shows a graph of the process force versus the angular position of the crankshaft. The corresponding RMSE values of the estimations are shown in each graph. Looking at the acceleration graphs of both experiments an upward and a downward peaks are depicted at the beginning ($-180°$) and at the end ($180°$) of the signal respectively. These acceleration peaks represent the start and the stop of the rotation of the crankshaft. The central oscillation seen in both, the acceleration graph and the speed graph of both experiments is due to the beginning and end of the stroke.

It should be noted that the RMSE of the force obtained in the experiment 2 is smaller than one obtained in experiment 1, and therefore the estimation of force in figure 4.7 is better. This is due to the higher signal to noise ratio (SNR) in the electric torque of experiment 2 compared to experiment 1. As the force level decreases, the required torque to generate that force also decreases, reducing the SNR. The lower the SNR, the more difficult is to distinguish the signal from the noise.

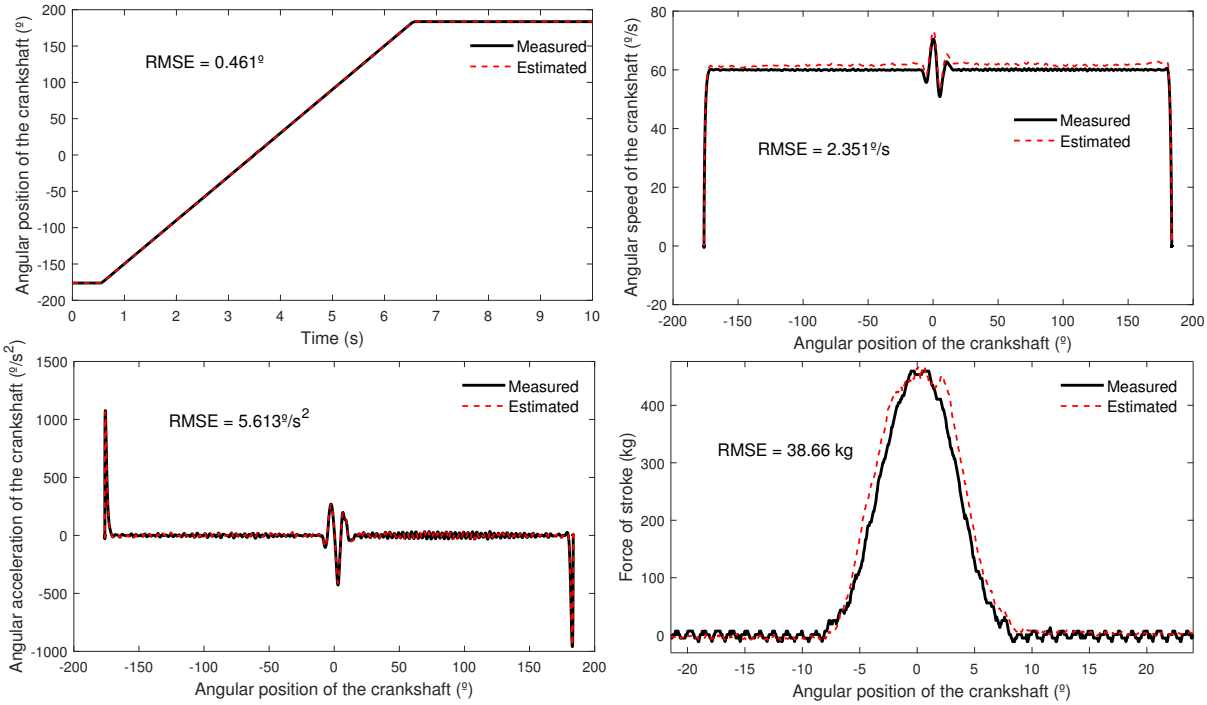

Figure 4.6: Estimation results of states and the process force in experiment 1.

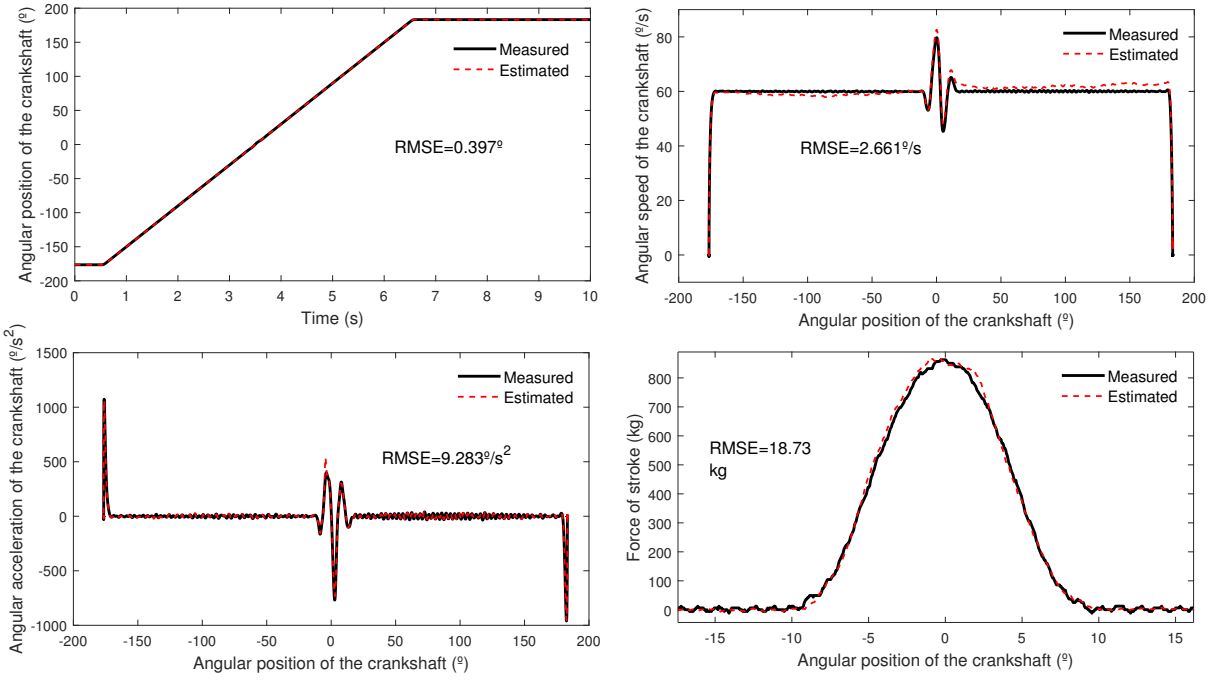

Figure 4.7: Estimation results of states and the process force in experiment 2.

Figure 4.8 illustrates the deviations of the estimated forces of figure 4.6 and figure 4.7 with respect to the measured forces. The deviation of the estimated force is evaluated by means of the instantaneous normalised absolute deviation calculated through as the difference between the estimation and the measurement, using a normalisation factor of 1000kg, which is the maximum force of the test bench. The force deviation in experiment 2 is lower than in experiment 1 during the whole force profile due to is higher SNR.

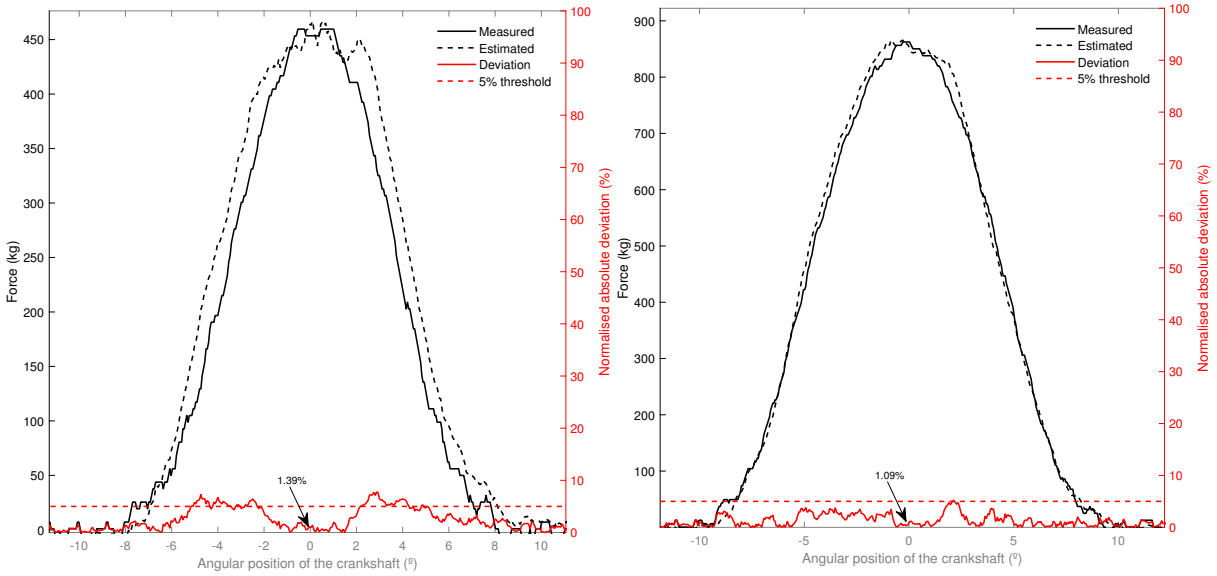

Figure 4.8: Instantaneous normalised absolute deviation of the estimated process forces with respect to the measurements.

The next chapter is focused on two sections, the validation of the dPF and the proposed model in an industrial servo press under different processes and the hardware implementation of the dPF to accelerate the execution time.

Chapter 5

Industrial implementation of the monitoring solution

This chapter tackles the experimental validation of the dPF in an industrial servo press to estimate the process force and its states and the hardware implementation of the dPF for the servo press model. Three different processes have been monitored by means of the dPF: a stroke against two rigid steel cylinders, a deep drawing process and a semi-solid forging process. The second section of the chapter addresses the hardware implementation of the dPF.

5.1 Validation of the dPF in an industrial servo press

In this section the proposed dPF is tested in three different processes carried out in an industrial servo press. The three processes provide different machine conditions and force profiles to assess the dPF.

The profile of the force exerted by a single stroke against two rigid steel cylinders, draws a parabolic shape during its application, as shown in figure 5.1. This process guarantees a continuous increase and decrease in force, depending on whether the ram approaches or moves away from the BDC respectively. In this process, due to the high stiffness of the cylinders, they do not deform and the structure of the press is which suffers the deformation when the force is applied (highlighted in blue in figure 5.1).

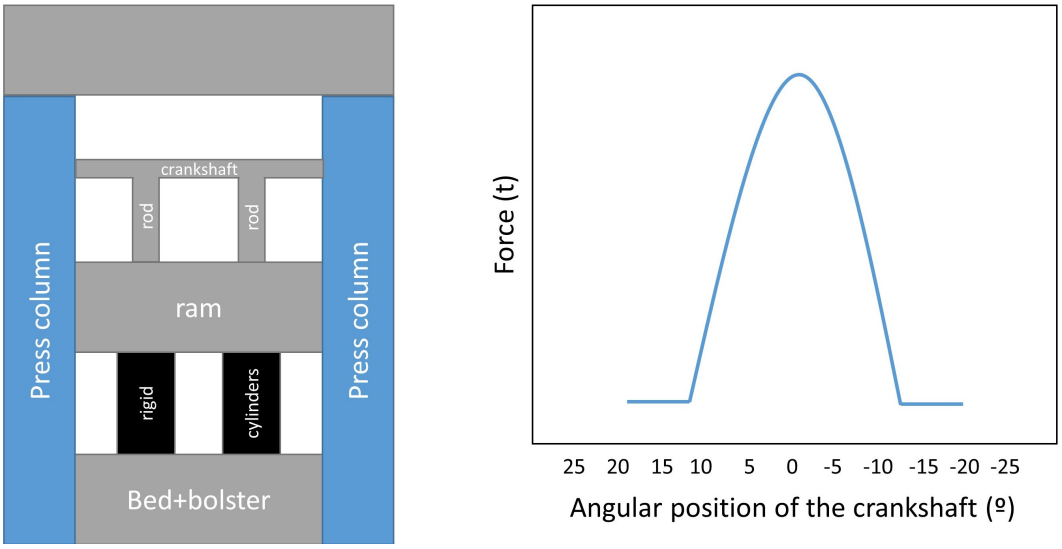

Figure 5.1: Force profile produced by a single stroke against two rigid steel cylinders.

The second process type that was carried out to evaluate the dPF was the deep drawing process. Deep drawing is a metal forming process where compressive and tensile forces are applied to transform a sheet metal blank (highlighted in blue in figure 5.2) into a hollow cup as illustrated in figure 5.2 (Schuler, 1998). The force profile depends on the geometry of the dies. Compared to the stroke against two rigid steel cylinders, the deep drawing process is characterised by prolonged force profiles that begin in an earlier and end in a later angular position of the crankshaft.

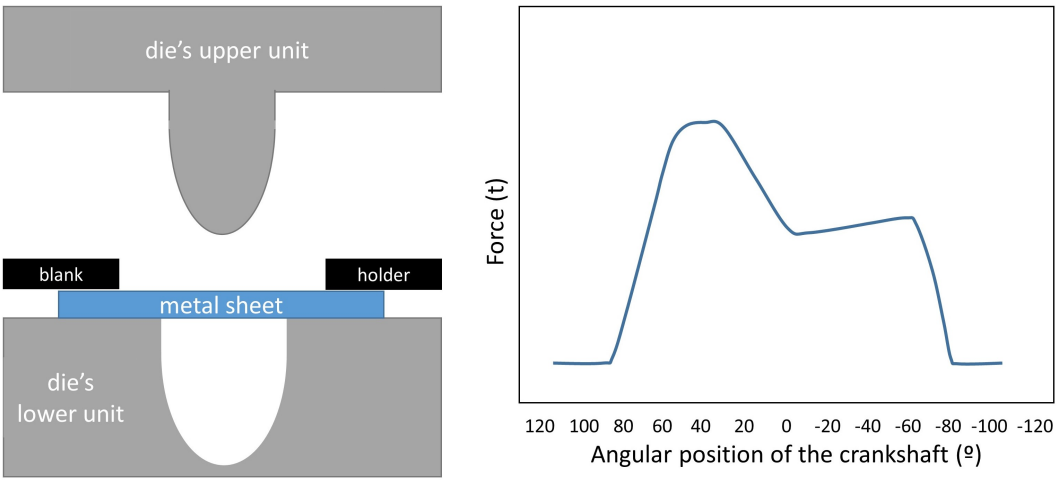

Figure 5.2: Conceptual illustration of a deep drawing process and a characteristic force profile.

The last process type where the dPF was evaluated was the semi-solid forging, where a part is formed in a closed die, as illustrated in figure 5.3. The semi-solid state is achieved by heating the workpiece during a determined period of time under specific temperatures. This technique allows to save raw material and energy consumed forming a part, compared to other conventional forging processes where the workpiece is not led to a semi-solid state, as stated by Lozares et al., 2019. In this process, a raw workpiece that is in a semi-solid state is introduced into the

die. Then the workpiece is shaped due to the applied force and the geometry of the die. The characteristic force profile of the SSF is shown in figure 5.3. The force increases until reaching the maximum value at the BDC, and then the ram is stopped at that position during a determined period of time, before the ram starts to move away from the BDC.

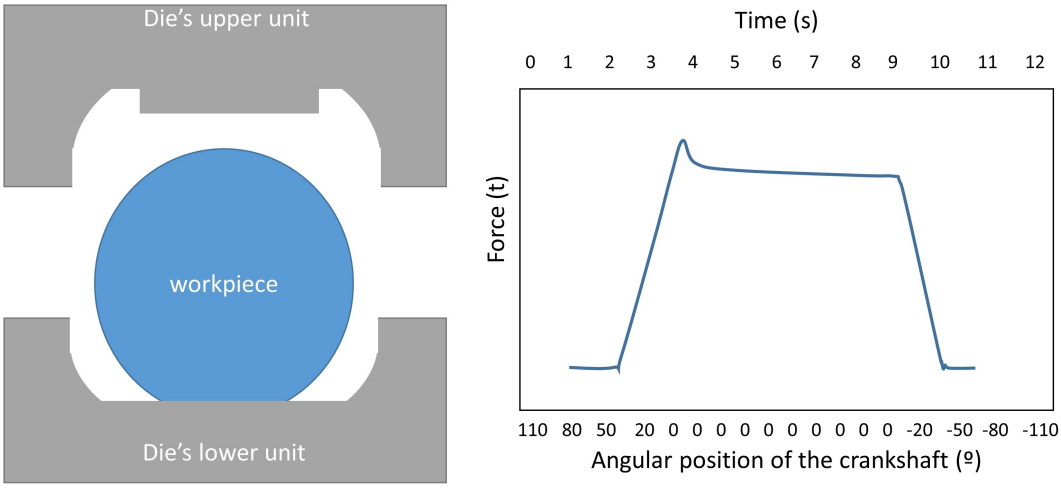

Figure 5.3: Conceptual illustration of a SSF process and its characteristic force profile.

The three types of processes have been carried out in Fagor Arrasate's model SDM2-400-2400-1200 industrial servo press. The signals used to feed the dPF are the three phase currents and angular position of the servomotor, obtained from the CNC of the servo press, using a sampling frequency of $1kSps$. No additional sensors have been integrated in the machine except the force sensors for validation. The force estimations carried out by the dPF, have been compared with actual force signals measured by means of two Brankamp®'s Vario piezoelectric sensors located on each connecting rod of the servo press. Additionally, the estimations of servo press states (the angular position, angular speed and angular acceleration of the crankshaft) have also been evaluated, comparing them with the signals obtained from the measured angular position of the servomotor.

As noted in section 2.2.1, the actual (measured) angular position of the crankshaft has been obtained multiplying the reduction ratio of the gearbox by the angular position of the PMSM's rotor $\theta = \theta_r \eta$. The angular speed and acceleration of the crankshaft are obtained deriving the angular position with respect to time: $\dot{\theta} = \frac{d\theta}{dt}$ and $\ddot{\theta} = \frac{d^2\theta}{dt^2}$. The derivatives have been calculated numerically by means of the differences between adjacent samples of the signal to be derived, multiplied by the sampling frequency of the data acquisition system.

Regarding the tuning of the dPF algorithm, the variance vectors used in proposal sampling and in the weighting function are given in (5.1). The number of initialised states particles and unknown input particles are $N_x = 300$ and $N_d = 1000$ respectively, based on the evaluation presented in section 5.2.

The deviation of the estimated force is evaluated by means of the instantaneous normalised absolute deviation calculated through as the difference between the estimation and the measurement,

using a normalisation factor of 400 t, which is the maximum force of the servo press. The results obtained at the BDC (0° of the angular position of the crankshaft) are also shown. The BDC is critical to the safety of a press because the maximum force is exerted at that position in most metal forming processes, which depending on the load may damage the machine.

5.1.1 Process: Strokes against rigid steel cylinders

The analysed process is a single stroke against two rigid cylinders depicted in figure 5.4. Five different experiments have been carried out, reaching a different maximum force level in each of them. Each force level has been applied modifying the heigh of the cylinders, adding rigid steel foils. The higher the cylinder, the greater force level is obtained.

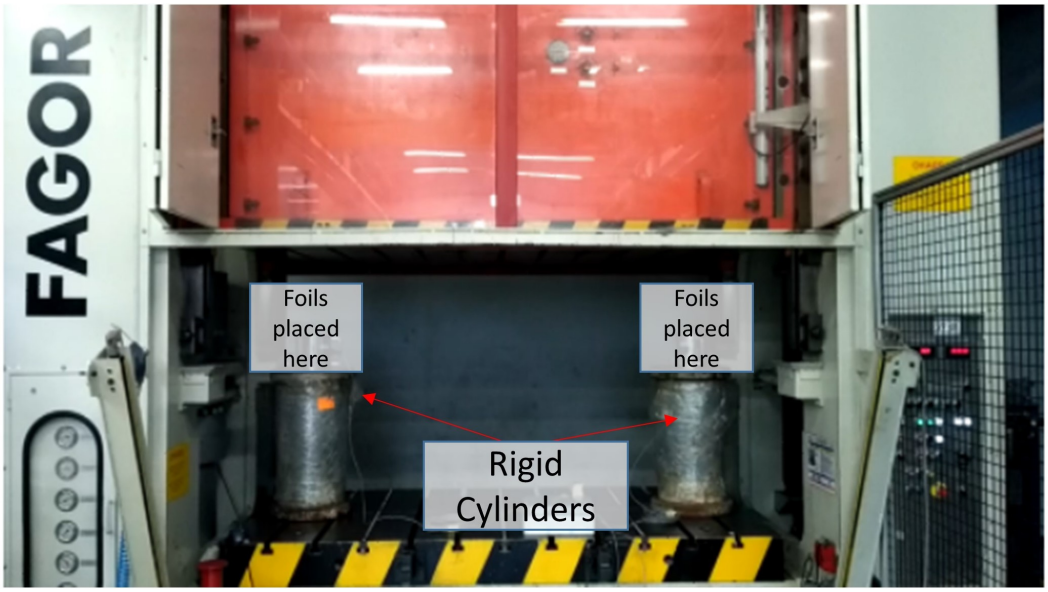

Figure 5.4: Experimental set-up of the stroke against post process.

Table 5.1 shows the maximum force, the initial height of the ram, the angular position at which the maximum force has been exerted and the angular speed of the experiments presented in this subsection.

Label	Maximum force measured	Adjustment of ram (height)	Maximum force position	Angular speed during force profile	Thickness of foils
STR1	186.24t	848.0mm	0°	$36°/s$	$0.7mm$
STR2	88.65t	848.0mm	0°	$36°/s$	$0.3mm$
STR3	184.27t	848.0mm	0°	$36°/s$	$0.7mm$
STR4	232.19t	848.0mm	0°	$36°/s$	$1mm$
STR5	343.11t	848.0mm	0°	$36°/s$	$1.4mm$

Table 5.1: Table of stroke against cylinder experiments.

Figure 5.5 shows the estimation results of experiment labelled as STR1, illustrating the measured

and estimated signals of the state variables of the servo press model and the force of stroke. The graphs of figure 5.5 are placed in the next way: the upper left corner shows a graph of the angular position of the crankshaft versus time; the upper right corner shows a graph of the angular speed of the crankshaft versus the angular position of the crankshaft; the lower left corner shows a graph of the angular acceleration of the crankshaft versus the angular position of the crankshaft; the lower right corner shows a graph of the process force versus the angular position of the crankshaft. The RMSE values that capture the fitting of the estimations are shown in the corresponding graph of each estimand. Looking at the acceleration graph a downward and an upward peaks are depicted at the beginning (180°) and at the end (−180°) of the signal respectively. These acceleration peaks represent the start and the stop of the forming cycle and are generated due to the beginning and the stop of the movement of the kinematic chain of the servo press. The central oscillation seen in the acceleration graph is produced by the stroke. Regarding the RMSE value of the force deviation, it is not shown throughout all the servo press cycle, but only for the angular positions where the force is exerted. Otherwise, the obtained RMSE value would be considerably smaller.

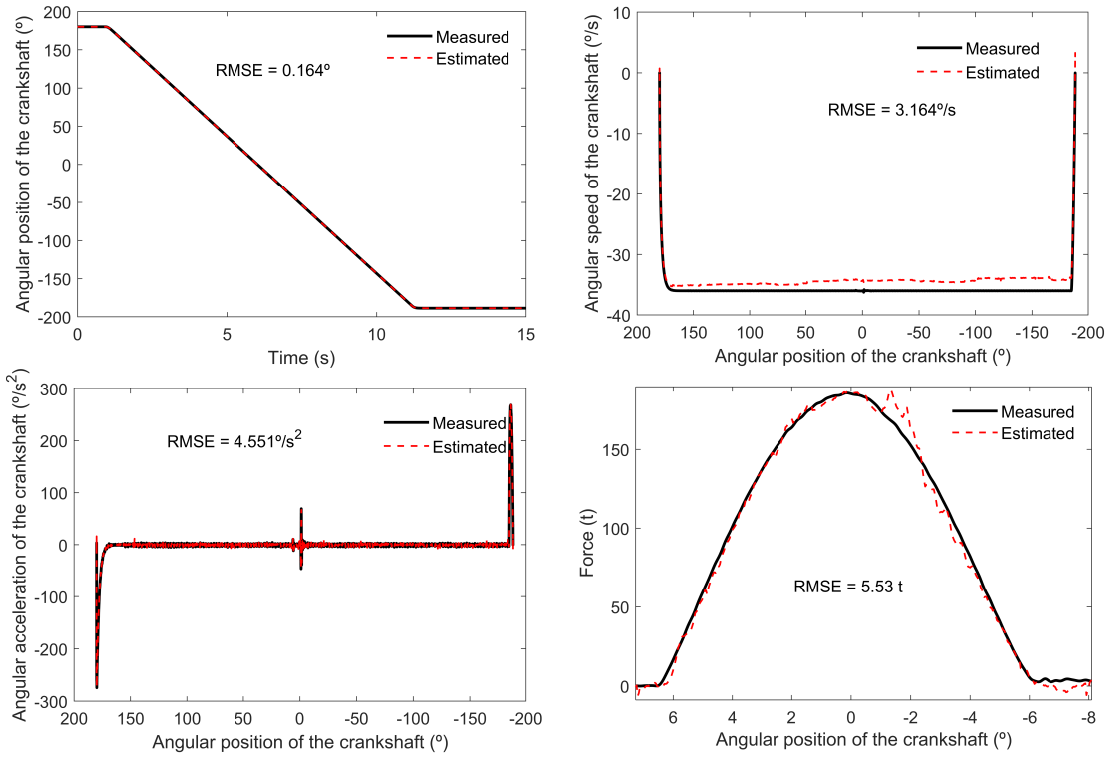

Figure 5.5: Estimation results of process force and states of experiment STR1.

The deviation in the estimated states variables is corrected at each iteration through the measured angular position of the crankshaft, so the next figure will be focused only on the process force, as it is the most relevant magnitude of the metal forming process. Figure 5.6 shows the estimation results of experiments STR2, STR3, STR4 and STR5, illustrating the measured and the estimated forces. The RMSE value of each estimation deviation is shown in the correspond-

ing graph.

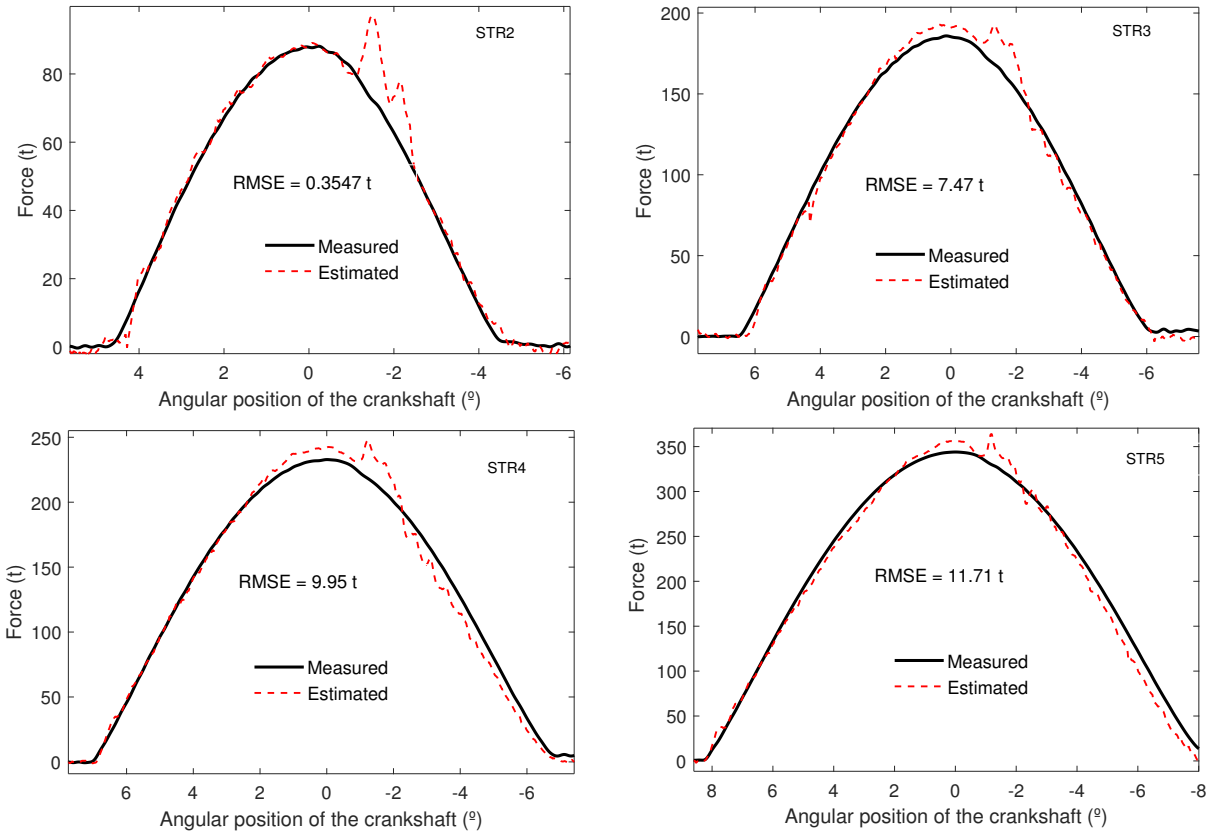

Figure 5.6: Estimation results of process forces of STR2, STR3, STR4 and STR5.

Figure 5.7 shows the instantaneous normalised absolute deviation of the forces illustrated in figure 5.6 from the beginning to the end of the stroke. The normalised absolute deviations of the four experiments remain under 5% throughout most of the time of the stroke. The deviations of the four experiments at the BDC are also highlighted in the corresponding graph, obtaining a maximum deviation of 2.97% in experiment STR5. Looking at either figure 5.6 or figure 5.7, one may note some peaks in the estimated force around $-1°$ and $-2°$ of the angular position of the crankshaft. These peaks are also found in the electric torque signal of the servomotor, as highlighted by the red ellipse of figure 5.8, which corresponds to the electric torque of experiment STR5.

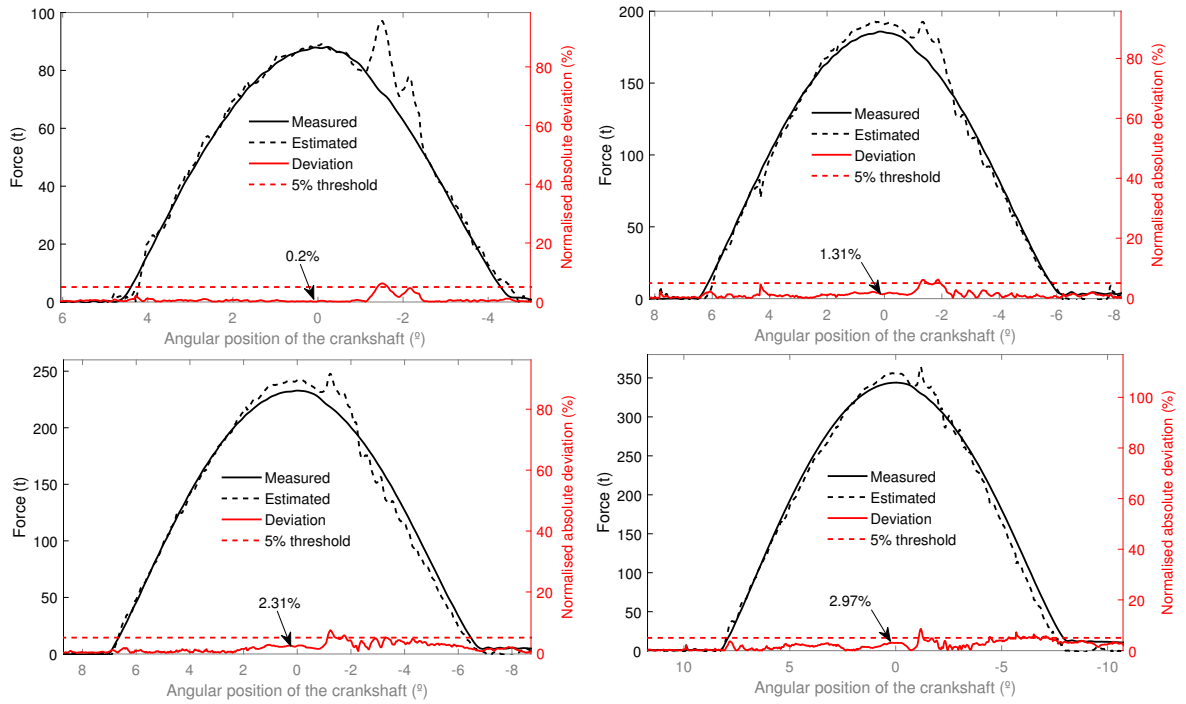

Figure 5.7: Instantaneous normalised absolute deviations of the process forces of STR2, STR3, STR4 and STR5.

These torque peaks are generated by the CNC of the servomotor in response to the energy that the structure of the press releases when recovering from its elastic deformation. The structure of the press suffers a elastic deformation when the force is applied. Therefore, when the ram moves away (upwards) from the BDC, the structure starts recovering the elastic deformation, producing those peaks as the controller tries to keep the commanded speed.

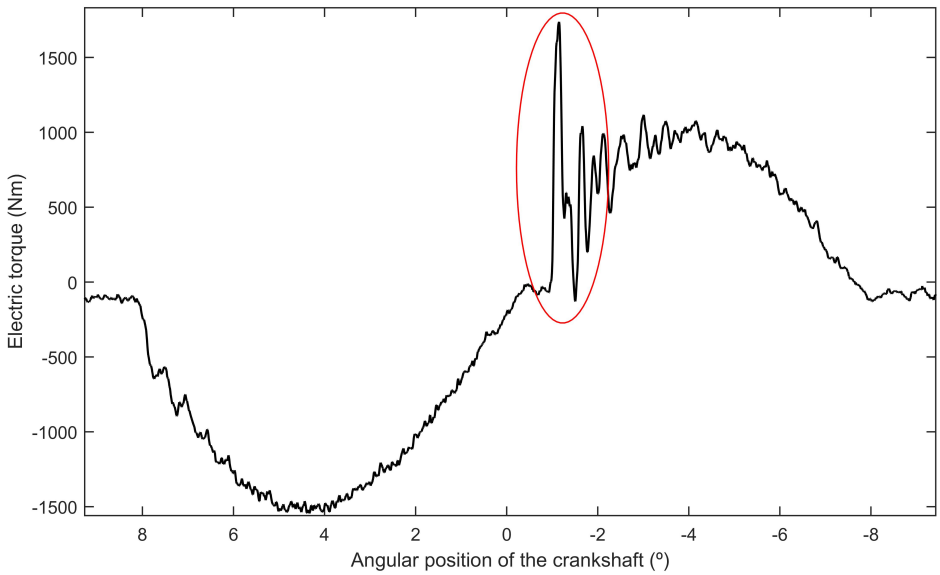

Figure 5.8: The electric torque of the servomotor, drawing peaks around 0○ angular position.

5.1.2 Process: Deep drawing

Three different deep drawing experiments were carried out using three different dies to evaluate the dPF. Each die generates a different force profile due to its geometric characteristics. Table 5.2 shows the maximum force, the initial height of the ram, the angular position at which the maximum force has been exerted and the angular speed of the experiments presented in this subsection. [Note: Due to confidentiality issues, the dies used in the mentioned deep drawing processes are not illustrated.]. Die 1 used in experiment DD1 performed a combined operation of drawing and multi-bending over a sheet metal. Die 2 used in experiment DD2 was designed to perform a deep drawing process. Die 3 of experiment DD3 was designed to form a cup-shaped part.

Label	**Maximum force measured**	**Adjustment of ram (height)**	**Maximum force position**	**Angular speed during force profile**	**Sheet material**
DD1	79.52t	850.2mm	14.59°	$120°/s$	DP1000
DD2	184.40t	850.2mm	0°	$120°/s$	DP1000
DD3	49.66t	800.0mm	49.51°	$36°/s$	DP1000

Table 5.2: Table of deep drawing experiments.

Figure 5.9 shows the estimations results for experiment DD1. The graphs of figure 5.9 are placed in the next order: the upper left graph shows the angular position of the crankshaft versus time; the upper right graph shows the angular speed of the crankshaft versus the angular position of the crankshaft; the lower left graph shows the angular acceleration of the crankshaft versus the angular position of the crankshaft; the lower right graph shows the process force versus the angular position of the crankshaft. The RMSE values of the deviation of estimations are shown in the corresponding graphs. The acceleration graph illustrates a negative (from 180° to 150° of the angular position) and a positive (from$-150°$ to $-180°$ of the angular position) acceleration steps that are respectively caused by the start and stop of the forming cycle. The three oscillating signal sections are due to the forming process. Regarding the process force, divergences around the $\theta = 0°$ angular position of the crankshaft show that the PMSM generates some torque peaks commanded by the CNC as shown in figure 5.8, to compensate the energy released by the structure of the servo press, as in the previous metal forming process.

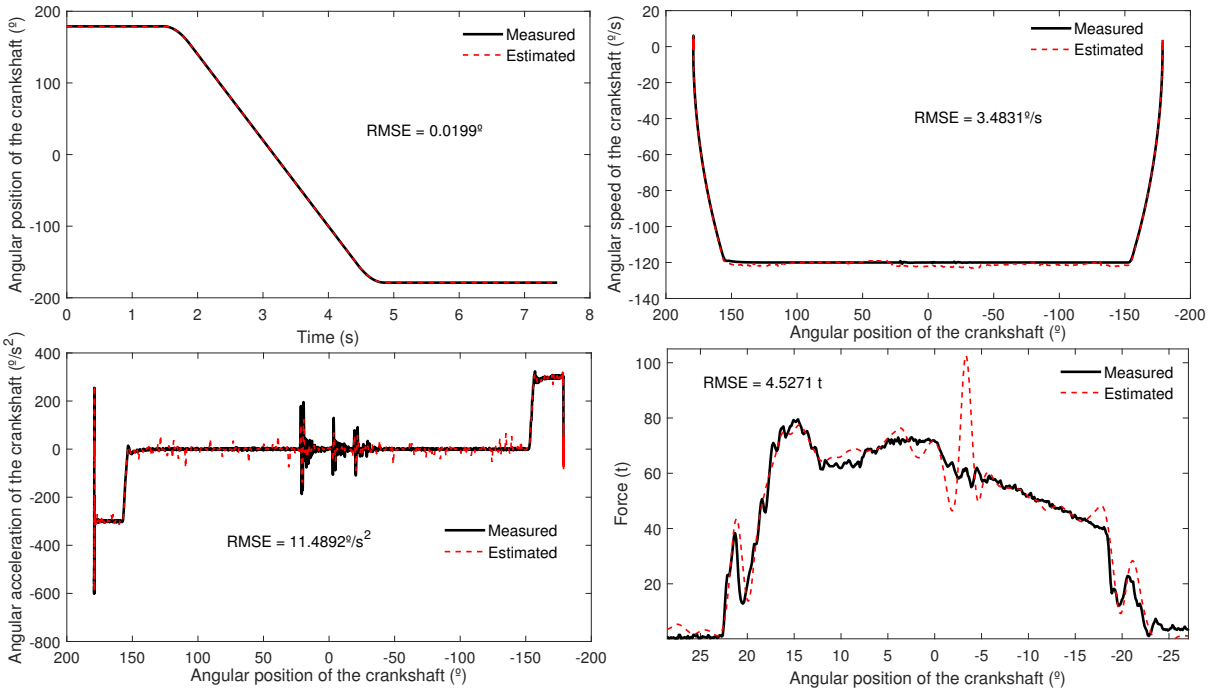

Figure 5.9: Estimation results of the process force and states of experiment DD1.

Figure 5.10 shows the estimations results for experiment DD2. The layout of the graphs of this figure is the same as in experiment DD1. The RMSE values of the estimation deviations are shown in the corresponding graphs. The acceleration graph shows a similar evolution of the acceleration as in experiment DD1. In this case, the PMSM also generates a torque peak to compensate the energy released by the structure of the servo press once the crankshaft passes 0° angular position.

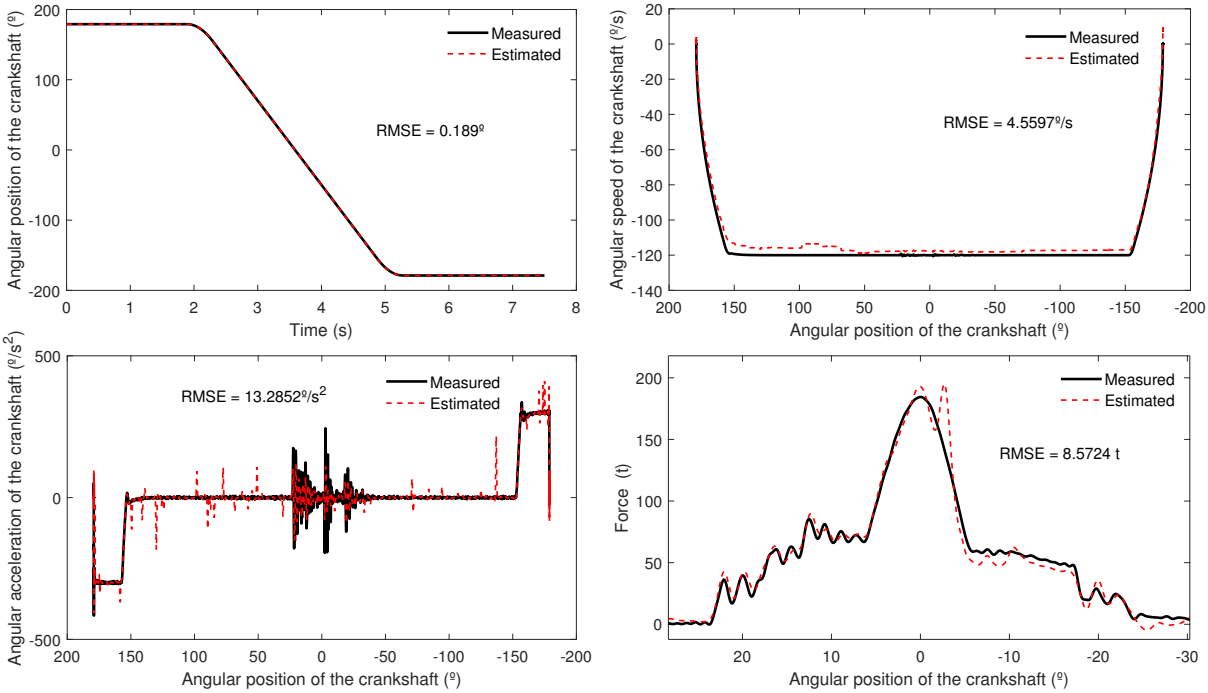

Figure 5.10: Estimation results of the process force and states of experiment DD2.

Figure 5.11 shows the estimation results for experiment DD3. The layout of the graphs of this figure is the same as in experiments DD1 and DD2. The RMSE values of the estimation deviations are shown in the corresponding graphs. In regards of the acceleration graph, the negative peak at 90° of the angular position and the positive peak at −90° of the angular position are caused by the start and the stop of the forming cycle. Oscillations around 50° of the angular position and −50° of the angular position are due to the beginning and the end of the forming operation. In this experiment, as the applied process force is smaller than in the experiments DD1 and DD2, the servo press's structure deforms less, so the torque produced by the PMSM to compensate the energy release of the servo press's structure is undetectable. The measured force profile finishes 8° earlier than the estimated force profile. In this case, the force estimation carried out by the dPF seems to be better than the measured one, since the acceleration graph also shows an oscillation at the same angular position as the estimated process force, pointing out the end of the forming operation.

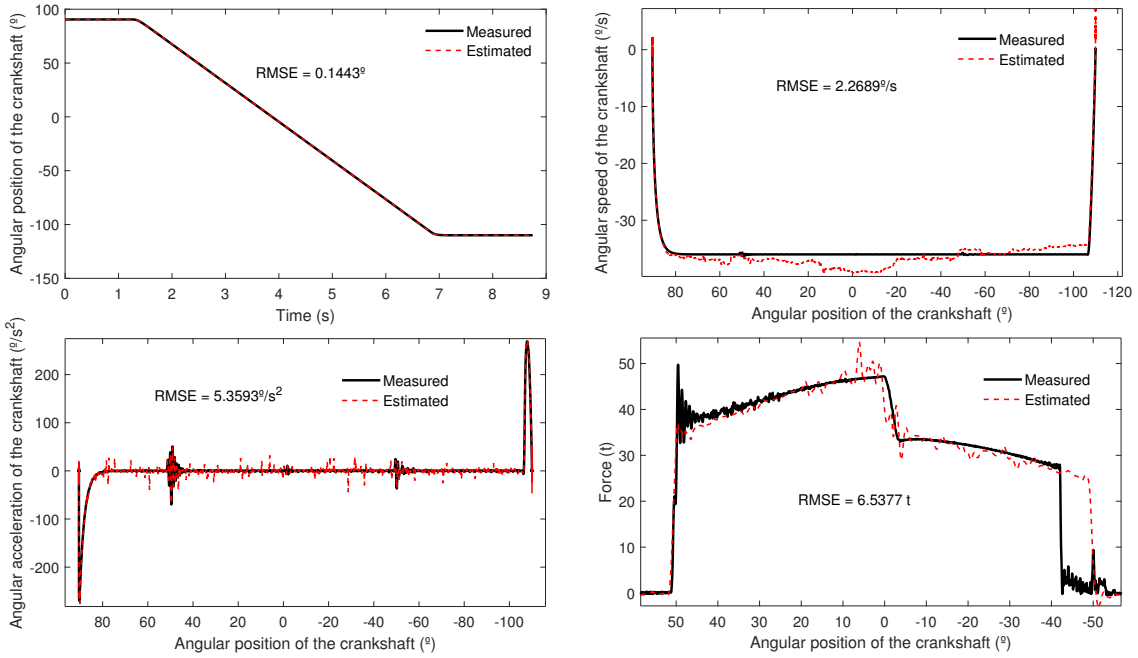

Figure 5.11: Estimation results of the process force and states of experiment DD3.

The deviations for the estimated process forces in the three experiments are shown in 5.12. The instantaneous normalised absolute deviations of the three experiments show variations along the force profile. The deviation for the maximum force point of the force profile is shown in the corresponding graph for each experiment. In the case of experiments DD1 and DD2, several peaks are found throughout the normalised absolute deviation which correspond to the torque peaks exerted by the PMSM in response to the energy release of the servo press's structure when recovering from its elastic deformation. In experiment DD3, the mentioned early drop of force in the measured signal shows a deviation that is over the 5% deviation threshold drawn in the graph.

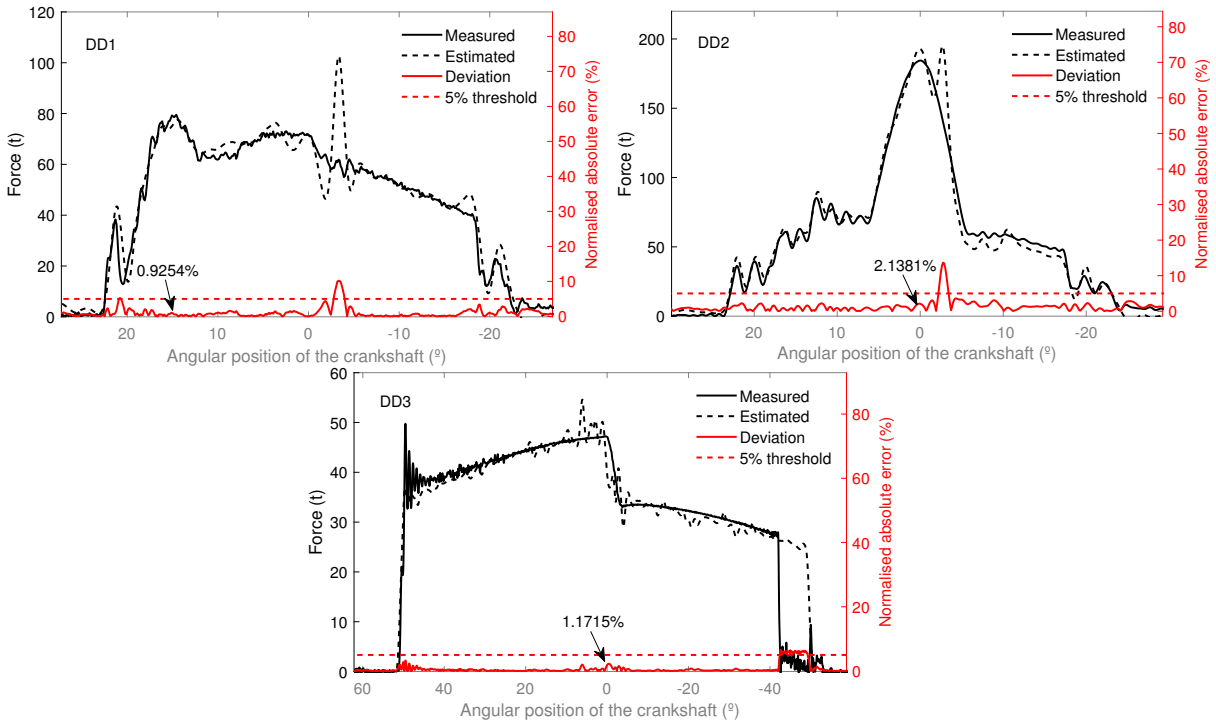

Figure 5.12: Instantaneous normalised absolute deviations of the estimated process forces of experiments DD1, DD2 and DD3.

5.1.3 Process: Semi-solid forging

Two different SSF experiments were carried out using two different dies to assess the dPF. Each die generates a different force profile due to its geometric characteristics. Table 5.3 shows the maximum force, the initial height of the ram, the angular position at which the maximum force has been exerted and the angular speed of the experiments presented in this subsection. Figure 5.13 shows the die and the part produced through the SSF process monitored in figure 5.14.

Figure 5.13: The die used in the monitored SSF process, along with the produced part.

Label	Maximum force measured	Adjustment of ram (height)	Maximum force position	Angular speed during force profile	Workpiece material
SSF1	417.72t	960.0mm	19.12°	$90°/s$	42CrMo4
SSF2	297.60t	960.0mm	3°	$0°/s$	S48C

Table 5.3: Table of semi solid forging experiments.

Figure 5.14 shows the estimation results of experiment SSF1. The layout of the graphs of this figure is the same as in experiments DD3. The RMSE values of the estimation deviations are shown in the corresponding graphs. In regards of the speed graph, a variable speed profile is depicted during the experiment. The acceleration graph shows a varying acceleration throughout the experiment. An initial downwards acceleration peak is found at 180° of the angular position of the crankshaft. The beginning of the forming operation is also identified in the acceleration signals around 53° of the angular position of the crankshaft. Acceleration is then abruptly reversed around 20° of the angular position. Regarding the force graph, the process force is continuously increasing until 20° of the angular position, where it drops abruptly. During this process, the critical force of the servo press was reached (400t), so the overload mechanism actuated stopping the process around the 20° of the angular position of the crankshaft. When the overload mechanism is activated, it stops the servomotor and pulls the ram upwards reducing the process force immediately. On the other side, from 18° onward, the estimated signal is not representative, since the servomotor is switched off.

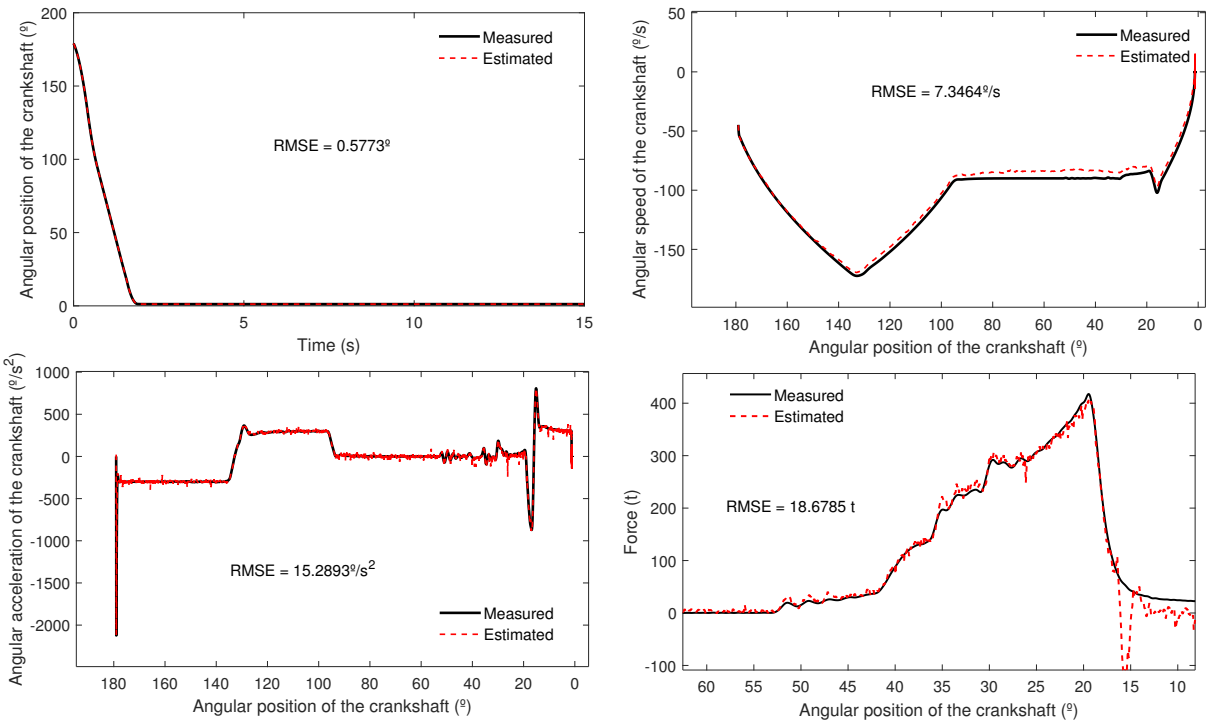

Figure 5.14: Estimation results of the process forces and states obtained in the experiment SSF1.

Figure 5.15 illustrates the estimation results of experiment SSF2 carried out by the servo press. The layout of the graphs of this figure is the same as in experiments SSF1, excepting in the case

of the force graph, where a force vs time plot is shown. The RMSE values of the estimation deviations are shown in the corresponding graphs. The angular position graph shows that the servo press was stopped at 0°, which corresponds to the BDC. Besides, the crankshaft rotated in the opposite direction to the rest of experiments, so the angular position increases in this experiment. The speed graph shows the same evolution in the measured and estimated signals. The acceleration graph also shows variability in both signals, the measured one and the estimated one. There is also a remarkable oscillation at 0° of the angular position of the crankshaft. The force graph shows a force profile that increases abruptly between seconds 5 and 6 and the decreases softly from second 6 to second 11.5, when it decreases abruptly. Looking at the force estimation graph, between seconds 11 and 12, a large peak arises due to the torque peak the PMSM exerts in response to the energy released by the servo press's structure when recovering from its elastic deformation.

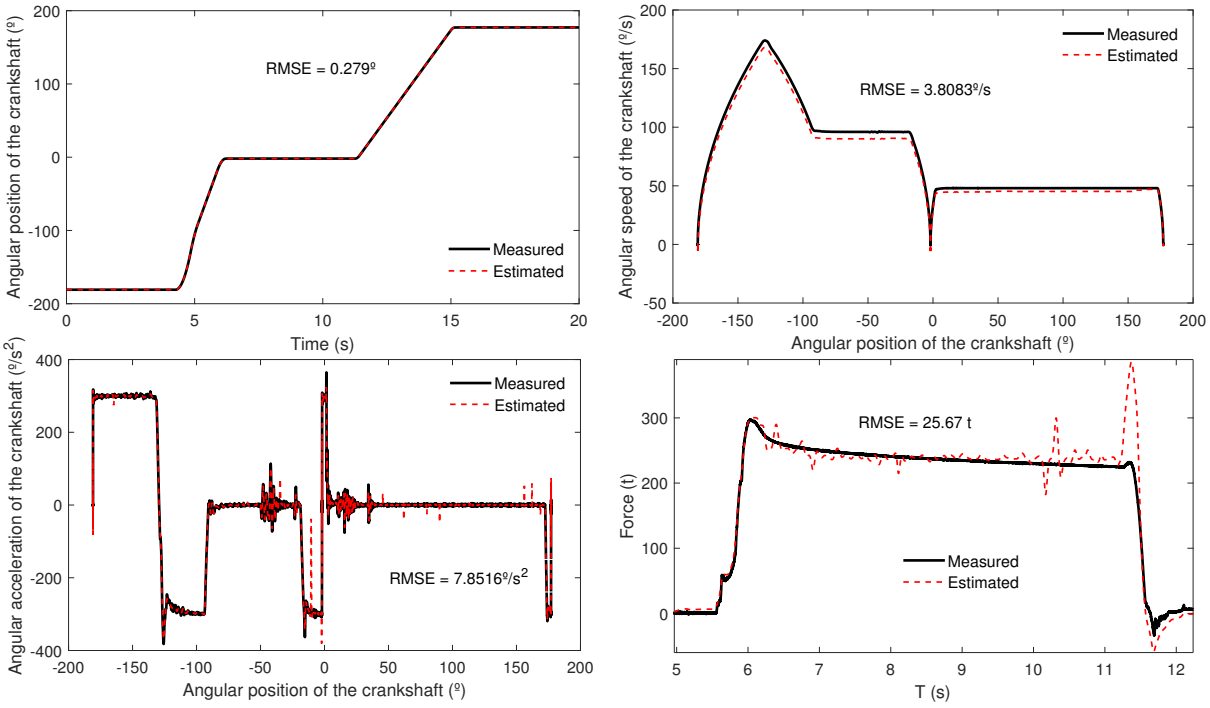

Figure 5.15: Estimation results of the process forces and states obtained in the experiment SSF2.

Figure 5.16 illustrates the instantaneous normalised absolute deviation of the estimated forces of experiment SSF1 and SSF2. The deviation in the maximum force position are pointed out in the corresponding graph. The deviation of the estimated force remains under the 5% force deviation threshold shown in the graph for almost the whole experiment, until the servo press is switched off around 18° of the angular position of the crankshaft. The deviation throughout the force profile of the experiment SSF2 remains under the 5% force deviation threshold, except in the peaks exerted in response to the energy release of the servo press's structure.

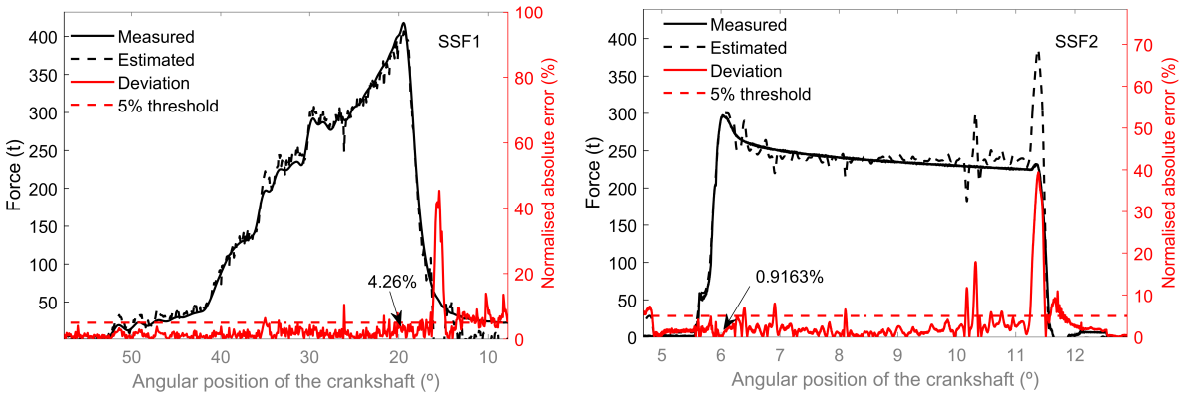

Figure 5.16: Instantaneous normalised absolute deviation of the experiment SSF1 and SFF2.

5.2 Hardware implementation of the dPF for real time estimations

The proposed dPF MBSS have been implemented in hardware to achieve a real time execution. The hardware architecture employed has already been presented in section 3.2, and is illustrated in figure 3.7.

The precision and computational time evaluation procedures are carried out as in sections "Parameters that affect precision of estimations" and "Computational time" to implement the hardware architecture of the dPF for the model of the industrial servo press. On the other hand, the variance vectors used in the proposal sampling and the variance vectors used in the weighting function are initialised as in (5.1).

$$\begin{aligned} \boldsymbol{q}_x &= \begin{bmatrix} 8t_s^4 \\ 8t_s^2 \\ 8 \end{bmatrix} & \boldsymbol{q}_d &= 4 \times 10^8 \\ \boldsymbol{\sigma}_x &= 0.1 & \boldsymbol{\sigma}_d &= 4 \times 10^8 \end{aligned} \tag{5.1}$$

5.2.1 Precision parameters

The combinations of different particle quantities are evaluated under single and double floating point arithmetic precision of the dPF variables. First, each combination of particles is tested 50 times under the single arithmetic precision to reduce the effect of the random sampling used throughout the dPF by taking the mean RMSE value. The same procedure is carried out to evaluate the estimation results under double arithmetic precision. In this case, the evaluation of the force's RMSE is slightly modified as in (5.2), to include a term that gives more importance to the maximum force point located at the BDC in most metal forming processes. As mentioned before, the BDC is critical to the safety of the servo press.

$$e = \sqrt{\frac{\sum_{k=1}^{L} \left(S_{F_k} \left(\hat{d}_k - u_{d_k} \right) \right)^2}{L}} \tag{5.2}$$

Figure 5.17 illustrates the terms of (5.2) graphically. The scaling factor is depicted by means of the green arrow, which emphasizes an incremental importance as the estimation approaches 0°.

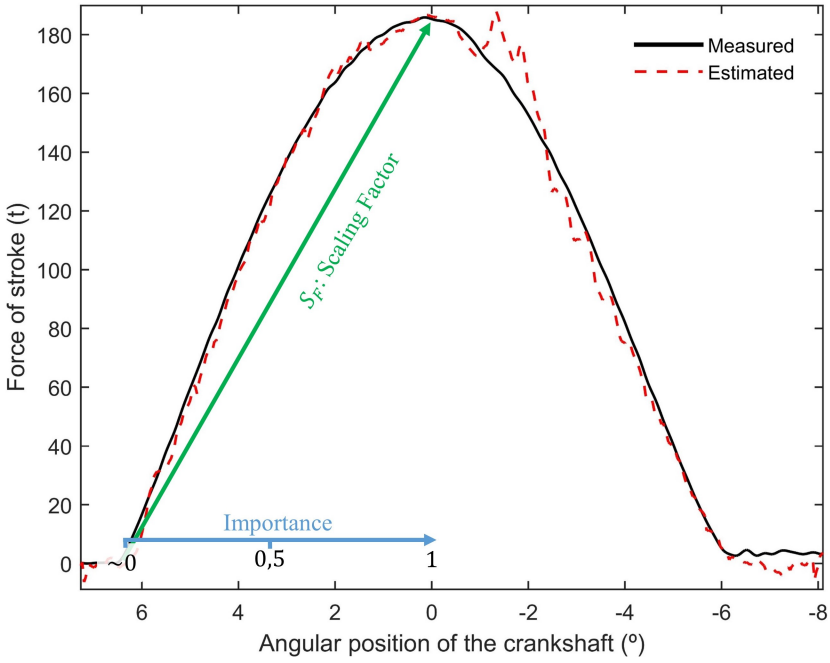

Figure 5.17: Graphical representation of the terms used in (5.2.)

Figure 5.18 shows the estimation error defined by (5.2) for all the tested combinations of particles under single and double arithmetic precisions.

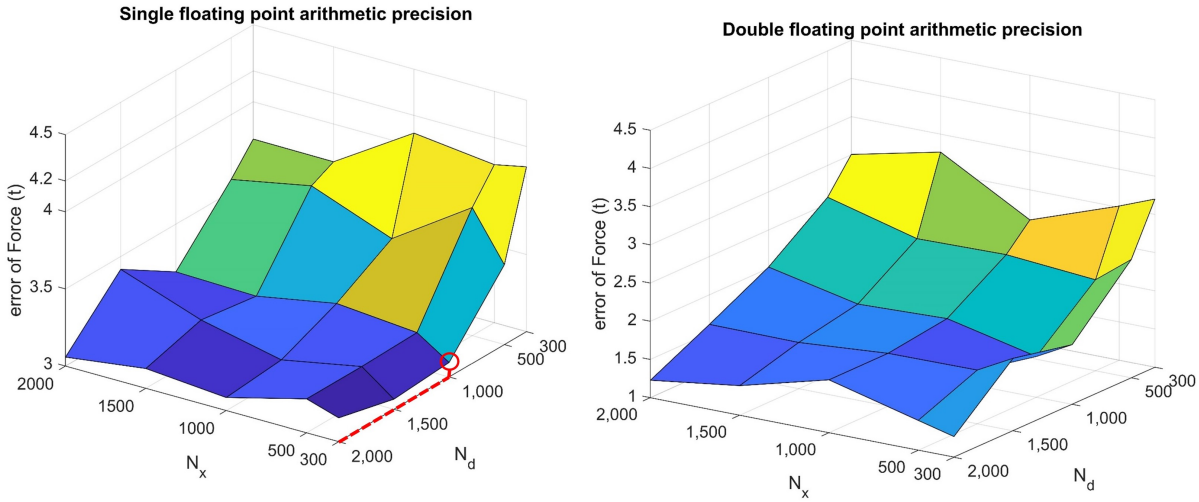

Figure 5.18: Deviation (tonnes) achieved for the tested combinations of N_x and N_d under single and double floating point arithmetic precisions.

The evaluation underlined the influence of N_x and N_d in the estimations. In both arithmetic

precisions, it can be noted that N_d has a larger impact than N_x in the estimation error. The error obtained under single and double floating point arithmetic precisions are very similar. Therefore, the combination of $N_d = 1000$ and $N_x = 300$ under single floating point arithmetic precision is selected, since the error obtained with larger values of N_x and N_d and with double floating point arithmetic precision do not improve the estimation error significantly, while increasing always the computational cost and hardware resources consumed by the dPF, as mentioned in section 3.2.

The sampling time used for the data acquisition is $t_s = 250\mu s$ for experiments of $10s$. The dPF is executed using the same PC described in section 3.1.3. On average, the execution of the dPF for a single working cycle under the chosen $N_x = 300$ and $N_d = 1000$ takes $1012s$, which corresponds to $t_s = 25.3ms$ to process each sample. Therefore, this execution time does not permit a real-time estimation of the process force, since it is more than the sampling time.

To overcome the computational time limitation of the dPF executed in a conventional PC, the afore mentioned hardware architecture is applied. As in the 2DoF MSD model presented in section 3.2.4, the Prediction & Update and Resampling loops of the dPF are pipelined to accelerate the throughput. The dPF algorithm has been implemented in Vivado® HLS. Initially the targeted initiation interval of each loop of the dPF is set as II= 1, but after the synthesis step of the hardware implementation it is modified as shown in table 5.4. These modifications are made due to dependencies among internal functions of the implemented hardware. The hardware resource utilisation and achieved computational time are also shown in table 5.4. Results on 5.4 show that the acceleration of the dPF achieves a faster execution time than the sampling time (or required latency) of the data acquisition system. Thereby, the hardware implementation of the dPF achieves to accelerate the execution time of the PC by a factor of 165.

Piece of code	**LUTs**	**FF**	**DSPs**	**BRAMs**	**II[1]**	**II[2]**	**Execution Time**
PF-UI	46176	30101	353	4	4	7	$115.35\mu s$
PF-S	48581	31712	353	4	4	7	$37.73\mu s$
Total	94757	61813	706	8	-	-	$153.08\mu s$
Available on board	230400	460800	1728	624	-	-	-
Percentage	41.13%	13.41%	40.85%	1.28%	-	-	-
Execution time in software							$25.3ms$
Required latency							$< 250\mu s$

Table 5.4: Post place & route resource utilisation and execution time.

[1] The II of the Prediction & Update loop.

[2] The II of the Resampling loop.

Chapter 6

Conclusions and future work

The work carried out during this thesis proved the hypothesis that a dPF MBSS is able estimate the process force and the dynamic behaviour of both, the test bench and the industrial servo press, under the conditions that the algorithm was evaluated.

The research carried out in this thesis provided a way to overcome the limitations of conventional hardware sensors regarding the drift and precision loss they suffer when measuring the process force of a servo press. Besides, the proposed monitoring algorithm provides more information than the conventional hardware sensors, since it is able to describe the behaviour of the entire kinematic chain of the servo press by means of the model, in addition to the process force.

To the best of the author's knowledge, the novel PF-based dPF was found to be the most generalist MBSS among the reviewed ones, as it is applicable to highly nonlinear systems. The dPF is able to estimate a variable and non-parametrised unknown input along with the states of a system. Moreover, MC based algorithms, such as the PF or the dPF, are suitable to be implemented in hardware to accelerate their execution time due to their parallelizable characteristics.

The proposed servo press model was able to explain the dynamic behaviour of the servo press using as input the electric torque of the servomotor, calculated from the three phase currents and the angular position signals obtained from the CNC. The model also includes a friction model that explains the torque that is consumed moving the servo press's components during a working cycle of the press. The friction model was evaluated under unloaded experiments as shown in subsection 2.2.1. Nevertheless, the developed dynamic model of the servo press failed to represent some deviations, such as the fluctuations in the simulated speed signal underlined in subsection 2.2.1 and the force peaks/oscillations estimated in most of the experiments of section 5.1. Fluctuations in the speed signal might be due to the unmodelled dynamics of the servo press, such as the clearances in servo press's joints. The model should also include the elastic behaviour of the servo press's components, such as the gears and the structure of the servo press, to describe their deformation when the process force is applied.

The proposed dPF-based process force monitoring algorithm was evaluated in a scaled test bench and in an industrial servo press. The estimation of the process force and the dynamic behaviour in the reduced scale test bench, validated the dPF algorithm in lab conditions. Two experiments were carried out where different force levels were applied. The deviation of the estimated force at the maximum force position (the BDC) were lower than 1.5% in both experiments compared to the measured force. In respect of the experimental validation in the industrial servo press, three different metal forming processes under several force levels and angular speed conditions were tested. Obtained estimations of the state variables and the process force were compared with their respective measured signals provided by physical sensors. The estimations carried out by the proposed dPF MBSS achieved a force deviation lower than 5%, excepting in the region of the torque peaks exerted by the servomotor. As mentioned before, these torque peaks/oscillations are commanded by the CNC to compensate the speed variations produced by the energy release of the servo press's structure when recovering from its elastic deformation.

The hardware implementation of the dPF allowed to estimate the process force and the state variables of a servo press in real time. The proposed methodology allowed to design an efficient hardware architecture for the dPF, as it guaranteed the minimum use of hardware resources for the required latency. This is achieved by means of the evaluation of the trade-off between the precision of estimations and the hardware resource utilisation. To ensure the required latency and a deterministic execution time of the dPF, step (g) of the two PFs of the dPF had to be modified, employing a binary search algorithm for the Resampling loop.

The developed similitude based scaling approach provided a complete design, optimisation and manufacturing methodology to build a scaled test bench able to emulate the dynamic behaviour of the industrial servo press. The activity analysis showed the relevance of each component of the servo press in its dynamic behaviour, allowing to define tolerances to ease the manufacturing process without altering the dynamic similitude significantly. The manufactured servo press test bench kept the dynamic similitude with the industrial servo press with a mean deviation of 5.08% in the emulated force profiles.

6.1 Contributions

The most important contributions of this thesis are the developed dynamic model of the servo press and the dPF MBSS that is able to estimate the process force (modelled as an unknown input) and the state variables during the whole cycle of the servo press using exclusively already available current and angular position signals of the servomotor.

The proposed dPF MBSS contributed to the estimation of an unknown input and the states of the evaluated systems, being them linear or highly nonlinear, taking advantage of a model and the available signals. The dPF was tested by means of simulated and experimental signals in a two DoF system and in two servo press models (the scaled test bench and the industrial servo press). The hardware implementation of the dPF allowed a real time execution of the algorithm.

The conducted literature review showed the advantages, limitations and the applicability of the analysed MBSS. The MBSSs table presented in the 1.4 section provides a summarised information about the applicability and characteristics of the reviewed MBSS. The hypothesis of this research work was formulated based on the discussion of the literature review.

The developed servo press model improved the existing models by including the electric and mechanical subsystems of the machine in a single model. Moreover, it also comprises a friction model that explains the torque losses produced in both, the servo press transition from static to dynamic regime and in continuous operation.

This thesis also improved the similitude based scaling methodology. The methodology presented, first, determines the dimensionless groups to define several scaling laws based on the Buckingham's π theorem, which are used to scale a test bench. Then, a constrained optimisation approach is used to obtain the optimal values of the scaled system's magnitudes. Finally, manufacturing tolerances are determined for the manufacturing of the system's components based on the activities of the optimised parameters. The implementation of this methodology guarantees a faithful scaling, keeping the kinematic and dynamic similitude with thee original system, according to the established design requirements and constraints.

6.2 Future research lines

The estimation of the process force and the state variables of the servo press model opens the possibility of developing a predictive maintenance in servo press facilities to detect faulty operation conditions and prevent deviations in the produced parts. The continuous monitoring of these estimands may emphasize deviations from the nominal operation conditions of the machine. Deviations may be traced to the defective components, and therefore, servo press users may introduce corrective actions to fix the causes of those deviations. The developed hardware architecture may contribute to the quick detection of failure and harmful operation conditions, preventing the servo press from suffering damages.

Furthermore, regarding the control of the process, the real time execution of the dPF may provide a means to create adaptive control strategies to improve the quality of the produced parts. Knowledge of the instantaneous estimated (filtered) ram's position, speed and acceleration extracted from the model, along with the process force, may be used to command specific force levels at each operation point of the forming cycle.

The servo press model could also be improved to include other phenomena such as the effect of clearances between components' joints or deformation of components. The modelling of these phenomena might reduce the deviations found in the obtained speed of the crankshaft and the estimated force peaks/oscillations due to the elastic recovery of the servo press's structure. A more exhaustive servo press condition and process monitoring might be carried out including these phenomena in the model.

Regarding the scaling methodology proposed in this dissertation, it may be adopted to optimally scale other industrial machines keeping the dynamic similitude with the original system. Besides, the parameters' activity analysis may be used to design and manufacture scaled test benches, so that the energy consumption of their components is efficient and optimal for the required process. This may contribute to a saving of the system's energy consumption.

Apart from the future lines this thesis opens in terms of monitoring and control methods in the servo press industry, the proposed dPF can be applied to other machines, processes or sectors to carry out the estimation of the modelled states and an unknown input.

Bibliography

Aiken, A. and A. Nicolau (1988). "Perfect pipelining: A new loop parallelization technique". In: *ESOP '88*. Ed. by H. Ganzinger. Berlin, Heidelberg: Springer Berlin Heidelberg, pp. 221–235. ISBN: 978-3-540-38941-5.

Ali, J. M., N. H. Hoang, M. A. Hussain, and D. Dochain (2015). "Review and classification of recent observers applied in chemical process systems". In: *Computers & Chemical Engineering* 76, pp. 27–41.

Altan, T. and A. E. Tekkaya (2012a). *Sheet metal forming: fundamentals*. Asm International.

Altan, T. and A. E. Tekkaya (2012b). *Sheet metal forming: processes and applications*. Asm International.

Alves, J., J. Ferreira, J. Lobo, and J. Dias (2015). "Brief survey on computational solutions for Bayesian inference". In: *Workshop on Unconventional computing for Bayesian inference*.

Arroyo, E. L. C. (2006). "Modeling and simulation of permanent magnet synchronous motor drive system". In: *University of puerto rico, Mayagüez Campus*.

Arulampalam, M. S., S. Maskell, N. Gordon, and T. Clapp (2002). "A tutorial on particle filters for online nonlinear/non-Gaussian Bayesian tracking". In: *IEEE Transactions on signal processing* 50.2, pp. 174–188.

Baker, W. E., P. S. Westine, and F. T. Dodge (1973). *Similarity methods in engineering dynamics: theory and practice of scale modeling*. Spartan Books;[distributed by] Hayden Book Co.

Bellman, R. (1964). *Stochastic processes in mathematical physics and engineering*. American Mathematical Society.

Benjak, O. and D. Gerling (2010). "Review of position estimation methods for PMSM drives without a position sensor, part III: Methods based on saliency and signal injection". In: *Electrical Machines and Systems (ICEMS), 2010 International Conference on*. IEEE, pp. 873–878.

Borutzky, W. (2011). *Bond graph modelling of engineering systems*. Springer.

Brennan, S. and A. Alleyne (2001). "Using a scale testbed: Controller design and evaluation". In: *IEEE Control Systems Magazine* 21.3, pp. 15–26.

Buckingham, E. (1914). "On physically similar systems; illustrations of the use of dimensional equations". In: *Physical review* 4.4, p. 345.

Candy, J. V. (2016). *Bayesian signal processing: classical, modern, and particle filtering methods*. Vol. 54. John Wiley & Sons. DOI: 10.1016/j.precisioneng.2013.06.007.

Chen, J. and R. J. Patton (2012). *Robust model-based fault diagnosis for dynamic systems*. Vol. 3. Springer Science & Business Media.

Chiew, T., Z. Jamaludin, A. B. Hashim, N. Rafan, and L. Abdullah (2013). "Identification of friction models for precise positioning system in machine tools". In: *Procedia Engineering* 53, pp. 569–578.

Chin, J.-W., S.-W. Hwang, H.-J. Park, and J.-P. Hong (2018). "Thermal Analysis and Verification of PMSM Using LPTN Considering Mechanical Components and Losses". In: *2018 XIII International Conference on Electrical Machines (ICEM)*. IEEE, pp. 1323–1329.

Chowdhary, G. and R. Jategaonkar (2010). "Aerodynamic parameter estimation from flight data applying extended and unscented Kalman filter". In: *Aerospace science and technology* 14.2, pp. 106–117.

Council, N. S. (2004). *Inspection and maintenance of mechanical power presses*. Tech. rep. National Safety Council.

Coutinho, C. P., A. J. Baptista, and J. D. Rodrigues (2016). "Reduced scale models based on similitude theory: a review up to 2015". In: *Engineering Structures* 119, pp. 81–94.

Curtis, W., J. D. Logan, and W. Parker (1982). "Dimensional analysis and the pi theorem". In: *Linear Algebra and its Applications* 47, pp. 117–126.

Darouach, M. (1994). "On the novel approach to the design of unknown input observers". In: *IEEE Transactions on Automatic Control* 39.3, pp. 698–699.

Davies, R. (2015). "Industry 4.0. Digitalisation for productivity and growth". In: *Briefing from EPRS. European Parliamentary Research Service*.

Del Moral, P. (1996). "Non-linear filtering: interacting particle resolution". In: *Markov processes and related fields* 2.4, pp. 555–581.

Doege, E., F. Meiners, T. Mende, W. Strache, and J. W. Yun (May 2002). "Sensors for Process Monitoring: Metal Forming". In: *Sensors in Manufacturing*. Wiley-VCH Verlag GmbH, pp. 172–202. DOI: 10.1002/3527600027.ch4b.

Doraiswami, R. and L. Cheded (2014). "Robust model-based soft sensor: design and application". In: *IFAC Proceedings Volumes* 47.3, pp. 5491–5496. DOI: 10.3182/20140824-6-ZA-1003.00245.

Esteban, E., O. Salgado, A. Iturrospe, and I. Isasa (2016). "Model-based approach for elevator performance estimation". In: *Mechanical Systems and Signal Processing* 68, pp. 125–137.

Esteban, E., O. Salgado, A. Iturrospe, and I. Isasa (2017). "Design methodology of a reduced-scale test bench for fault detection and diagnosis". In: *Mechatronics* 47, pp. 14–23.

Eurostat (2016). *Structural Business Statistics - Main Indicators*. Database.

Faragher, R. et al. (2012). "Understanding the basis of the Kalman filter via a simple and intuitive derivation". In: *IEEE Signal processing magazine* 29.5, pp. 128–132.

Fortuna, L., S. Graziani, A. Rizzo, and M. G. Xibilia (2007). *Soft sensors for monitoring and control of industrial processes*. Springer Science & Business Media.

functionbay (2016). *Permanent magnet synchronous machine*. Accessed: 2019-08-02.

Garcia, E. A. and P. Frank (1997). "Deterministic nonlinear observer-based approaches to fault diagnosis: a survey". In: *Control Engineering Practice* 5.5, pp. 663–670.

Gelman, A., H. S. Stern, J. B. Carlin, D. B. Dunson, A. Vehtari, and D. B. Rubin (2013). *Bayesian data analysis*. Chapman and Hall/CRC.

Ghiotti, A., P. Regazzo, S. Bruschi, and P. Bariani (2010). "Reduction of vibrations in blanking by MR dampers". In: *CIRP Annals-Manufacturing Technology* 59.1, pp. 275–278.

Ghiotti, A., S. Bruschi, and P. Regazzo (2014). "Shear surface control in blanking by adaptronic systems". In: *Procedia Engineering* 81, pp. 2512–2517.

Gieras, J. F. (2002). *Permanent magnet motor technology: design and applications*. CRC press.

Gilks, W. R., S. Richardson, and D. Spiegelhalter (1995). *Markov chain Monte Carlo in practice*. CRC press.

Gordon, N., B. Ristic, and S. Arulampalam (2004). "Beyond the kalman filter: Particle filters for tracking applications". In: *Artech House, London* 830, p. 5.

Ha, J.-L., R.-F. Fung, K.-Y. Chen, and S.-C. Hsien (2006). "Dynamic modeling and identification of a slider-crank mechanism". In: *Journal of sound and vibration* 289.4, pp. 1019–1044.

Halicioglu, R., L. C. Dulger, and A. T. Bozdana (2016a). "Mechanisms, classifications, and applications of servo presses: A review with comparisons". In: *Proceedings of the Institution of Mechanical Engineers, Part B: Journal of Engineering Manufacture* 230.7, pp. 1177–1194.

Halicioglu, R., L. C. Dulger, and A. T. Bozdana (2016b). "Modeling, design, and implementation of a servo press for metal-forming application". In: *The International Journal of Advanced Manufacturing Technology*, pp. 1–12.

Hammersley, J. M. and D. C. Handscomb (1964). "Monte Carlo methods". In:

Haseltine, E. L. and J. B. Rawlings (2005). "Critical evaluation of extended Kalman filtering and moving-horizon estimation". In: *Industrial & engineering chemistry research* 44.8, pp. 2451–2460.

Hastings, W. K. (1970). "Monte Carlo sampling methods using Markov chains and their applications". In: *Biometrika* 57.1, pp. 97–109.

He, K., W. Li, and R. Du (2006). "Dynamic modelling with kineto-static method and experiment validation of a novel controllable mechanical metal forming press". In: *International Journal of Manufacturing Research* 1.3, pp. 354–378.

Hsu, P.-L., Y.-C. Houng, and S.-S. Yeh (2001). "Design of an optimal unknown input observer for load compensation in motion systems". In: *Asian Journal of Control* 3.3, pp. 204–215.

Huang, S. and G. Dissanayake (2007). "Convergence and consistency analysis for extended Kalman filter based SLAM". In: *IEEE Transactions on robotics* 23.5, pp. 1036–1049.

Huh, S.-H., S.-J. Seo, I. Choy, and G.-T. Park (2007). "Design of a robust stable flux observer for induction motors". In: *Journal of Electrical Engineering and Technology* 2.2, pp. 280–285.

Jianbo, C., H. Yuwen, H. Wenxin, L. Yong, Y. Jianfei, and W. Mingjin (2009). "Direct active and reactive power control of PMSM". In: *Power Electronics and Motion Control Conference, 2009. IPEMC'09. IEEE 6th International*. IEEE, pp. 1808–1812.

Julier, S. J. and J. K. Uhlmann (1997). "A new extension of the Kalman filter to nonlinear systems". In: *Int. symp. aerospace/defense sensing, simul. and controls*. Vol. 3. 26. Orlando, FL, pp. 182–193.

Kadlec, P., B. Gabrys, and S. Strandt (2009). "Data-driven soft sensors in the process industry". In: *Computers & Chemical Engineering* 33.4, pp. 795–814.

Kalman, R. E. et al. (1960). "A new approach to linear filtering and prediction problems". In: *Journal of basic Engineering* 82.1, pp. 35–45.

Keith, M. R. (2002). *An introduction to predictive maintenance*.

Khalil, W. (2011). "Dynamic modeling of robots using Newton-Euler formulation". In: *Informatics in Control, Automation and Robotics*. Springer, pp. 3–20.

Khemili, I. and L. Romdhane (2008). "Dynamic analysis of a flexible sliderÔÇôcrank mechanism with clearance". In: *European Journal of Mechanics - A/Solids* 27.5, pp. 882–898. ISSN: 0997-7538. DOI: https://doi.org/10.1016/j.euromechsol.2007.12.004. URL: http://www.sciencedirect.com/science/article/pii/S0997753807001234.

Kitagawa, G. and W. Gersch (2012). *Smoothness priors analysis of time series*. Vol. 116. Springer Science & Business Media.

Kittirungsi, B. (2008). *A scaling methodology for dynamic systems: Quantification of approximate similitude and use in multiobjective design*. ProQuest.

Kline, S. J. (2012). *Similitude and approximation theory*. Springer Science & Business Media.

Konatowski, S., P. Kaniewski, and J. Matuszewski (2016). "Comparison of estimation accuracy of EKF, UKF and PF filters". In: *Annual of Navigation* 23.1, pp. 69–87.

Kristensen, N. R., H. Madsen, and S. B. Jørgensen (2004). "Parameter estimation in stochastic grey-box models". In: *Automatica* 40.2, pp. 225–237.

Kumme, R., O. Mack, B. Bill, C. Gossweiler, H. Haab, and K. I. AG (2002). "Dynamic properties and investigations of piezoelectric force measuring devices". In: *VDI BERICHTE* 1685, pp. 161–172.

Kung, Y.-S., N. P. Thanh, and M.-S. Wang (2015). "Design and simulation of a sensorless permanent magnet synchronous motor drive with microprocessor-based PI controller and dedicated hardware EKF estimator". In: *Applied Mathematical Modelling* 39.19, pp. 5816–5827.

Lahiri, S. K. (2017). *Multivariable Predictive Control: Applications in Industry*. John Wiley & Sons.

Lebedev, I., S. Cheng, A. Doupnik, J. Martin, C. Fletcher, D. Burke, M. Lin, and J. Wawrzynek (2010). "MARC: A many-core approach to reconfigurable computing". In: *Reconfigurable Computing and FPGAs (ReConFig), 2010 International Conference on*. IEEE, pp. 7–12.

Lebedev, I., C. Fletcher, S. Cheng, J. Martin, A. Doupnik, D. Burke, M. Lin, and J. Wawrzynek (2012). "Exploring many-core design templates for FPGAs and ASICs". In: *International Journal of Reconfigurable Computing* 2012, p. 8.

Lee, J., B. Bagheri, and H.-A. Kao (2015). "A cyber-physical systems architecture for industry 4.0-based manufacturing systems". In: *Manufacturing Letters* 3, pp. 18–23.

Lin, M., I. Lebedev, and J. Wawrzynek (2010). "High-throughput bayesian computing machine with reconfigurable hardware". In: *Proceedings of the 18th annual ACM/SIGDA international symposium on Field programmable gate arrays*. ACM, pp. 73–82.

Liu, C., S. Zhao, X. Han, and T. Guo (2017). "High-accuracy servo press system for the clinching joint process". In: *Journal of Mechanical Science and Technology* 31.2, pp. 903–910.

Liu, S., G. Mingas, and C.-S. Bouganis (2014). "Parallel resampling for particle filters on FPGAs". In: *2014 International Conference on Field-Programmable Technology (FPT)*. IEEE, pp. 191–198.

Liu, S., G. Mingas, and C.-S. Bouganis (2017). "An unbiased mcmc fpga-based accelerator in the land of custom precision arithmetic". In: *IEEE Transactions on Computers* 5, pp. 745–758.

Ljung, L. (1979). "Asymptotic behavior of the extended Kalman filter as a parameter estimator for linear systems". In: *IEEE Transactions on Automatic Control* 24.1, pp. 36–50.

Ljung, L. (2002). "Prediction error estimation methods". In: *Circuits, Systems and Signal Processing* 21.1, pp. 11–21.

Lozares, J., G. Plata, I. Hurtado, Z. Azpilgain, and I. Loizaga (2019). "Semisolid Forging of 250 Automotive Spindles of S48C Steel". In: *Solid State Phenomena*. Vol. 285. Trans Tech Publ, pp. 411–416.

Luenberger, D. (1966). "Observers for multivariable systems". In: *IEEE Transactions on Automatic Control* 11.2, pp. 190–197.

Mejri, S., A. S. Tlili, and N. B. Braiek (2013). "Particle Filter for State and Unknown Input Estimation of Chaotic Systems". In: *Proceedings Engineering & Technology-Vol* 4, pp. 67–72.

Merzoug, M., F. Naceri, et al. (2008). "Comparison of field-oriented control and direct torque control for permanent magnet synchronous motor (PMSM)". In: *World Academy of Science, Engineering and Technology* 45, pp. 299–304.

Mingas, G. (2015). "Algorithms and architectures for MCMC acceleration in FPGAs". PhD thesis. Imperial College London.

Mingas, G., L. Bottolo, and C.-S. Bouganis (2017). "Particle MCMC algorithms and architectures for accelerating inference in state-space models". In: *International Journal of Approximate Reasoning* 83, pp. 413–433.

Mingas, G. and C.-S. Bouganis (2012). "Parallel tempering MCMC acceleration using reconfigurable hardware". In: *International Symposium on Applied Reconfigurable Computing*. Springer, pp. 227–238.

Mingas, G. and C.-S. Bouganis (2016). "Population-based MCMC on multi-core CPUs, GPUs and FPGAs". In: *IEEE Transactions on Computers* 65.4, pp. 1283–1296.

Mustière, F., M. Bolic, and M. Bouchard (2009). "Speech enhancement based on nonlinear models using particle filters". In: *IEEE transactions on neural networks* 20.12, pp. 1923–1937.

Ogata, K. (2010). *Modern Control Engineering*. 5th ed. Prentice Hal. ISBN: 978-0136156734.

Ohm, D. Y. (2000). "Dynamic model of PM synchronous motors". In: *Drivetech, Inc., Blacksburg, Virginia, www. drivetechinc. com* 16.

Osakada, K., K. Mori, T. Altan, and P. Groche (2011). "Mechanical servo press technology for metal forming". In: *CIRP Annals-Manufacturing Technology* 60.2, pp. 651–672.

Pan, S., D. Xiao, S. Xing, S. Law, P. Du, and Y. Li (2016). "A general extended Kalman filter for simultaneous estimation of system and unknown inputs". In: *Engineering Structures* 109, pp. 85–98.

Park, R. H. (1929). "Two-reaction theory of synchronous machines generalized method of analysis-part I". In: *Transactions of the American Institute of Electrical Engineers* 48.3, pp. 716–727.

Patton, R., F. Uppal, and C. Lopez-Toribio (2000). "Soft computing approaches to fault diagnosis for dynamic systems: a survey". In: *IFAC Proceedings Volumes* 33.11, pp. 303–315.

Peresada, S., A. Tilli, and A. Tonielli (Nov. 1999). "Robust output feedback control of a doubly-fed induction machine". In: *Proc. 25th Annual Conf. of the IEEE Industrial Electronics Society (Cat. No.99CH37029) IECON'99*. Vol. 3, 1348–1354 vol.3. DOI: 10.1109/IECON.1999.819407.

Plunkett, A. B. (Mar. 1989). *Field orientation control of a permanent magnet motor*. US Patent 4,814,677.

Radke, A. and Z. Gao (2006). "A survey of state and disturbance observers for practitioners". In: *American Control Conference, 2006*. IEEE, 6–pp.

Renard, P., A. Alcolea, and D. Ginsbourger (2013). "Stochastic versus Deterministic Approaches". In: *Environmental Modelling*. John Wiley & Sons, Ltd. Chap. 8, pp. 133–149. ISBN: 9781118351475. DOI: 10.1002/9781118351475.ch8. eprint: https://onlinelibrary.wiley.com/doi/pdf/10.1002/9781118351475.ch8. URL: https://onlinelibrary.wiley.com/doi/abs/10.1002/9781118351475.ch8.

Rizzo, A. (2010). "Soft sensors and artificial intelligence for nuclear fusion experiments". In: *MELECON 2010-2010 15th IEEE Mediterranean Electrotechnical Conference*. IEEE, pp. 1068–1072.

Särkkä, S. (2013). *Bayesian filtering and smoothing*. Vol. 3. Cambridge University Press.

Schuler (1998). *Metal forming handbook*. Springer Science & Business Media.

Senda, M., H. Yoshida, A. Harada, K. Hishinuma, H. Kawabuchi, H. Matsuda, Y. Harada, and K. Honjo (May 2014). *Method and apparatus for controlling electric servo press*. US Patent 8,726,802.

Sharma, P. C. (1999). *A Textbook of Production Enginerring*. S. Chand Publishing.

Shieh, J., J. Huber, N. Fleck, and M. Ashby (2001). "The selection of sensors". In: *Progress in materials science* 46.3, pp. 461–504.

Sileshi, B., J. Oliver, and C. Ferrer (2016). "Accelerating Particle Filter on FPGA". In: *VLSI (ISVLSI), 2016 IEEE Computer Society Annual Symposium on*. IEEE, pp. 591–594.

Simitses, G. J. (2001). "Structural similitude for flat laminated surfaces". In: *Composite structures* 51.2, pp. 191–194.

Simitses, G. J. and J. Rezaeepazhand (1992). "Structural similitude and scaling laws for laminated beam-plates". In:

Singhatanadgid, P. and V. Ungbhakorn (2002). "Buckling similitude invariants of symmetrically laminated plates subjected to biaxial loading". In: *SEM Annual Conference and Exposition*, pp. 10–12.

Spitler, D., J. G. Nee, D. A. Smith, and J. Lantrip (2003). *Fundamentals of tool design*. 5th ed. Society of Manufacturing Engineers. ISBN: 0-87263-650-X,9780872636507,9780872636613,0872636615.

Suja, R., P. M. Mary, and P. S. Karuvelem (2016). "Field Oriented Control of Permanent Magnet Synchronous Motor". In: *Asian Journal of Research in Social Sciences and Humanities* 6.11, pp. 261–273.

Szirtes, T. (2007). *Applied dimensional analysis and modeling*. Butterworth-Heinemann.

Thrun, S., D. Fox, W. Burgard, and F. Dellaert (2001). "Robust Monte Carlo localization for mobile robots". In: *Artificial intelligence* 128.1-2, pp. 99–141.

Ungbhakorn, V. and N. Wattanasakulpong (2007). "Structural similitude and scaling laws of anti-symmetric cross-ply laminated cylindrical shells for buckling and vibration experiments". In: *International Journal of Structural Stability and Dynamics* 7.04, pp. 609–627.

Vaschy, A. (1892). "Sur les lois de similitude en physique". In: *Annales télégraphiques*. Vol. 19, pp. 25–28.

Virgala, I., P. Frankovskỳ, and M. Kenderová (2013). "Friction effect analysis of a DC motor". In: *American Journal of Mechanical Engineering* 1.1, pp. 1–5.

Wan, E. A. and R. Van Der Merwe (2000). "The unscented Kalman filter for nonlinear estimation". In: *Adaptive Systems for Signal Processing, Communications, and Control Symposium 2000. AS-SPCC. The IEEE 2000*. Ieee, pp. 153–158.

Wang, X., T. Li, S. Sun, and J. Corchado (2017). "A survey of recent advances in particle filters and remaining challenges for multitarget tracking". In: *Sensors* 17.12, p. 2707.

Webster, J. G. and H. Eren (2014). *Measurement, instrumentation, and sensors handbook: spatial, mechanical, thermal, and radiation measurement*. Vol. 1. CRC press.

Widodo, A. and B.-S. Yang (2007). "Support vector machine in machine condition monitoring and fault diagnosis". In: *Mechanical systems and signal processing* 21.6, pp. 2560–2574.

Wilson, J. S. (2005). *Sensor technology handbook*.

Yan, W., P. Guo, Y. Tian, and J. Gao (2016). "A Framework and Modeling Method of Data-Driven Soft Sensors Based on Semisupervised Gaussian Regression". In: *Industrial & Engineering Chemistry Research* 55.27, pp. 7394–7401.

Yu, S., Y. Liu, and L. Li (Apr. 2013). "Comparative life cycle assessment of servo press and flywheel press". In: *Re-engineering Manufacturing for Sustainability*. Springer, pp. 515–521. DOI: 10.1007/978-987-4451-48-2.

Zarei, J. and J. Poshtan (2010). "Design of nonlinear unknown input observer for process fault detection". In: *Industrial & Engineering Chemistry Research* 49.22, pp. 11443–11452.

Zhang, P. (2010). *Advanced industrial control technology*. William Andrew.

Zheng, E. and X. Zhou (2014). "Modeling and simulation of flexible slider-crank mechanism with clearance for a closed high speed press system". In: *Mechanism and Machine Theory* 74, pp. 10–30. ISSN: 0094-114X. DOI: https://doi.org/10.1016/j.mechmachtheory.2013.11.015. URL: http://www.sciencedirect.com/science/article/pii/S0094114X13002425.

Zhou, J., X. Li, A. J. Andernroomer, H. Zeng, K. M. Goh, Y. Wong, and G. S. Hong (2005). "Intelligent prediction monitoring system for predictive maintenance in manufacturing". In: *Industrial Electronics Society, 2005. IECON 2005. 31st Annual Conference of IEEE*. IEEE, 6–pp.

Zhu, L. (2008). *Adaptive control of sinusoidal brushless DC motor actuators*. Michigan Technological University.

Appendices

Appendix A

Mechanical subsystem derivation

A.1 Lagrange's equations of motion for the mechanical subsystem

Lagrange's equation of motion is defined based the obtained Lagrange function A.1 written in the generalised coordinate θ.

$$\begin{aligned} L = \frac{1}{2}\dot{\theta}^2 \Bigg(& I_1 + m_1 \acute{r}^2 + \frac{I_2 r^2 \cos^2(\theta)}{c^2} + \frac{\left(l - \acute{l}\right)^2}{l^2} m_2 r^2 \cos^2(\theta) + \sin^2(\theta) \\ & \left(m_2 r^2 \frac{\left(r\acute{l}\cos(\theta) + lc\right)^2}{l^2 c^2} + m_3 r^2 \frac{(r\cos(\theta) + c)^2}{c^2} \right) + I_4 + I_5 \eta_4^2 + I_6 \left(\eta_4 \eta_5\right)^2 \\ & + I_7 \left(\eta_4 \eta_5 \eta_6\right)^2 \Bigg) + g \left(\cos(\theta) \left(m_1 \acute{r} + m_2 r + m_3 r\right) + m_2 \frac{\acute{l}}{l} c + m_3 c \right) \end{aligned} \tag{A.1}$$

$$\frac{d}{dt}\left(\frac{dL}{d\dot{q}_k}\right) - \frac{dL}{dq_k} = Q_k \qquad k = 1, 2, ..n \tag{A.2}$$

Partial derivatives of the Lagrange's equation of motion are shown from equation A.3 to A.5.

$$\begin{aligned} \frac{dL}{d\dot{\theta}} = \ddot{\theta} \Bigg(& I_1 + m_1 \acute{r}^2 + \frac{I_2 r^2 \cos^2(\theta)}{c^2} + \frac{\left(l - \acute{l}\right)^2}{l^2} m_2 r^2 \cos^2(\theta) \\ & + \sin^2(\theta) \left(m_2 r^2 \frac{\left(r\acute{l}\cos(\theta) + lc\right)^2}{l^2 c^2} + m_3 r^2 \frac{(r\cos(\theta) + c)^2}{c^2} \right) \\ & + I_4 + I_5 \eta_4^2 + I_6 \left(\eta_4 \eta_5\right)^2 + I_7 \left(\eta_4 \eta_5 \eta_6\right)^2 \Bigg) \end{aligned} \tag{A.3}$$

$$\begin{aligned}\frac{d}{dt}\left(\frac{dL}{d\dot{\theta}}\right) = \ddot{\theta}\Bigg(& I_1 + m_1\acute{r}^2 + \frac{I_2 r^2\cos^2(\theta)}{c^2} + \frac{\left(l-\acute{l}\right)^2}{l^2}m_2 r^2\cos^2(\theta) \\ & + \sin^2(\theta)\left(m_2 r^2\frac{\left(r\acute{l}\cos(\theta)+lc\right)^2}{l^2c^2} + m_3 r^2\frac{(r\cos(\theta)+c)^2}{c^2}\right) \\ & + I_4 + I_5\eta_4^2 + I_6\left(\eta_4\eta_5\right)^2 + I_7\left(\eta_4\eta_5\eta_6\right)^2\Bigg) \\ & + \dot{\theta}^2\Bigg(\frac{2I_2 r^4\cos^3(\theta)\sin(\theta)}{c^4} - \frac{2I_2 r^2\cos(\theta)\sin(\theta)}{c} - \frac{2m_2 r^2\cos(\theta)\sin(\theta)\left(l-\acute{l}\right)^2}{l^2} \\ & + 2\sin(\theta)\cos(\theta)\left(m_2 r^2\frac{\left(r\acute{l}\cos(\theta)+lc\right)^2}{l^2c^2} + m_3 r^2\frac{(r\cos(\theta)+c)^2}{c^2}\right) + 2\sin^2(\theta) \\ & \left(\frac{m_2 r^3\acute{l}\sin(\theta)\left(r\acute{l}\cos(\theta)+lc\right)(r\cos(\theta)-c)(r\cos(\theta)+c)}{l^2c^4}\right. \\ & \left.\frac{m_3 r^3\sin(\theta)(r\cos(\theta)+c)^2(r\cos(\theta)-c)}{c^4}\right)\Bigg)\end{aligned} \tag{A.4}$$

$$\begin{aligned}\frac{dL}{d\theta} = \frac{1}{2}\dot{\theta}^2\Bigg(& \frac{2I_2 r^4\cos^3(\theta)\sin(\theta)}{c^4} - \frac{2I_2 r^2\cos(\theta)\sin(\theta)}{c} - \frac{2m_2 r^2\cos(\theta)\sin(\theta)\left(l-\acute{l}\right)^2}{l^2} \\ & + 2\sin(\theta)\cos(\theta)\left(m_2 r^2\frac{\left(r\acute{l}\cos(\theta)+lc\right)^2}{l^2c^2} + m_3 r^2\frac{(r\cos(\theta)+c)^2}{c^2}\right) + 2\sin^2(\theta) \\ & \left(\frac{m_2 r^3\acute{l}\sin(\theta)\left(r\acute{l}\cos(\theta)+lc\right)(r\cos(\theta)-c)(r\cos(\theta)+c)}{l^2c^4}\right. \\ & \left.\frac{m_3 r^3\sin(\theta)(r\cos(\theta)+c)^2(r\cos(\theta)-c)}{c^4}\right)\Bigg) \\ & - g\left(\sin(\theta)\left(m_1\acute{r}+m_2 r+m_3 r\right) + \sin(\theta)\cos(\theta)\left(\frac{m_2 r^2\acute{l}}{lc} + \frac{m_3 r^2}{c}\right)\right)\end{aligned} \tag{A.5}$$

Substituting equations A.3, A.4 and A.5 in A.2, equation A.6 is obtained, which represents the dynamic model of the mechanical subsystem.

$$\ddot{\theta}\left(I_1+m_1\acute{r}^2+\frac{I_2r^2\cos^2(\theta)}{c^2}+\frac{\left(l-\acute{l}\right)^2}{l^2}m_2r^2\cos^2(\theta)+\sin^2(\theta)\left(m_2r^2\frac{\left(r\acute{l}\cos(\theta)+lc\right)^2}{l^2c^2}\right.\right.$$
$$\left.\left.+m_3r^2\frac{(r\cos(\theta)+c)^2}{c^2}\right)+I_4+I_5\eta_4^2+I_6\left(\eta_4\eta_5\right)^2+I_7\left(\eta_4\eta_5\eta_6\right)^2\right)$$
$$+\frac{1}{2}\dot{\theta}^2\left(\frac{2I_2r^4\cos^3(\theta)\sin(\theta)}{c^4}-\frac{2I_2r^2\cos(\theta)\sin(\theta)}{c}-\frac{2m_2r^2\cos(\theta)\sin(\theta)\left(l-\acute{l}\right)^2}{l^2}\right.$$
$$+2\sin(\theta)\cos(\theta)\left(m_2r^2\frac{\left(r\acute{l}\cos(\theta)+lc\right)^2}{l^2c^2}+m_3r^2\frac{(r\cos(\theta)+c)^2}{c^2}\right)+2\sin^2(\theta)$$
$$\left(\frac{m_2r^3\acute{l}\sin(\theta)\left(r\acute{l}\cos(\theta)+lc\right)(r\cos(\theta)-c)(r\cos(\theta)+c)}{l^2c^4}\right.$$
$$\left.\left.\frac{m_3r^3\sin(\theta)(r\cos(\theta)+c)^2(r\cos(\theta)-c)}{c^4}\right)\right)$$
$$+g\left(\sin(\theta)\left(m_1\acute{r}+m_2r+m_3r\right)+\sin(\theta)\cos(\theta)\left(\frac{m_2r^2\acute{l}}{lc}+\frac{m_3r^2}{c}\right)\right)=Q_k \tag{A.6}$$

A.2 Derivation of external forces by means of the virtual work principle

The virtual work principle is used to define the external forces and torques acting in the dynamic equation of the servo press. A virtual work is produced when a virtual displacement δr consistent with the forces and constraints is applied to a system in equilibrium.

The virtual work of external forces and torques is defined A.8 in generalised coordinates Q_k of the servo press, with the virtual displacement denoted as $\delta r = \theta, y$. The displacement of the ram y with respect to the crankshaft's axis is defined by A.7.

$$y = -r\cos(\theta) - l\cos(\beta) \tag{A.7}$$

The work carried out by the external forces and torques that act over the mechanical subsystem is given by A.8.

$$\begin{aligned}
\delta W &= \tau_e \eta \delta\theta - \tau_{fric}\delta\theta - (F_{ms} + F_{lb})\,\delta y \\
&= \tau_e \eta \delta\theta - \tau_{fric}\delta\theta - (F_{ms} + F_{lb})\,(-r\sin(\theta)\delta\theta - l\sin(\beta)\delta\beta) \\
&= \tau_e \eta \delta\theta - \tau_{fric}\delta\theta - (F_{ms} + F_{lb})\left(-r\sin(\theta)\delta\theta - \frac{lr\sin(\theta)}{l}\delta\beta\right) \\
&= \tau_e \eta \delta\theta - \tau_{fric}\delta\theta - (F_{ms} + F_{lb})\,r\sin(\theta)\,(\delta\theta + \delta\beta) \\
&= \tau_e \eta \delta\theta - \tau_{fric}\delta\theta - (F_{ms} + F_{lb})\,r\sin(\theta)\left(\delta\theta + \frac{r\cos(\theta)}{c}\delta\theta\right)
\end{aligned} \tag{A.8}$$

Generalised external forces and torques are then obtained as in A.9.

$$\frac{\delta W}{\delta\theta} = Q_k = \tau_e \eta - \tau_{fric} - (F_{ms} + F_{lb})\,r\sin(\theta)\left(1 + \frac{r\cos(\theta)}{c}\right) \tag{A.9}$$

Appendix B

Test bench design

B.1 Calculation of a π-group

This appendix addresses the calculation of a π-group elaborated with τ_e and the primary magnitudes F_{ms}, m_3 and r. The terms of 4.2 are replaced by the mentioned magnitudes and by their fundamental dimensions as in B.1.

$$\pi_1 = \tau_e F_{ms}^{\alpha_1} m_3^{\alpha_2} r^{\alpha_3} \rightarrow M^0 L^0 T^0 = M L^2 T^{-2} (M L T^{-2})^{\alpha_1} M^{\alpha_2} L^{\alpha_3} \tag{B.1}$$

Developing the above expression, values of α_1, α_2 and α_3 are obtained so that a dimensionless π_1-group is formed as in B.2.

$$\begin{aligned} M^0 L^0 T^0 &= M^{1+\alpha_1+\alpha_2} L^{2+\alpha_1+\alpha_3} + T^{-2-2\alpha_1} \\ 0 &= 1 + \alpha_1 + \alpha_2 \qquad \alpha_2 = 0 \\ 0 &= 2 + \alpha_1 + \alpha_3 \qquad \alpha_3 = -1 \\ 0 &= -2 - 2\alpha_1 \qquad \alpha_1 = -1 \\ \pi_1 &= \tau_e F_{ms}^{-1} r^{-1} = \frac{\tau_e}{F_{ms} r} \end{aligned} \tag{B.2}$$

B.2 Analytic equations of parameters' power

This section of Appendix B collects the analytical expression of the power of servo press's parameters. The powers of parameters are calculated using the energy expressions of the parameters defined in Appendix A, as in B.3.

$$P_x = \frac{d}{dt}E_x \qquad x = 1, 2, ...X \tag{B.3}$$

The analytical expressions of the parameters' power are defined on the basis of the angular position of the crankshaft $\theta(t)$. Analytical expressions of the power of the servo press's parameters are shown in the set of equations B.4, where $\theta(t), \dot{\theta}(t)$ and $\ddot{\theta}(t)$ are defined as $\theta, \dot{\theta}$ and $\ddot{\theta}$ respectively for the sake of simplicity.

$$\begin{aligned}
P_{m_1} &= g m_1 \acute{r} \dot{\theta} \sin(\theta) \\
P_{m_2} &= \frac{m_2(l-\acute{l})^2 r^2 \dot{\theta} \cos(\theta)^2 \ddot{\theta}}{l^2} - \frac{m_2(l-\acute{l})^2 r^2 \dot{\theta}^3 \cos(\theta)\sin(\theta)}{l^2} + m_2 \left(-r\theta \sin(\theta)\right. \\
&\quad \left. - \frac{\acute{l} r^2 \theta \cos(\theta)\sin(theta(t))}{lc}\right)\left(-r(\ddot{\theta}\sin(\theta) - r\dot{\theta}^2\cos(\theta) - \frac{\acute{l} r^2 \ddot{\theta}\cos(\theta)\sin(\theta)}{lc}\right. \\
&\quad \left. + \frac{\acute{l} r^2 \dot{\theta}^2 \sin(\theta)^2}{lc} - \frac{\acute{l} r^4 \dot{\theta}^2 \cos(\theta)^2 \sin(\theta)^2}{lc^3} - \frac{L r^2 \dot{\theta}^2 \cos(\theta)^2}{lc}\right) \\
&\quad - g m_2 \left(-r\dot{\theta}\sin(\theta) - \frac{L r^2 \dot{\theta}\cos(\theta)\sin(\theta)}{lc}\right) \\
P_{m_3} &= m_3 \left(-r\dot{\theta}\sin(\theta) - \frac{r^2\dot{\theta}\cos(\theta)\sin(\theta)}{c}\right)\left(-r\ddot{\theta}\sin(\theta) - r\dot{\theta}^2\cos(\theta)\right. \\
&\quad \left. - \frac{r^2\ddot{\theta}\cos(\theta)\sin(\theta)}{c} + \frac{r^2\dot{\theta}^2\sin(\theta)^2}{c} - \frac{r^4\dot{\theta}^2\cos(\theta)^2\sin(\theta)^2}{c^3} - \frac{r^2\dot{\theta}^2\cos(\theta)^2}{c}\right) \\
&\quad - g m_3 \left(-r\dot{\theta}\sin(\theta) - \frac{r^2\dot{\theta}^2\sin(\theta)\cos(\theta)^2}{c}\right) \\
P_{I_1} &= I_1 \ddot{\theta}\dot{\theta} \\
P_{I_2} &= I_2 \dot{\theta} c^2 \ddot{\theta} \\
P_\xi &= \xi x \dot{x}
\end{aligned} \tag{B.4}$$